# S-Band Monopulse Radar Receiver Design and Implementation

by

Mussie Ghebreegziabiher Hagos
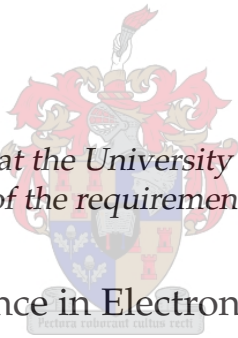
*Thesis presented at the University of Stellenbosch in partial fulfilment of the requirements for the degree of*

## Master of Science in Electronic Engineering

Department of Electrical and Electronic Engineering
University of Stellenbosch
Private Bag X1, 7602 Matieland, South Africa

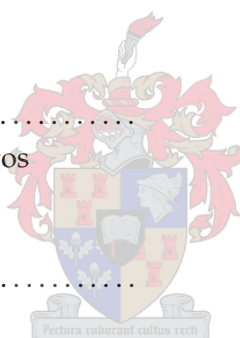Study leader: Dr. Cornell van Niekerk

January 2006

# Declaration

I, the undersigned, hereby declare that the work contained in this thesis is my own original work and that I have not previously in its entirety or in part submitted it at any university for a degree.

Signature: . . . . . . . . . . . . . . . . . . . . . . . . . . . . . . . .

Mussie G. Hagos

Date: . . . . . . . . . . . . . . . . . . . . . . . . . . . . . . . . . . .

# Abstract

This thesis documents the design and implementation of an S-band receiver for phase-comparison monopulse radar. The design and evaluation of the various sub-systems involved in realizing the receiver are discussed in detail. The designed sub-systems are connected via low loss coaxial cables to form the complete phase-comparison monopulse radar receiver. The performance of the receiver is evaluated and compared with the theoretical results, in terms of frequency response, gain and noise figure.
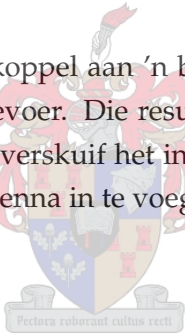
The designed receiver is finally connected to an existing antenna system, and a preliminary test of the complete radar is performed. The initial results show that the design is successful, but the boresight-axis of the radar has shifted in angle and requires pre-comparator phase shifting in order to obtain accurate tracking.

# Opsomming

Hierdie tesis dokumenteer die ontwerp en implementasie van 'n S-band ontvanger vir 'n fase-vergelyking monopulse radar. Die ontwerp en evaluering van die verskeie subsisteme in die besef van die ontvanger word bespreek. Die ontwerp subsisteme word gekoppel via lae verlies coaxial kabels na uit die hele fase-vergelyking monopulse radar ontvanger. Die prestasie van die ontvanger is bereken in terme van die frekwensie weergawe, aanwins en ruis syfer word vergelyk met die teoreties verwag te resultate.

Die ontwerp ontvanger is finaal gekoppel aan 'n bestaande antenne stelsel en 'n voorlopige toets van die hele stelsel is uitgevoer. Die resultate wys dat die ontwerp suksesvol is, maar die middelpunt van die radar verskuif het in hoek. Hierdie kan reggestel word deur die nodige faseskuif direk na die antenna in te voeg.

# Acknowledgements

# Contents

# List of Figures

# List of Tables

# List of Abbreviations and Acronyms

| | |
|---|---|
| ACM | Amplitude-Comparsion Monopulse |
| dB | Decibel |
| dBm | Decibel with respect to 1mW |
| DC | Direct Current |
| ES | Error Signal |
| GHz | Gigahertz |
| Hz | Hertz |
| IC | Integrated Circuit |
| IF | Intermediate Frequency |
| IF1AMP1 | First amplfier of the $1^{st}$ IF stage |
| IF1AMP2 | Second amplfier of the $1^{st}$ IF stage |
| IF1FLT | $1^{st}$ IF stage Filter |
| IF2FLT | $2^{nd}$ IF stage Filter |
| IM | Intermodulation |
| KHz | kilohertz |
| LF | Loop Filter |
| LO | Local Oscillator |
| MHz | Megahertz |
| MIX1 | First Mixer |
| MIX2 | Second Mixer |
| PCB | Printed-Circuited Board |
| PCM | Phase-Comparsion Monopulse |
| PLL | Phase-Locked-Loop |
| RF | Radio Frequency |
| RFAMP | RF Amplifier |
| RFFLT | RF Filter |
| SMA | Subminiature |
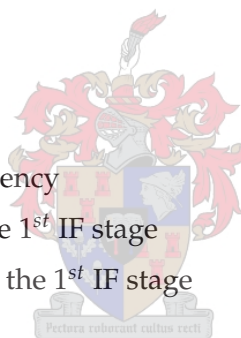
SOLT          Short-Open-Load-Through

SAW           Surface Acoustic Wave

VCO           Voltage Controlled Oscillator

VNA           Vector Network Analyzer
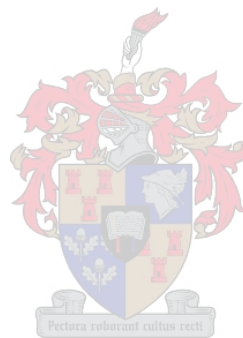
# Chapter 1

# Introduction

## 1.1 Background

This thesis describes the design and implementation of an S-band receiver for a phase-comparison monopulse radar. Phase-comparison monopulse (PCM) is a tracking technique that provides accurate angular position of a moving target from a single pulse. The first PCM radar was developed in 1943 by the General Electric Company [1] with principal contribution in eliminating tracking errors associated with target signal modulation.

## 1.2 Overview of the Project

This project is a continuation to the work that was launched to build and test two-dimensional PCM radar at the University of Stellenbosch. As a first step towards building the PCM radar, a servomechanism and an antenna-system with 14dB gain and $15^o$ beamwidth have been designed and implemented as shown in Figure 1.1. The aim of this thesis will be to design, build and test a PCM radar receiver and incorporate it into the existing system.

### 1.2.1 Receiver Specifications

With the goal of designing a complete PCM radar receiver, some design specifications have to be laid down. The following specifications were taken from the existing system and will be used as a reference for performance evaluation of the receiver and the complete PCM radar.

- The PCM radar should able to track a moving target in 5m range and over $\pm 7.5^o$ of the system boresight-axis.

- The target signal power and center frequency are 12dBm and 3000MHz, respectively.

- The receiver must able to downconvert the signals received at the antennas to a 10.7MHz intermediate frequency (IF).

- A phase sensitive detector with an input frequency of 0-270MHz and maximum input power of 0dBm should be used to determine the error signal (ES), which is equivalent to the angular deviation of the target from the system boresight-axis.
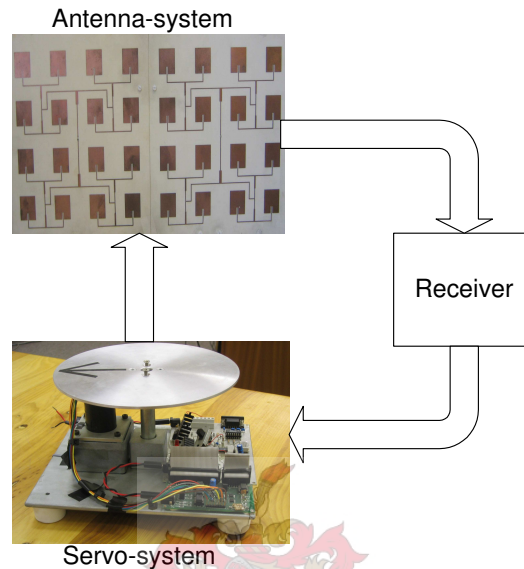


**Figure 1.1:** Existing system.

## 1.3   Overview of the Thesis

This thesis starts with an overview of phase-comparison monopulse (PCM) radar in chapter 2. In this chapter, the basics of PCM radar is reviewed and an attempt is made to specify the effect of certain parameters on the performance of the PCM radar.

Chapter 3 describes the justification of the various sub-systems used to implement the PCM radar receiver, and analyses the overall performance of the receiver using the specifications given in the data sheets of the sub-systems.

Chapter 4 deals with the design and implementation of the various passive sub-systems of the PCM radar receiver - a $0/180^o$ microwave hybrid circuit, microwave filters and power dividers.

Chapter 5 focuses on the design and evaluation of the active sub-systems of the receiver, which includes amplifiers, mixers and local oscillators.

Chapter 6 presents the final measurements of the receiver and the complete PCM radar.

Chapter 7 concludes the thesis through reflecting on its contents and results achieved, while a critical review of the designed receiver is given for further modifications.
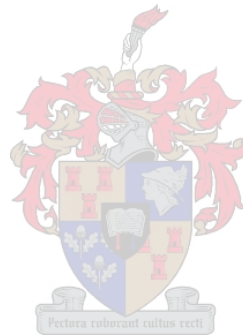
# Chapter 2

# Theory of Phase-Comparison Monopulse (PCM) Radar

## 2.1 Introduction

The intent of this chapter is to give a general overview of phase-comparison monopulse (PCM) radar. Section 2.2 briefly explains the basic concept of tracking radars, while section 2.3 explains the main sub-systems of the PCM radar. The understanding on PCM radar is further enhanced mathematically in appendix A and section 2.4, which examine the effect of certain parameters on the performance and accuracy of the radar.

## 2.2 Tracking Radar Basics

Figure 2.1 shows a basic block diagram of tracking radar. Any angular deviation of the target from the system boresight-axis generates an error signal (ES), which is equivalent to the angular deviation of the target; and tracking is so accomplished by supplying the ES to the servo-system, which positions the system boresight-axis back again on the target. Several techniques have been employed to generate the ES [1, 2]. Some of these techniques include the sequential lobing, conical scan and monopulse techniques.
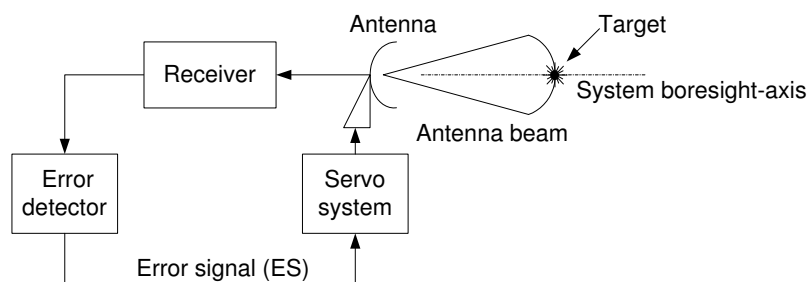
**Figure 2.1:** Basic block diagram of tracking radar.

### 2.2.1 Sequential Lobing Technique

A sequential lobing technique uses a squinted antenna beam which alternately switches between two positions as shown in Figure 2.2. The difference in amplitude of the voltages obtained from these two positions forms the required error signal (ES). For a target on the switching axis, for example, the difference is zero and this establishes a well-defined system boresight-axis, which is along the switching-axis.
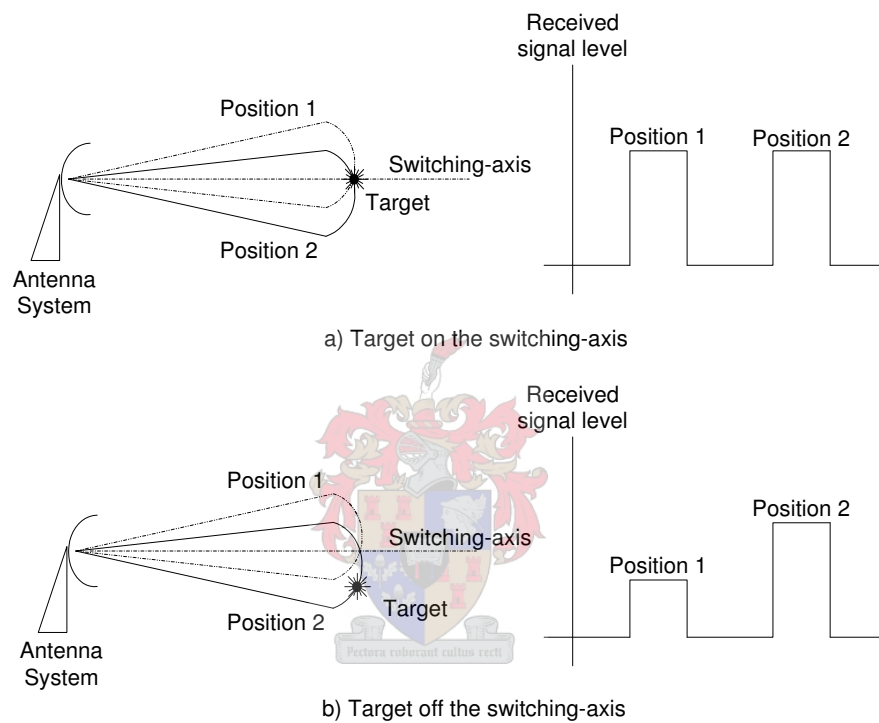


**Figure 2.2:** Sequential lobing technique.

### 2.2.2 Conical Scan Technique

In a conical scan technique a single antenna beam, but tilted by a small angle, called squint angle is rotated about the rotation-axis as shown in Figure 2.3. The signals received at the antenna are amplitude modulated and the amount of modulation, which depends on the location of the target, forms the error signal (ES). For a target on the rotation-axis, for example, the modulation is zero and this establishes a well-defined system boresight-axis, which is along the rotation-axis.

### 2.2.3 Monopulse Technique

Pulse to pulse variations, mainly due to external noise, impose an inherent limitation in the accuracy and performance of the above-mentioned tracking techniques [1, 2]. To over-

come this problem a monopulse, also called simultaneous lobing, technique was developed [3]. This technique is more accurate and faster than the above-mentioned techniques as the former uses a single pulse to determine the error signal (ES). Depending on the antenna-system configuration and parameters used to extract the ES, the monopulse technique can be mainly classified as amplitude-comparison monopulse and phase-comparison monopulse techniques.
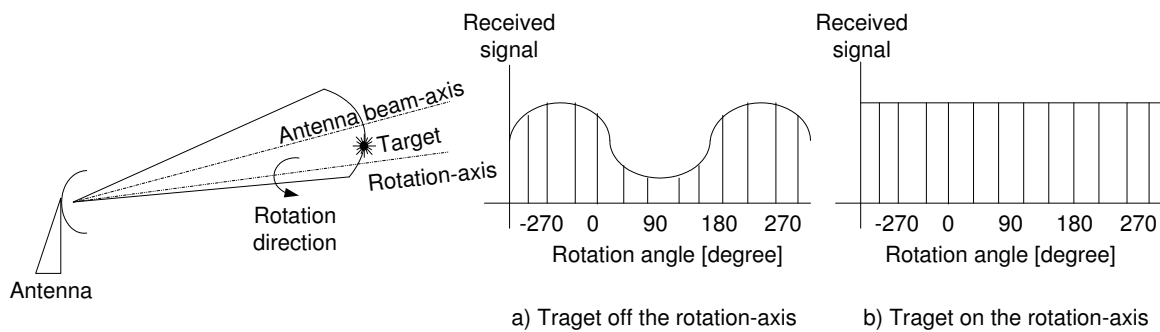


**Figure 2.3:** Conical scan technique.

### 2.2.3.1   Amplitude-Comparison Monopulse (ACM) Technique

Figure 2.4 shows the antenna configuration of a two-dimensional amplitude-comparison monopulse (ACM) technique. It is constructed using a single antenna aperture with two closely spaced feeds, each producing identical radiation patterns displaced from the antenna boresight-axis. Similar to the sequential lobing technique discussed in section 2.2.1, the difference in amplitude of the voltages received at both feeds forms the error signal (ES). For a target signal arriving along the antenna boresight-axis, for example, the difference is zero and this establishes a well-defined system boresight, which is along the antenna boresight-axis.

### 2.2.3.2   Phase-Comparison Monopulse (PCM) Technique

Figure 2.5 shows the antenna configuration of a phase-comparison monopulse (PCM) technique. It is constructed using two antenna apertures separated by several wavelengths. The apertures, each having a single feed, produce identical radiation patterns, which are symmetrical about their individual boresight-axes and almost overlapping at the far end. Therefore, the amplitudes of the voltages received at the feeds of the apertures are equal. There will be, however, a time or phase delay between the arrivals of the signals, and this will be used to generate the error signal (ES). For a target signal arriving along the antenna boresight-axis, for example, the phase delay between the signals received at the feeds is zero
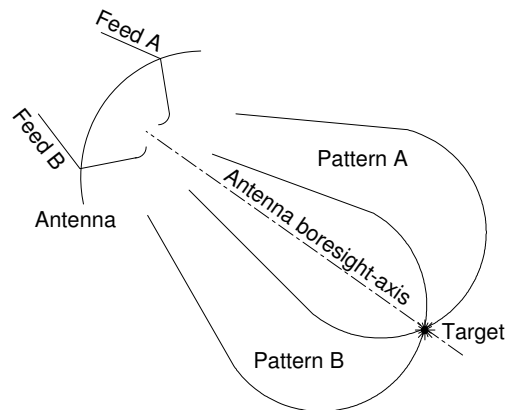
**Figure 2.4:** Antenna configuration for amplitude-comparison monopulse technique.

and this establishes a well-defined system boresight-axis, which is midway and parallel to the individual boresight-axes of the antennas.
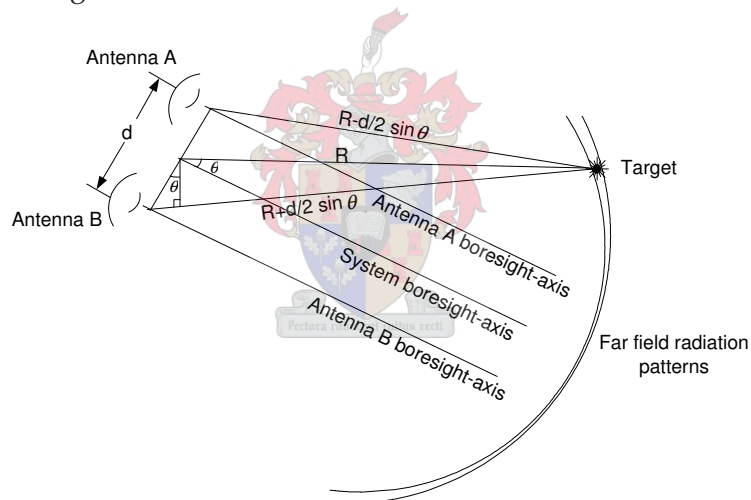


**Figure 2.5:** Antenna configuration for phase-comparison monopulse technique.

## 2.3 Phase-Comparison Monopulse (PCM) Radar

Figure 2.6 shows a simplified block diagram for a two-dimensional PCM radar, which consists of an antenna, a servo-system and receiver with a comparator and phase sensitive detector.

### 2.3.1 The Antenna System

The antenna is a key sub-system of the PCM tracking radar. It is constructed using two apertures which are separated by several wavelengths [1] as shown in Figure 2.7. A target
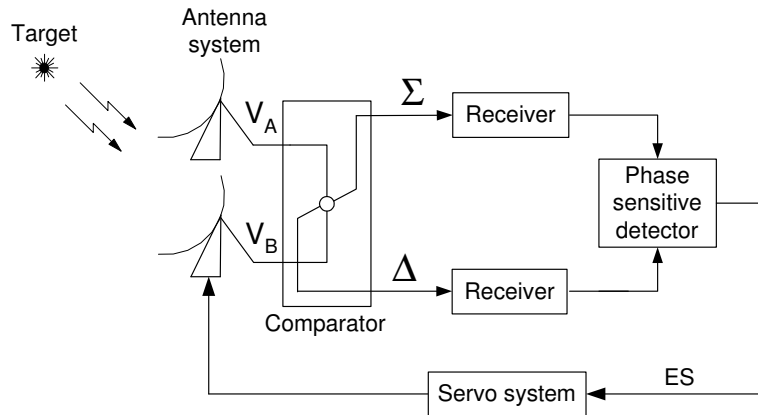
**Figure 2.6:** Block diagram of a two-dimensional PCM radar.

signal arriving at antenna B will be delayed from that arriving at antenna A due to the distance $S$, which is given by

$$S = d \sin \theta \tag{2.3.1}$$

where, $\theta$ is the angular deviation of the target from the system boresight-axis and $d$ is the separation between the feeds of the antennas.
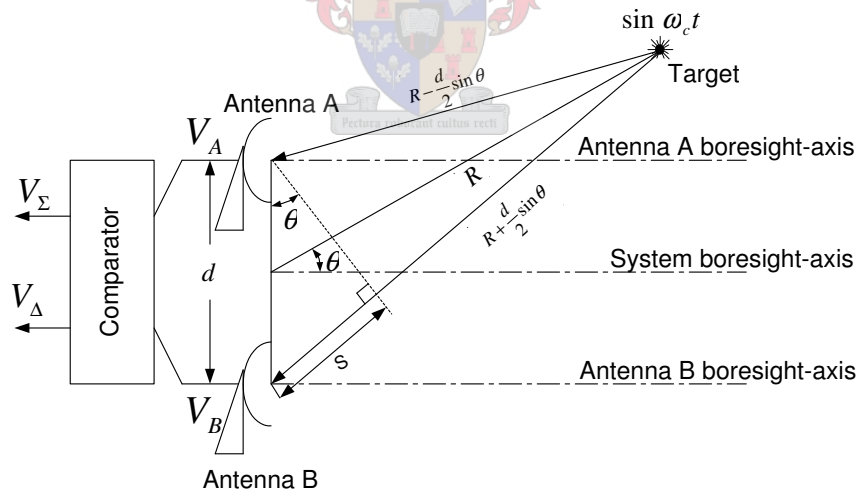


**Figure 2.7:** PCM radar operation.

The phase difference $\phi$ between the signals received at antennas A and B is calculated as

$$\phi = \frac{-2\pi d \sin \theta}{\lambda} \tag{2.3.2}$$

where $\lambda$ is the wavelength of the target signal.

Eqn. (2.3.2) has been plotted in Figure 2.8 for different values of $d/\lambda$, where one can see that the angular deviation of the target, also called tracking angle $\theta$, is restricted so as to limit the phase difference between the signals received $\phi$ between $\pm\pi$. Thus, any possible multi-boresight-axes confusion due to the periodicity of eqn. (2.3.2) is avoided. For $d/\lambda = 2$, for example, the angular deviation of the target is limited between $\pm15^o$. This is accomplished by limiting the beamwidth of the antennas to $30^o$ or less.
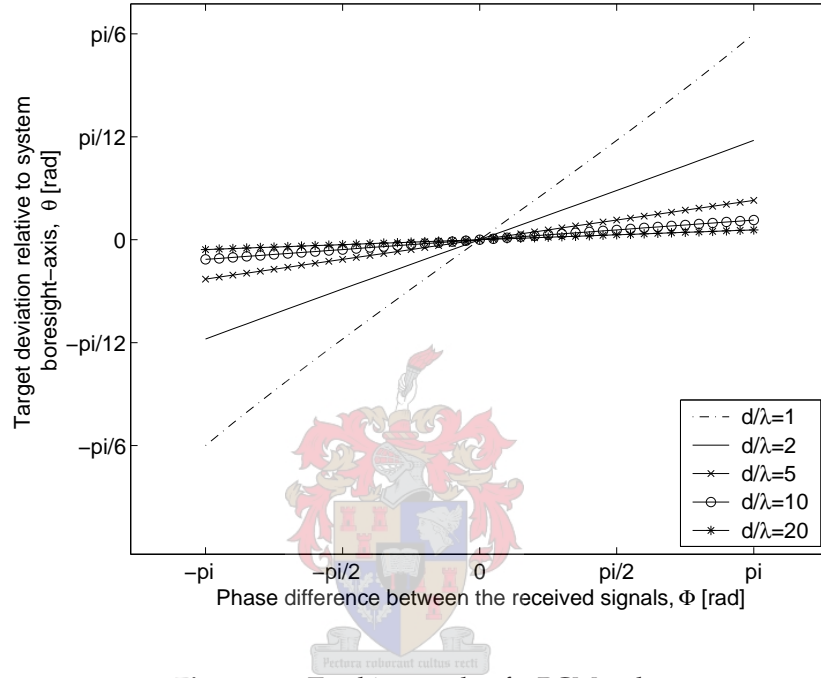


**Figure 2.8:** Tracking angle of a PCM radar.

### 2.3.2 The Comparator

The comparator outputs the sum ($\Sigma$) and difference ($\Delta$) of the signals received at the antennas A and B of the PCM radar. For a simple sinusoidal target signal ($\sin\omega_c t$), the $\Sigma$ and $\Delta$-signals are respectively given by

$$V_\Sigma \;=\; 2K\cos\left(\frac{\phi}{2}\right)\sin\left[\omega_c t + \tan^{-1}\left(\frac{\sin\phi}{\cos\phi + 1}\right)\right] \qquad (2.3.3)$$

$$V_\Delta \;=\; 2K\sin\left(\frac{\phi}{2}\right)\sin\left[\omega_c t + \tan^{-1}\left(\frac{\sin\phi}{\cos\phi - 1}\right)\right] \qquad (2.3.4)$$

where $\omega_c$ is the center frequency of the target signal, $\phi$ is relative phase difference and K is a constant which is related to the target signal, transmission medium and antenna parameters. The complete derivation of eqns. (2.3.3) and (2.3.3) is available in appendix A.1.

Comparison of the phase angles of the $\Sigma$ and $\Delta$-signals, respectively described by $\alpha_\Sigma$ and $\alpha_\Delta$, yields

$$\alpha_\Sigma - \alpha_\Delta = \tan^{-1}\left(\frac{\sin\phi}{\cos\phi + 1}\right) - \tan^{-1}\left(\frac{\sin\phi}{\cos\phi - 1}\right) \tag{2.3.5}$$

The relative amplitude and phase difference of eqn. (2.3.3) and (2.3.4) have been plotted in Figures 2.9 and 2.10, where it can be seen that an instantaneous phase reversal or null occurs at the system boresight-axis ($\theta = 0$). Thus, the relative amplitude and phase of the $\Sigma$ and $\Delta$ signals can be used to define the error signal (ES), which is equivalent to angular deviation of the target from the system boresight-axis.
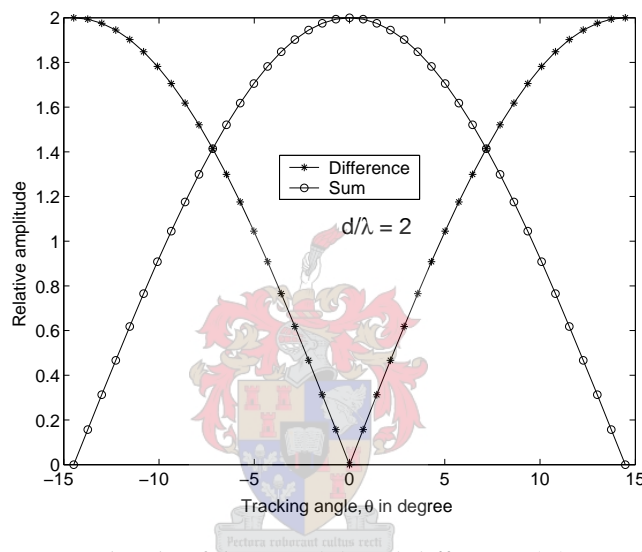


**Figure 2.9:** Relatve amplitude of the sum ($\Sigma$) and difference ($\Delta$) signals in PCM radar.
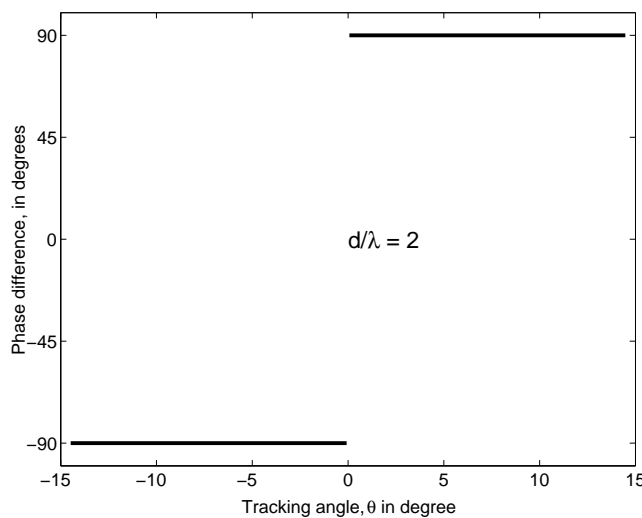


**Figure 2.10:** Phase difference between the sum ($\Sigma$) and difference ($\Delta$) signals in PCM radar.

### 2.3.3 The Receiver

Prior to the error signal (ES) detection, the $\Sigma$ and $\Delta$ signals obtained from the comparator are filtered, amplified and down converted using two superheterodyne receivers - the $\Sigma$ and $\Delta$-channels. The two channels should be balanced in terms of gain and phase. Besides, the $\Sigma$-channel carries the maximum signal level when the target signal arrives along the system boresight-axis, whereas an opposite condition exists for the $\Delta$-channel, where the signal level is minimum for a target signal arriving along the system boresight-axis.

### 2.3.4 The Phase Sensitive Detector and Servo-System

Finally, the downconverted version of the $\Sigma$ and $\Delta$ signals are compared in a phase sensitive detector to determine the error signal (ES), which is used to drive the servo-system for accurate tracking.

## 2.4 Analysis of PCM Radar

Since the error signal (ES) is determined towards the end of the $\Sigma$ and $\Delta$-channels of the receiver, any unbalance between the two channels influences the performance of the complete PCM system [1]. The unbalances could occur anywhere, but depending on the location and their effect, they can be classified as pre-comparator and post-comparator unbalances.

### 2.4.1 Pre-Comparator Unbalances

The pre-comparator section of the PCM radar includes the feeds of the antennas and the comparator itself, which both are mostly passive. Thus, in this section of the PCM radar, amplitude and phase unbalances are inevitable.

#### 2.4.1.1 Phase Unbalance

For a pre-comparator phase unbalance $\gamma$, the $\Sigma$ and $\Delta$ signals at the comparator output are respectively given as

$$V_{\Sigma d} = 2K\cos\left(\frac{\phi+\gamma}{2}\right)\sin\left[\omega_c t + \tan^{-1}\left(\frac{\sin\phi-\sin\gamma}{\cos\phi+\cos\gamma}\right)\right] \qquad (2.4.1)$$

$$V_{\Delta d} = 2K\sin\left(\frac{\phi+\gamma}{2}\right)\sin\left[\omega_c t + \tan^{-1}\left(\frac{\sin\phi+\sin\gamma}{\cos\phi-\cos\gamma}\right)\right] \qquad (2.4.2)$$

The relative phase and amplitude of eqns. (2.4.1) and (2.4.2) have been respectively plotted in Figures 2.11 and 2.12, where it can be seen that for $\gamma \neq 0$, the system boresight-axis shifts by

$$\theta = \sin^{-1}\left(\frac{\gamma\lambda}{2\pi d}\right) \qquad (2.4.3)$$
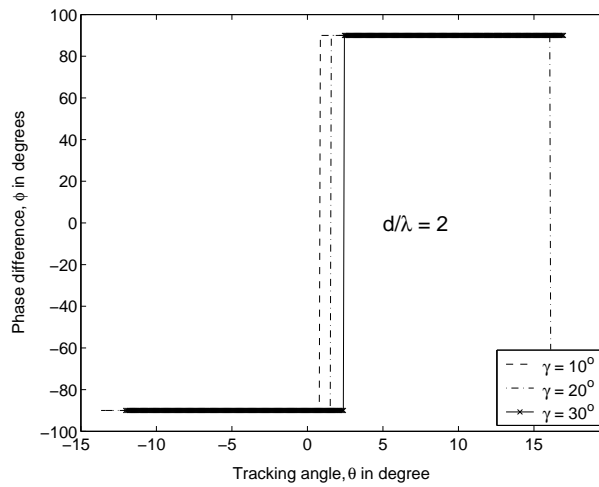
**Figure 2.11:** Phase difference between the sum ($\Sigma$) and difference ($\Delta$) signals under pre-comparator phase unbalance.
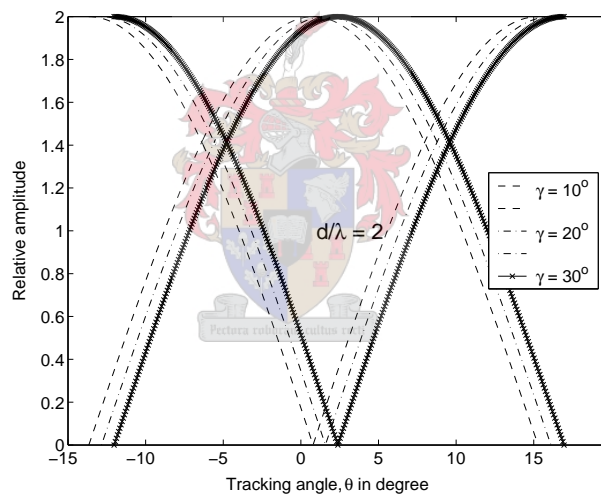


**Figure 2.12:** Amplitude of the sum ($\Sigma$) and difference ($\Delta$) signals under pre-comparator phase unbalance.

The complete derivation of eqns. (2.4.1) and (2.4.2)is available in appendix A.2.

Figure 2.13 plots a shift in system boresight-axis as a function of pre-comparator phase unbalance $\gamma$ for different values of $\frac{d}{\lambda}$. This shows that a shift in the system boresight-axis due to pre-comparator phase unbalance $\gamma$ can minimized using large values of $\frac{d}{\lambda}$. However, antennas with very narrow beamwidth will be required, as illustrated in Figure 2.8.
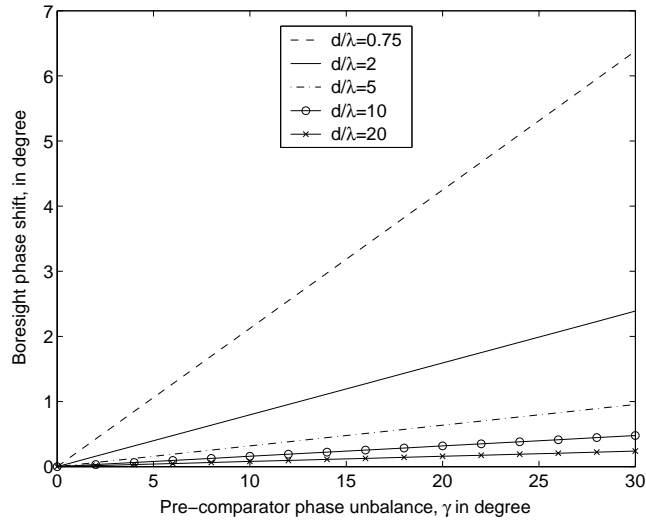
**Figure 2.13:** PCM radar system boresight-axis shift versus pre-comparator phase unbalance.

#### 2.4.1.2  Amplitude Unbalance

For a pre-comparator amplitude unbalance of $\ell$, the $\Sigma$ and $\Delta$ signals at the comparator output are respectively given by

$$V_{\Sigma a} = K\sqrt{(\ell\cos\phi + 1)^2 + (\ell\sin\phi)^2}\sin\left[\omega_c t + \tan^{-1}\left(\frac{\ell\sin\phi}{\ell\cos\phi + 1}\right)\right] \qquad (2.4.4)$$

$$V_{\Delta a} = K\sqrt{(\ell\cos\phi - 1)^2 + (\ell\sin\phi)^2}\sin\left[\omega_c t + \tan^{-1}\left(\frac{\ell\sin\phi}{\ell\cos\phi - 1}\right)\right] \qquad (2.4.5)$$
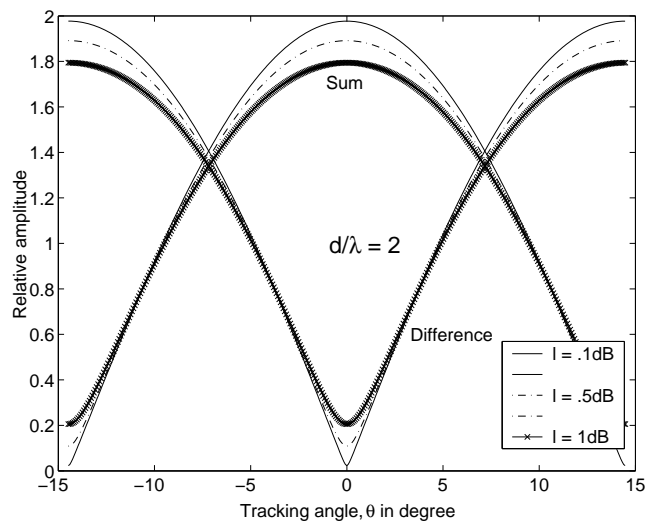


**Figure 2.14:** Phase difference between the sum ($\Sigma$) and difference ($\Delta$) signals under pre-comparator amplitude unbalance.

Eqns. (2.4.4) and (2.4.5) have been plotted in Figures 2.14 and 2.14 for different pre-comparator amplitude unbalances ($\ell$). One can see that the system boresight-axis doesn't shift for a pre-comparator amplitude unbalance. However, the phase reversal becomes gradual and the null of the $\Delta$ signal fills in, which effectively reduce the resolution of the complete PCM radar. Derivations of eqns. (2.4.4) and (2.4.5) are available in appendix A.3.
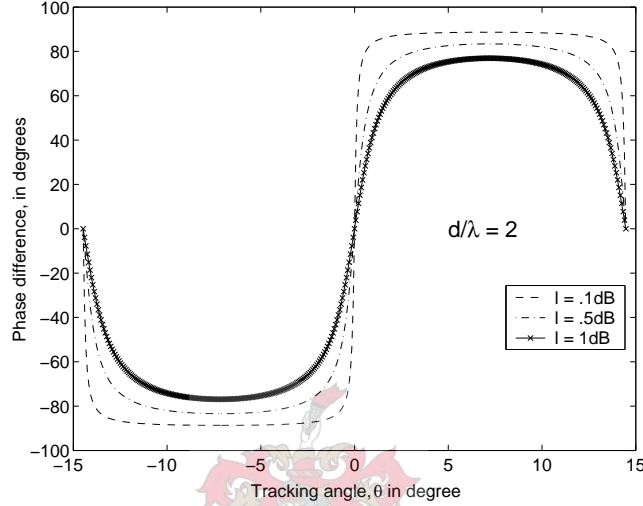


**Figure 2.15:** Amplitude of the sum ($\Sigma$) and difference ($\Delta$) signals under pre-comparator amplitude unbalance.

### 2.4.2 Post-Comparator Unbalances

The post-comparator section of the PCM radar includes two superhetrodyne receivers and the phase sensitive detector, which are mostly active. Thus, phase unbalance between them is inevitable. For a post-comparator phase unbalance $\alpha_K$, the phase sensitive detector output voltage is given by

$$V_o = \frac{|V_\Delta|}{|V_\Sigma|} \sin\left(\alpha_\Delta - \alpha_\Sigma - \alpha_k\right) \tag{2.4.6}$$

For $\alpha_K \neq 0$, the argument of the sin term of eqn. (2.4.6) will not be exactly $\frac{\pi}{2}$ or $-\frac{\pi}{2}$. Thus, the phase detector output voltage will not be equal to $\frac{|V_\Delta|}{|V_\Sigma|}$, but plus or minus some smaller value. This will reduce the sensitivity of the complete system, but will not shift the system boresight-axis unless $\alpha_K \geq |\frac{\pi}{2}|$.

## 2.5 Conclusion

This chapter discussed the operation and performance of PCM radar under both phase and amplitude unbalances. The PCM radar uses both the amplitude and phase information of the $\Sigma$ and $\Delta$ signals to determine the error signal (ES), which is equivalent to the angular deviation of the target from the system boresight-axis. The effect of pre-comparator phase

unbalance is very serious as it potentially shifts the system boresight-axis, but it can be minimized by performing the combination of the signals received at the antennas right at the reception and using very short, low loss and phase stable feed cables to avoid mismatch between the two channels. The effect associated with post-comparator unbalance is limited to reducing the sensitivity of the PCM radar receiver and can be minimized by keeping the sub-systems of both channels balanced in terms of gain and phase.
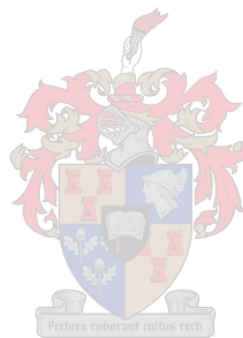
# Chapter 3

# System Level Analysis

## 3.1  Introduction

As mentioned in chapter 2, the outputs of the PCM radar receiver are fed into a phase sensitive detector to determine the error signal (ES), which is equivalent to the angular deviation of the target. Noise limits the minimum signal that can be detected, while harmonics and intermodulation distortions resulting from the nonlinearity of the receiver limit the maximum signal the receiver can handle. Thus, appropriate signal levels are required at the input of the phase sensitive detector. Figure 3.1 shows a preliminary PCM radar receiver with the two downconversion stages, a comparator and a phase sensitive detector.
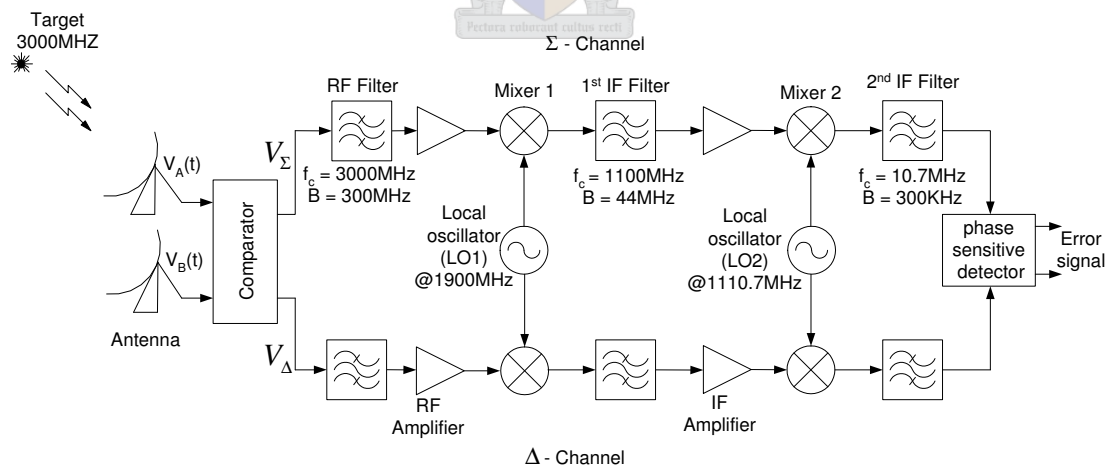


**Figure 3.1:** A preliminary PCM radar receiver.

Like conventional receivers, the PCM radar receiver is made up of filters, amplifiers, mixers and local oscillators (LOs). Accurate design and selection of these sub-systems is important to the overall operation and accuracy of the PCM radar. This chapter presents a top-to-down budget analysis of the PCM receiver in terms of power level, noise figure and frequency of operation.

## 3.2   Noise Figure and Noise Temperature

The minimum signal level that can be detected is limited by the thermal noise captured by the antennas facing a blackbody (which is at a temperature of 290K) and noise generated within the sub-systems of the receiver.

The thermal noise is commonly characterized by a power density N given by [4]

$$N = kTB \tag{3.2.1}$$

where k is Boltzman's constant ($1.38*10^{-23}$ joules/K), B is the bandwidth un Hertz and T is the temperature in Kelvin. In a 1-Hz bandwidth, for example, a -174dm thermal noise power is captured by the antennas facing a blackbody (which is at a temperature of 290K).

The noise generated within the receiver sub-systems is quantitatively expressed in terms of noise figure F, given by [4]

$$F = \frac{S_i/N_i}{S_o/N_o} \tag{3.2.2}$$

where $S_i$ and $N_i$ are the input signal and noise powers respectively, while $S_o$ and $N_o$ are the output signal and noise powers respectively.

Figure 3.2(a) shows a noisy sub-system, which can be fictitiously represented by an external effective noise temperature $T_e$ and noise free sub-system as shown in Figure 3.2(b). The total output noise $N_o$ of the noisy sub-system is then given by

$$N_o = G(kT_eB + N_i) \tag{3.2.3}$$

where $G$ and $F$ are respectively the gain and noise figure of the noisy sub-system, and $N_i$ is the input noise power.
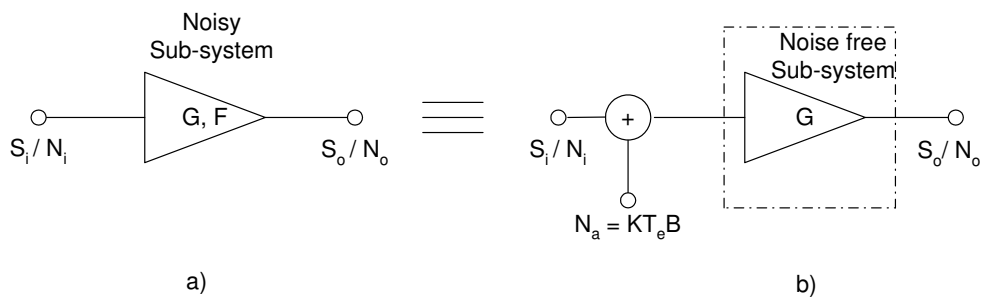


**Figure 3.2:** Effective noise temperature of a noisy sub-system.

Since $G = S_o/S_i$, substuting eqn. (3.2.3) into eqn. (3.2.2) yields

$$F = 1 + \frac{KT_eB}{N_i} \tag{3.2.4}$$

Substuting eqn (3.2.1) into eqn. (3.2.4) yields

$$F = 1 + \frac{T_e}{T} \tag{3.2.5}$$

Eqn. (3.2.5) has been plotted in Figure 3.3 for various input temperatures T. For antennas facing a space (which is at a temperature of 30K), the noise generated within the receiver is more dominant compared to the received noise, whereas for antennas facing a blackbody (which is at a temperature of 290K) the received noise is as dominant as the noise generated within the receiver. Thus, the former requires a low noise amplifier (LNA) [5] at its front end in order to improve the sensitivity of the receiver, but little is gained from such arrangement in the latter case.
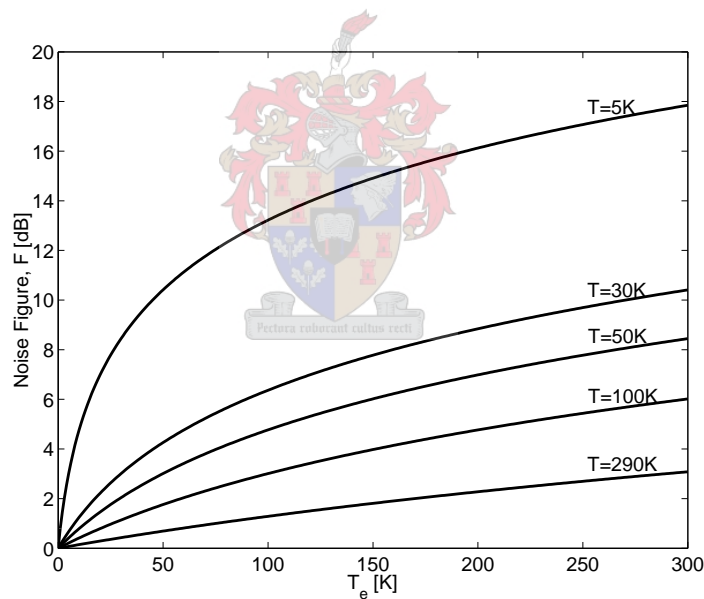


**Figure 3.3:** Degrdation in signal to noise ratio of a receiver.

## 3.2.1 Cascaded Noise Figure

Figure 3.4 shows a cascaded system, where each sub-system is characterized in terms of gain, bandwidth and noise figure or noise temperature. Noise generated at the front end appears with full gain at the output, whereas those originating further down the receiver chain are only amplified partially. Thus, the overall equivalent noise figure of a cascaded

system is given as [5]

$$F_e = F_1 + \sum_{i=2}^{n} \frac{F_i - 1}{\prod_{j=1}^{i-1} G_j} \tag{3.2.6}$$

where $F_i$ and $G_i$ are respectively the noise figure and gain of the sub-systems and $n$ is the number of sub-systems in the cascade.
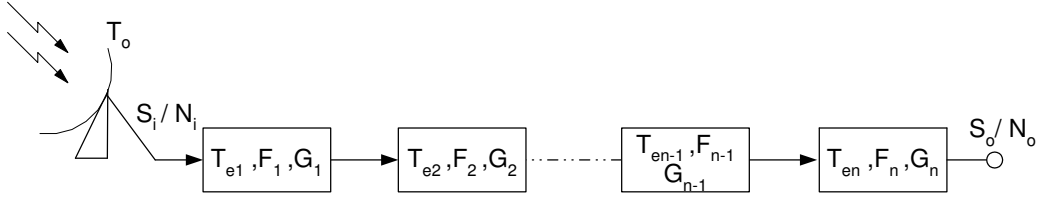


**Figure 3.4:** Cascaded system.

According to eqn. (3.2.6), the total noise figure of the cascaded system is mostly dominated by the noise figure of the front end sub-systems, and with some positive gain at the front end the noise contribution of the subsequent sub-systems can be minimized. Therefore, having a high gain LNA at the front end will not only strengthen the weak signal received at the antennas but also improve the sensitivity of the receiver.

In terms of effective noise temperature $T_e$, eqn. (3.2.6) can be expressed as

$$T_e = T_{e1} + \sum_{i=2}^{n} \frac{T_{ei}}{\prod_{j=1}^{i-1} G_j} \tag{3.2.7}$$

where $T_{ei}$ is the effective noise temperature of the sub-systems. Therefore, the overall noise temperature of a receiver plus an antenna is given by

$$T_{sys} = T + T_e \tag{3.2.8}$$

## 3.3   Choice of Operating Frequency

The signals received at the antennas of the PCM radar must be downconverted to 10.7MHz for detection. With a single downconversion from 3000MHz to 10.7MHz, a high Q pre-selector filter will be required as the image frequency will be centered at 2978.6MHz. The need for such high Q pre-selector filter, however, can be bypassed using two downconversion stages. Thus, from the RF signals received at the antennas, a first downconversion stage at L-band of 1100MHz (1$^{st}$ IF) is used followed by a second downconversion to the required IF of 10.7MHz (2$^{nd}$ IF). The choice of the 1$^{st}$ IF of 1100MHz results from the normalized spur plot shown in Figure 7.15 of [6], which comprises no potentially interfering spurious frequency and shifts the image frequency to 800MHz.

## 3.4   Local Oscillator Technology

Two stable local oscillators (LOs) centered at 1900MHz and 1110.7MHz are required in or-
der to downconvert the received RF signal at 3000MHz to the $1^{st}$ IF of 1100MHz in the
first downconversion stage and $2^{nd}$ IF of 10.7MHz in the second downconversion, respec-
tively. Among various methods of LO generation [7], the phase-locked frequency synthe-
sizer shown in Figure 3.5 is chosen, as it is easy to implement and can provide a stable and
low-phase noise LO signal. The output frequency of the synthesizer $f_{out}$ is given by

$$f_{OUT} = N f_{REF} \tag{3.4.1}$$

where $f_{REF}$ is the reference frequency and N is the feedback counter.
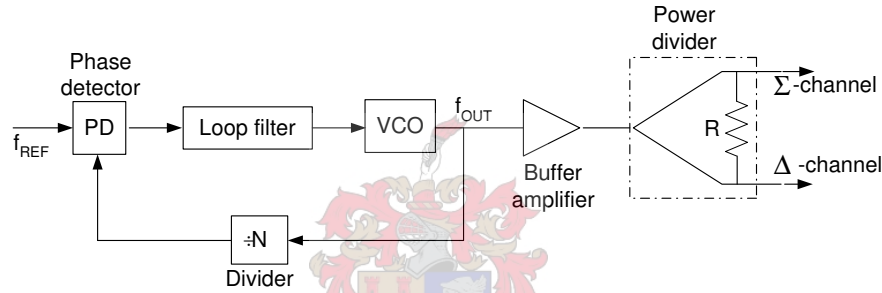


**Figure 3.5:** Local oscillator technology for the PCM radar receiver.

The buffer amplifier and symmetrical power divider are included as part of the synthesizer
circuit to boost the output signal to the required level and provide better output impedance
matching and isolation between the receiver and the synthesizer circuit. This will ensure
phase coherence between the two channels of the receiver and consequently improve the
sensitivity of the receiver.

## 3.5   Comparator

A balanced $0/180^o$ microwave hybrid [5] shown in Figure 3.6 is employed to generate the
sum ($\Sigma$) and difference ($\Delta$) signals of a PCM radar. The RF signals arriving at the feeds of
the antennas of the PCM radar are fed into ports 1 ($V_A$) and 2 ($V_B$), while vectorial addition
and subtraction of these signals appear at ports 3 ($V_\Sigma$) and 4 ($V_\Delta$), respectively.
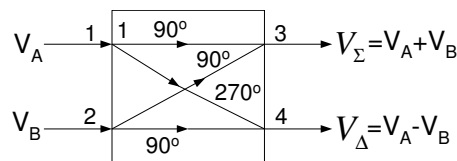


**Figure 3.6:** Balanced $0/180^o$ microwave hybrid.

## 3.6  RF Filter

The initial filtering after the $0/180^o$ microwave hybrid protects the front-end of the receivers from being overloaded by strong undesired adjacent signals, including the image frequency. It also limits the amount of noise entering the receiver. The addition of an RF filter at the front end usually degrades the sensitivity of the receiver due to the inherent loss of the filter. In this particular PCM radar receiver, however, the effect of the RF filter is not significant, as the sensitivity is already degraded by the $0/180^o$ microwave hybrid. To ensure low ripple, a $3^{rd}$ order Chebychev bandpass filter with 20dB return loss over 10% of relative bandwidth is suggested for this application. This will reject frequencies outside the passband and limit the noise entering the receiver.

## 3.7  RF Amplifier

In most receivers, a low noise amplifier (LNA) is usually used at the RF stage to boost the strength of the received signal and improve the sensitivity of the receiver [5, 8]. In this design, however, little will be gained using a LNA at the front end. This is mostly because the receiver is preceded by the $0/180^o$ microwave hybrid with inherent 3dB insertion loss. Besides, the noise received at the antennas facing a blackbody is as significant as the noise generated within the receiver. Thus, the choice of an RF amplifier with 15dB gain and 3.5dB noise figure provides the necessary gain at the RF stage without driving the subsequent sub-systems into compression.

## 3.8  Mixers

Mixers translate the received RF signals into intermediate frequencies (IFs) for easy amplification, filtering and detection. To generate the desired IF frequency and other frequencies that are not present at the input, mixers use nonlinear devices such as diodes or transistors
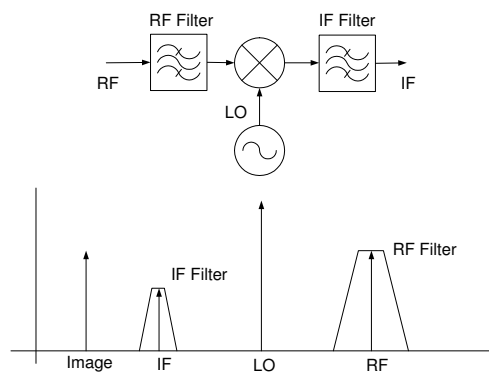


**Figure 3.7:** Mixer output spectrum.

[9]. The output frequency of a mixer which is driven by a stable LO $f_{LO}$ is given by

$$f_{IF} = mf_{RF} + nf_{LO} \tag{3.8.1}$$

where $f_{RF}$ is the input RF frequency, and $m$ and $n$ are integers. The fundamental mixing product (m=1 and n=-1) of eqn. (3.8.1) yields the desired intermediate frequency (IF). The same IF frequency, however, can also be a result of an image signal, which is 2$x$IF away from the RF signal. This is illustrated in Figure 3.7. The use of an RF filter along with double downconversion stage provides the necessary suppression for such image signal. For both downconversion stages of the PCM radar receiver, double balanced mixers [8] were chosen as they offer superior performance in terms of third order intermodulation distortion and RF and LO signals suppression at the IF ports.

## 3.9 IF Amplifier

The additional gain required by the receiver is achieved at the IF section, as it easy to realize high gain stable amplifiers at low frequency. Thus, two amplifiers with 22dB and 17dB gain are cascaded to achieve the remaining gain of the receiver.

## 3.10 IF Filters

The IF filters are included to reject unwanted signals generated by the mixers. Since the selectivity of the receiver is determined at this stage, a $3^{rd}$ order Chebychev filter with narrow bandwidth of 4% is selected for the $1^{st}$ IF filter, while off-the-shelf ceramic filter from Mini-Circuits are recommended to realize the $2^{nd}$ IF filter.

## 3.11 Nonlinear characteristics

### 3.11.1 Compression Point

The fundamental output power of a mixer or amplifier $P_{OUT}$ is related linearly to the applied input power $P_{IN}$ by

$$G[dB] = 10\log\frac{P_{out}}{P_{in}} \tag{3.11.1}$$

Eqn. (3.11.1), however, deviates from being linear when the input power exceeds a certain level, called a 1dB-compression point, which is defined as the input power for which the output power saturates 1dB below the expected ideal value. A typical characteristics of a nonlinear sub-system with its associated ideal response is shown in Figure 3.8. This parameter determines the power handling capability of the nonlinear sub-systems of a receiver and special care must be taken not to operate such sub-systems in the proximity of their respective 1dB-compression points.
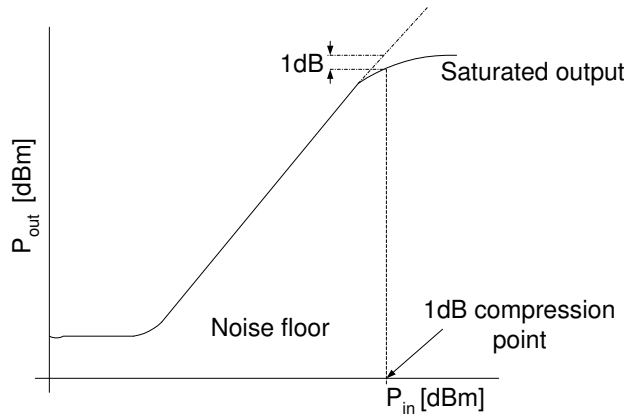
**Figure 3.8:** 1dB-compression point.

## 3.11.2   Intercept point

When two input RF signals, $f_{RF1}$ and $f_{RF2}$ are mixed with the LO signal $f_{LO}$, multitone IM products are generated and the output spectrum is given by

$$f_{IM} = m_1 f_{RF1} + m_2 f_{RF2} + n f_{LO} \qquad (3.11.2)$$

where $m_1$, $m_2$ and $n$ are all integers. Of all the IM products given by eqn. (3.11.2), the third order terms $2f_{RF2} - f_{RF1} - f_{LO}$ and $2f_{RF1} - f_{RF2} - f_{LO}$ fall close to the desired IF signal and make detection very difficult. Thus, active sub-systems with large third order intercept points must be used to improve the sensitivity of the receiver. The third order intercept point, as illustrated in Figure 3.9, is a fictitious point where the level of the third order terms equals that of the desired signal.
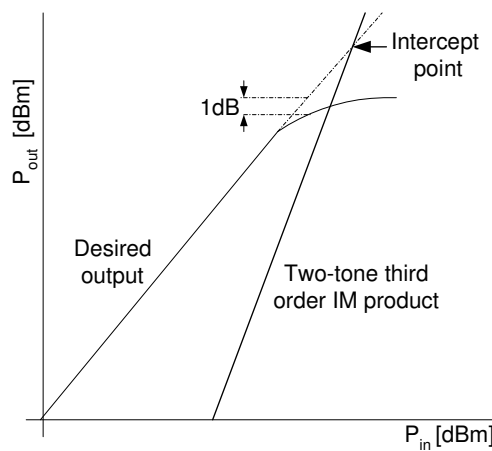


**Figure 3.9:** Third order intercept point.

## 3.12   Receiver Budget Analysis

The receiver budget analysis provides the signal and noise of the received signal as it passes through each sub-systems of the receiver. Figure 3.10 shows a single channel of the PCM radar receiver.
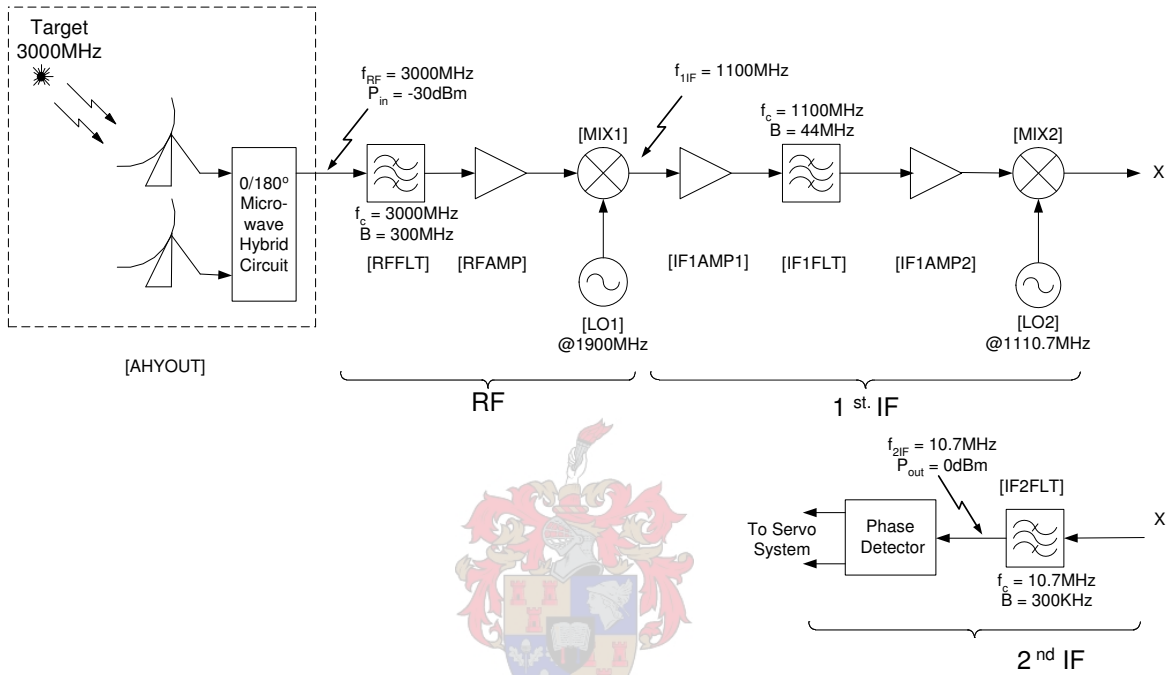


**Figure 3.10:** A single channel of the PCM radar receiver.

The strength of the signals received at the antennas of the PCM radar $P_r$ is given by Friis transmission equation [10]

$$P_r = \frac{P_t G_r \lambda^2}{(4\pi R)^2} \tag{3.12.1}$$

where $P_t$ is the transmitted power R is the range between the target and receiver antenna

| Sub-system | AHYOUT | RFFLT | RFAMP | MIX1 | IF1AMP1 | IF1FLT | IF1AMP2 | MIX2 | IF2FLT |
|---|---|---|---|---|---|---|---|---|---|
| Bandwidth[MHz] | | 300 | 6000 | 3000 | 3000 | 44 | 3000 | 1300 | 0.35 |
| Gain[dB] | | -1 | 15 | -8.5 | 22 | -1 | 17 | -9 | -4.5 |
| Noise Figure[dB] | | 1 | 3.5 | 8.5 | 3.8 | 1 | 4.1 | 9 | 4.5 |
| Input 1-dB Compression Point[dBm] | | | -3 | 5 | 12.1 | | 18 | 7 | |
| Cumulative Gain[dB] | | -1 | 14 | 5.5 | 27.5 | 26.5 | 43.5 | 34.5 | 30 |
| Signal[dBm] | -30 | -31 | -16 | -24.5 | -2.5 | -3.5 | 13.5 | 4.5 | 0 |
| Noise[dBm] | -89.2 | -89.2 | -60.1 | -68.3 | -45.9 | -46.9 | -29.9 | -38.9 | -41.4 |
| Cumulative Noise Figure[dB] | | 1 | 4.5 | 4.8578 | 5.3269 | 5.3275 | 5.3310 | 5.3314 | 5.3318 |

**Table 3.1:** PCM radar receiver budget analysis.

and $G_r$ is the gain of of the receiver antenna. For G=14dB, $P_t$ = 12dBm and R=5m the strength of the received RF signal, $P_r$ is -30dBm and the per-Hz input noise power is -174dBm as the antennas face a blackbody (which is at a temperature of 290K).

The theoretical cumulative gain and noise figure were calculated using eqns. (3.2.1) to (3.2.6) and the results are tabulated in Table 3.1. The signal level at the output of each sub-system was also monitored such that they always remain below their respective 1dB-compression point. The cumulative gain of the receiver is set to 30dB as the maximum input power of the phase sensitive detector AD8302 from Analog Devices [11] is 0dBm.

## 3.13 Conclusion

This chapter justifies the sub-systems used in designing the PCM radar receiver, selects the frequency of operation and monitors the level of the received signal and thermal noise. The results obtained from the analysis are summarized in Table 3.1, where it shows that non of the active sub-systems is driven into saturation and provides the required level at the input of the phase sensitive detector. Besides, the cumulative noise figure is calculated to be 5.3318dB.
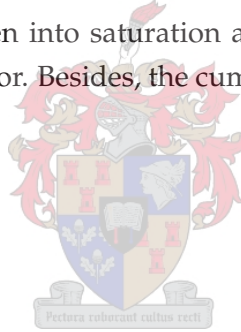
# Chapter 4

# Design and Evaluation of Passive Sub-Systems

## 4.1   Introduction

The passive sub-systems of the PCM radar receiver include: a comparator realized using $0^o/180^o$ microwave hybrid, microwave filters, and power dividers, which are required for the local oscillators (LOs). This chapter presents the design and evaluation of these sub-systems. Section 4.2 discusses the design and measurements of a $0^o/180^o$ microwave hybrid. The development and test results of a parallel-coupled microstrip-line and combline microwave filters are described in section 4.3. Section 4.4 presents the design of two Wilkinson power dividers with $2^{nd}$ harmonic suppression.

## 4.2   Design of a $0^o/180^o$ Microwave Hybrid at 3GHz

### 4.2.1   Introduction

The comparator of the PCM radar is implemented using a $0^o/180^o$ microwave hybrid, also called a ratrace [5]. As described in section 2.4, any phase unbalance introduced in this sub-system shifts the system boresight-axis of the PCM radar. Thus, special attention should be given to the design and implementation of this sub-system.

### 4.2.2   Network Theory

The configuration of a conventional $0^o/180^o$ microwave hybrid is illustrated in Figure 4.1, where the four ports are connected to a central ring with $3\lambda/2$ circumference and $\sqrt{2}Z_o$ characteristic impedance ($\lambda$ is the wavelength of the center frequency and $Z_o$ is the port impedance). Since the $0^o/180^o$ microwave hybrid is symmetrical about the X-X' plane, it can be easily analyzed using the even and odd excitation technique [12].
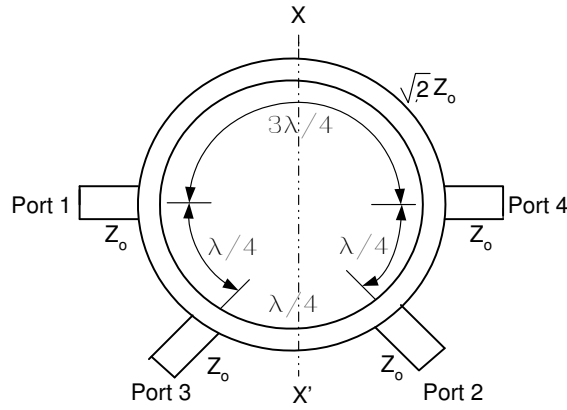
**Figure 4.1:** A $0^o/180^o$ microwave hybrid.

### 4.2.2.1 Even Mode Analysis

In an even mode analysis, two equal and in-phase signals are applied at either ports 1 and 4, or ports 2 and 3 of the $0^o/180^o$ microwave hybrid shown in Figure 4.1. Since the current is zero at the X-X' plane, the $0^o/180^o$ microwave hybrid can be effectively open-circuited at the plane of symmetry to obtain the network shown in Figure 4.2.
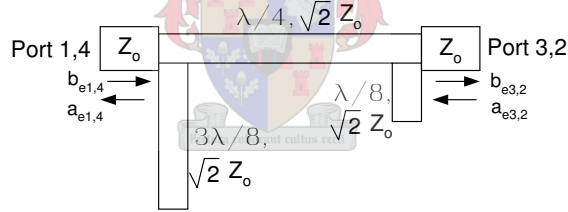


**Figure 4.2:** Bisection of $0^o/180^o$ microwave hybrid for even mode excitation.

The normalized ABCD matrix $T_e$ [5] of Figure 4.2 is given as a cascade of $3\lambda/8$ long open-circuited stub, $\lambda/4$ long transmission line and $\lambda/8$ long open-circuited stub. That is,

$$
\begin{aligned}
T_e &= \begin{bmatrix} 1 & 0 \\ -j/\sqrt{2} & 1 \end{bmatrix} \begin{bmatrix} 0 & j\sqrt{2} \\ j/\sqrt{2} & 0 \end{bmatrix} \begin{bmatrix} 1 & 0 \\ j/\sqrt{2} & 1 \end{bmatrix} \\
&= \begin{bmatrix} -1 & j\sqrt{2} \\ j\sqrt{2} & 1 \end{bmatrix}
\end{aligned}
\tag{4.2.1}
$$

In terms of scattering matrix, eqn. (4.2.1) can be written as

$$
S_e = \begin{bmatrix} j/\sqrt{2} & -j/\sqrt{2} \\ -j/\sqrt{2} & -j/\sqrt{2} \end{bmatrix}
\tag{4.2.2}
$$

**4.2.2.2 Odd Mode Analysis**

In an odd mode analysis, two equal but out of phase signals are applied at either ports 1 and 4, or 3 and 2 of the $0^o/180^o$ microwave hybrid shown in Figure 4.1. Since the voltage at the plane of symmetry (X-X′) is zero, the $0^o/180^o$ microwave hybrid can be effectively short-circuited at the X-X′ plane to obtain the network shown in Figure 4.3.
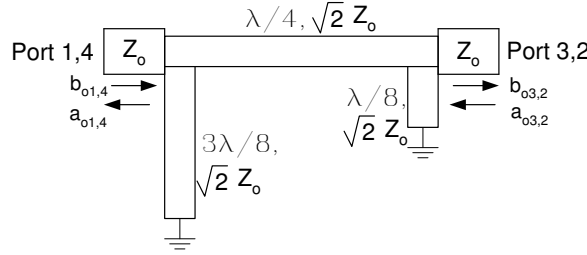


**Figure 4.3:** Bisection of $0^o/180^o$ microwave hybrid for odd mode excitation.

The normalized ABCD matrix $T_o$ of Figure 4.3 is given as a cascade of $3\lambda/8$ long short-circuited stub, $\lambda/4$ long transmission line and $\lambda/8$ long short-circuited stub. That is,

$$
\begin{aligned}
T_o &= \begin{bmatrix} 1 & 0 \\ j/\sqrt{2} & 1 \end{bmatrix} \begin{bmatrix} 0 & j\sqrt{2} \\ j/\sqrt{2} & 0 \end{bmatrix} \begin{bmatrix} 1 & 0 \\ -j/\sqrt{2} & 1 \end{bmatrix} \\
&= \begin{bmatrix} 1 & j\sqrt{2} \\ j\sqrt{2} & -1 \end{bmatrix}
\end{aligned}
\tag{4.2.3}
$$

In terms of scattering matrix, eqn. (4.2.4) can be written as

$$
S_o = \begin{bmatrix} -j/\sqrt{2} & -j/\sqrt{2} \\ -j/\sqrt{2} & j/\sqrt{2} \end{bmatrix}
\tag{4.2.4}
$$

Since the circuit is linear, the superposition principle is applied to obtain the complete scattering matrix of the $0^o/180^o$ microwave hybrid circuit as

$$
S = \begin{bmatrix} 0 & 0 & -j/\sqrt{2} & j/\sqrt{2} \\ 0 & 0 & -j/\sqrt{2} & -j/\sqrt{2} \\ -j/\sqrt{2} & -j/\sqrt{2} & 0 & 0 \\ j/\sqrt{2} & -j/\sqrt{2} & 0 & 0 \end{bmatrix}
\tag{4.2.5}
$$

From eqn. (4.2.5), the voltages at ports 3 and 4 are out of phase for an input voltage at port 1, while in phase for an input voltage at port 2. The input signals applied at ports 1 and 2 are equally divided between ports 3 and 4, while perfect isolation exists between ports 1 and 2; and ports 3 and 4. Moreover, all ports are perfectly matched.

### 4.2.3 T-Junction Discontinuity and Compensation

At all ports of the $0^o/180^o$ microwave hybrid circuit, unwanted parasitic reactances are involved due to the geometrical discontinuities associated with the T-junctions [13, 14]. Figure 4.4 shows a symmetrical microstrip T-junction along with its equivalent circuit. The parasitic reactances $X_A$ and $X_B$ are respectively given by [14]

$$\frac{X_A}{Z_o} = -\frac{D_2}{\lambda} \left( n\frac{\pi}{4} \right)^2 \tag{4.2.6}$$

and

$$\frac{X_B}{Z_o} = -\frac{X_A}{2Z_o} + \frac{2D_1}{n^2\lambda} \left[ \ln\left( \frac{1.43D_1}{D_2} \right) + 2 \left( \frac{D_1}{\lambda} \right)^2 \right] \tag{4.2.7}$$

for $D_2/D_1 > 0.5$, where $n$ is given by

$$n = \frac{\sin(\pi D_2/\lambda)}{\pi D_2/\lambda} \tag{4.2.8}$$
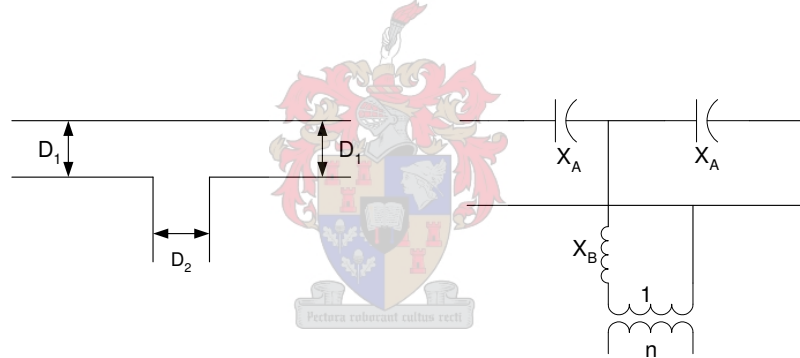


**Figure 4.4:** Equivalent circuit for a symmetrical microstrip-line T-junction.

The reactances ($X_A$ and $X_B$) are dependent on the transmission line characteristic impedance $Z_o$, dielectric constant of the substrate used and the frequency of operation. At higher frequencies the parasitic reactances are significant, and entirely disappears at low frequency as both $D_1/\lambda$ and $D_2/\lambda$ approach zero.
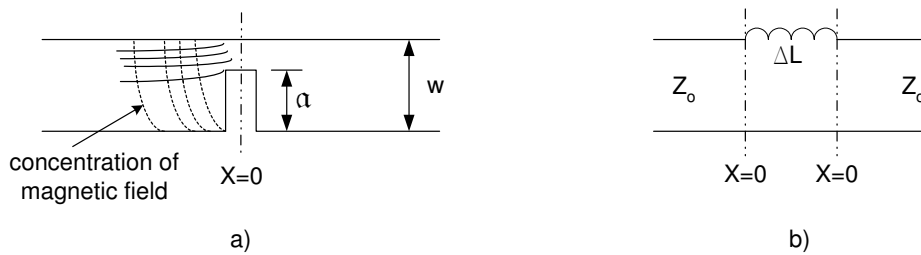


**Figure 4.5:** A microstrip line with a narrow slit (a) and its equivalent circuit (b).

Figure 4.5(a) illustrates the concentration of a magnetic field as a result of narrow slit cut into one side of a microstrip transmission line, and Figure 4.5(b) shows the corresponding equivalent circuit, where the value of the inductor $\Delta L$ is given as [15]

$$\Delta L = h\frac{\mu_o\pi}{2}\left(\frac{a}{W}\right)^2 \tag{4.2.9}$$

where $a/W$ and $h$ are respectively the relative penetration depth and substrate thickness.

Therefore, cutting a narrow slit into a T-junction can compensate the parasitic reactances associated with T-junction discontinuity. The compensation can be expressed mathematically as

$$2\pi f\Delta L - 2X_A = 0 \tag{4.2.10}$$

Substuting eqn. (4.2.9) into eqn. (4.2.10) yields the relative penetration depth (a/W) as

$$\frac{a}{W} = \frac{1}{\pi}\sqrt{\frac{2X_A}{\mu_o hf}} \tag{4.2.11}$$

### 4.2.4 Design and Implementation

#### 4.2.4.1 Conventional $0^o/180^o$ Microwave Hybrid Circuit

Figure 4.6 shows the layout of a 3GHz conventional $0^o/180^o$ microwave hybrid fabricated on a 0.787mm GIL substrate with 3.86 dielectric constant. The dimensions were calculated with the aid of TXLINE [16] and the design was first simulated using a built in mathematical model of Microwave Office (MWO) [16].
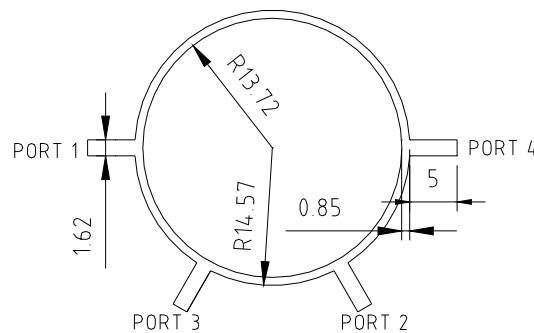


**Figure 4.6:** Layout of the 3GHz conventional $0^o/180^o$ microwave hybrid (dimenions are all in mm)

Since MWO doesn't include a footprint for the simulated $0^o/180^o$ microwave hybrid model, another $0^o/180^o$ microwave hybrid was designed by connecting microstrip transmission lines as shown in 4.9, where compensated T-junctions were also used at all ports.

### 4.2.4.2   Modified $0^o/180^o$ Microwave Hybrid Circuit

In order to compensate the parasitic capacitances associated with a T-junction discontinuity, a triangular slit was cut off from the side across the main-feed of the T-junction [17] shown in Figure 4.7. In order to obtain optimum compensation, the T-junction was first optimized in MWO for different values of $a$ and $\Psi$.
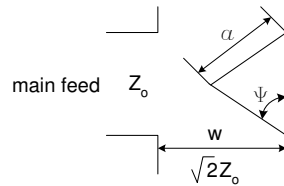


**Figure 4.7:** Compensated T-junction.

The simulation results are shown in Figure 4.8, where the bottom right plot of Figure 4.8 compares the reflection coefficient of the uncompensated T-junction with the best compensations obtained in the other three plots. The theoretical best match at the main feed of a T-junction is -9.5dB (when all ports terminated with a 50$\Omega$ load). At low frequency, the effect of the discontinuity is hardly noticeable for all compensations considered. However, as the frequency increases the effect becomes visible and the compensation becomes important. The best compensation was obtained for $\Psi = 45^o$ and $a = 0.9W$.
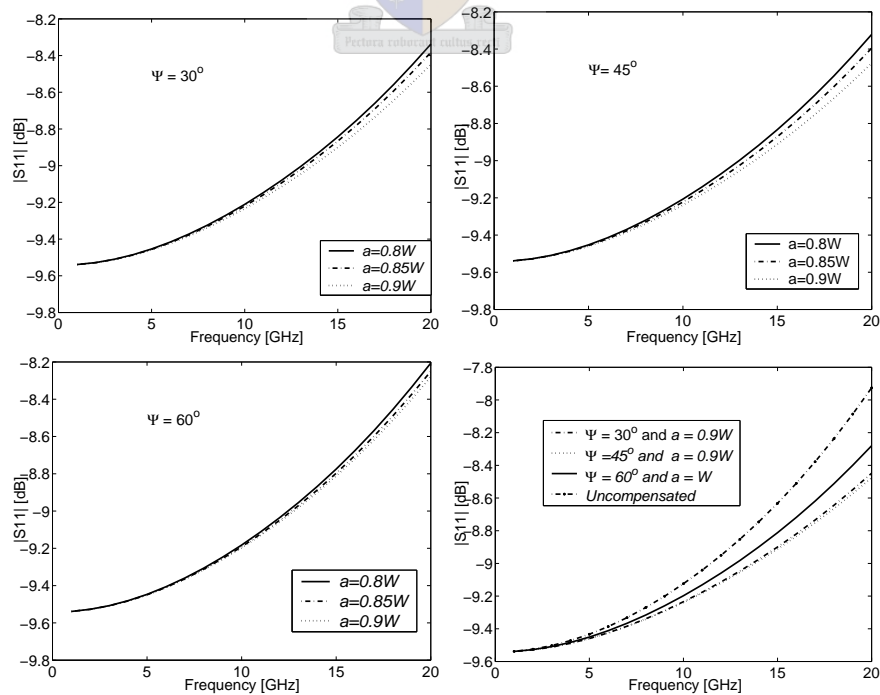


**Figure 4.8:** Simulated reflection coeffcient at the main feed of Figure 4.7.

The layout of the modified $0^o/180^o$ microwave hybrid circuit is shown in Figure 4.9 and it was fabricated using the same substrate used in the conventional $0^o/180^o$ microwave hybrid.
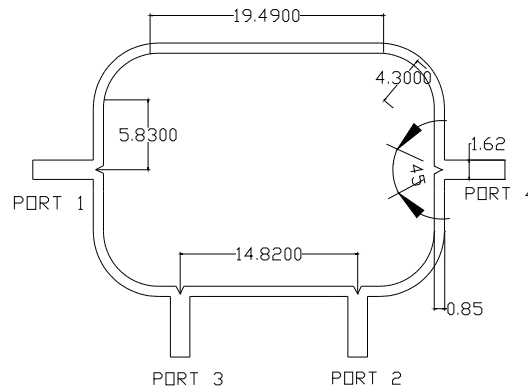


**Figure 4.9:** Layout of the 3GHz modified $0^o/180^o$ microwave hybrid (the dimensions are in mm).

### 4.2.5 Measurement and Discussion

The measured performance of the conventional $0^o/180^o$ microwave hybrid is shown in Figure 4.10, and simulation results are included in the same plot for comparison. The measurements were made using a calibrated HP8753C vector network analyzer (VNA) with two ports of the $0^o/180^o$ microwave hybrid appropriately terminated, while taking the measurements on the other two ports.
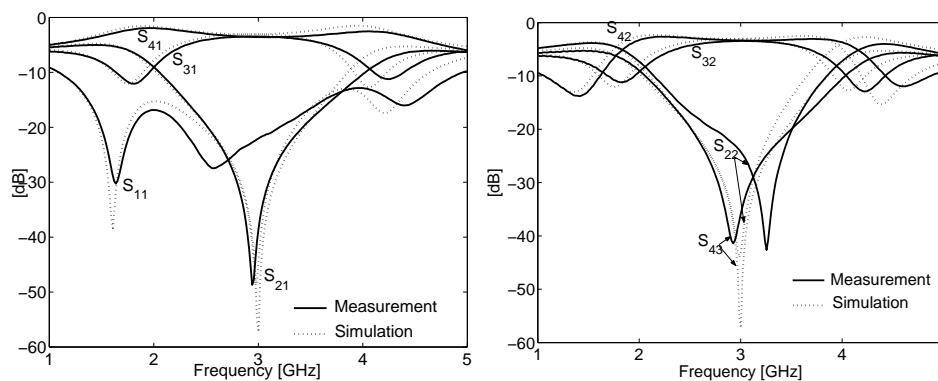


**Figure 4.10:** Simulated and measured S-parameters of the conventional $0^o/180^o$ microwave hybrid.

The measured results show good agreement with the simulated results in terms of power division (S41, S31, and S42, S32) and isolation (S21 and S43). Return losses at ports 1 and 2 (S11 and S22), however, have shifted respectively to the left and right of the designed center frequency of 3GHz. These shifts could be attributed to manufacturing inaccuracy. Figure

4.11 compares the simulated and measured phase differences of the sum (port 3) and difference (port 4) outputs of the conventional $0^o/180^o$ microwave hybrid, where a $1.8^o$ phase unbalance is recorded.
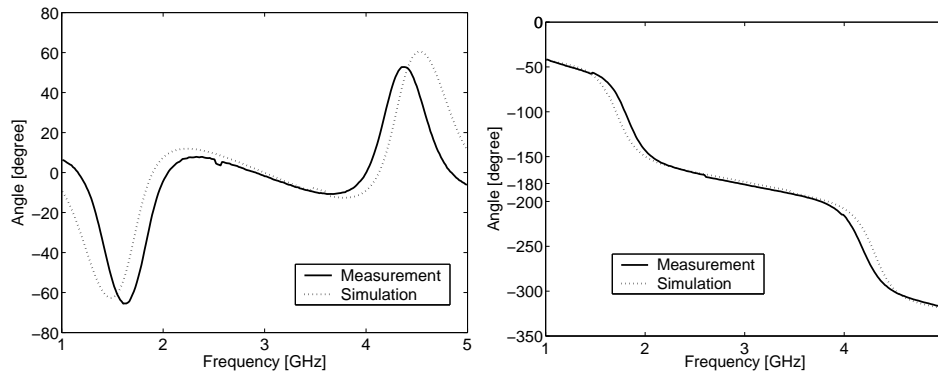


**Figure 4.11:** Phase difference at ports 3 and 4 of the conventional $0^o/180^o$ microwave hybrid.

Figure 4.12 compares the measured and simulated S-parameters of the modified $0^o/180^o$ microwave hybrid. The measurements show good agreement with the simulated results, except the measured isolation and port matching are 5dB below their respective simulated results. This discrepancy might be due to discontinuities at the SMA connector to microstrip transitions. Figure 4.13 compares the simulated and measured phase difference at the sum (port 3) and difference (port 4) outputs of the modified $0^o/180^o$ microwave hybrid. In each case the responses are almost indinguishable especially around the center frequency.
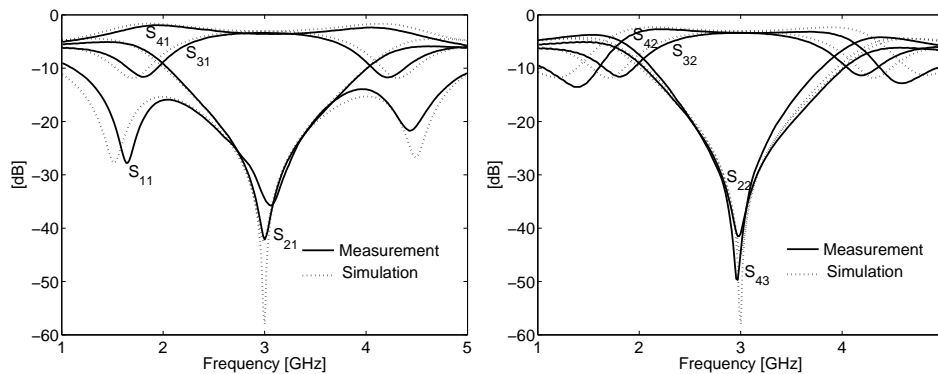


**Figure 4.12:** Simulation and measurement S-parameters of the modified $0^o/180^o$ microwave hybrid.

The phase differences at ports 3 and 4 are respectively summarized in Tables 4.1 and 4.2 for the conventional and modified $0^o/180^o$ microwave hybrid. Apart from shifting in center frequency, the bandwidth (over $\pm1^o$) of the modified $0^o/180^o$ microwave hybrid is improved by 13MHz compared to that of the conventional $0^o/180^o$ microwave hybrid.
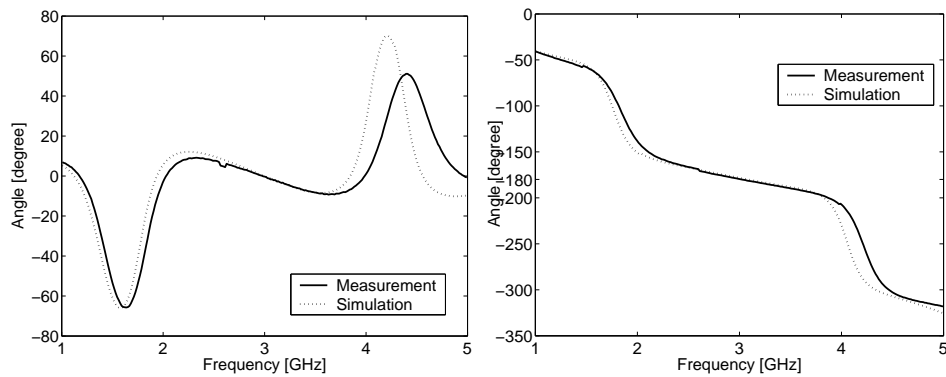
**Figure 4.13:** Phase difference at the sum and difference ports of the modified $0^o/180^o$ microwave hybrid.

| Frequency [GHz] | 2.852 | 2.882 | 2.912 | 2.942 | 2.972 | 3.0020 | 3.0310 |
|---|---|---|---|---|---|---|---|
| Conventional [degree] | 0.9278 | 0.5091 | 0.0531 | -0.5429 | -1.2094 | -1.2094 | -2.1815 |
| Modified [degree] | 2.3781 | 1.8120 | 1.2332 | 0.6136 | 0.1864 | -0.2986 | -1.0793 |

**Table 4.1:** Measured phase difference at port 3.

| Frequency [GHz] | 2.912 | 2.942 | 2.972 | 3.0020 | 3.0310 | 3.0610 | 3.0910 |
|---|---|---|---|---|---|---|---|
| Conventional [degree] | -179.32 | -179.86 | -180.51 | -181.15 | -181.90 | -182.59 | -183.15 |
| Modified [degree] | -177.62 | -178.27 | -178.90 | -179.62 | -180.29 | -180.80 | -181.59 |

**Table 4.2:** Measured phase difference at port 4.
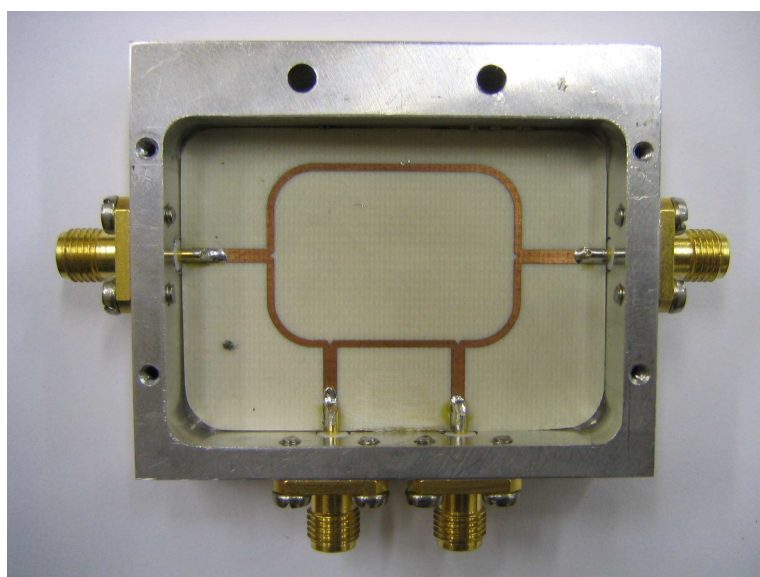


**Figure 4.14:** A photograph of the final modified $0^o/180^o$ microwave hybrid.

### 4.2.6 Conclusion

In this section, two $0^o/180^o$ microwave hybrids have been designed and tested. Though the measured performances of both $0^o/180^o$ microwave hybrids show good agreements with the simulated results, the modified $0^o/180^o$ microwave hybrid out performs the conventional counterpart in terms of retun loss, phase unbalance and bandwidth. A photograph of the modified $0^o/180^o$ microwave hybrid is shown Figure 4.14.

## 4.3 Design of Microwave Filters

### 4.3.1 Introduction

Microwave filters are vital sub-systems of the PCM radar receiver. Two microwave filters, a parallel-coupled microstrip-line filter [18] and a combline filter [19] were designed for the RF section (3GHz) and $1^{st}$ IF section (1.1GHz) of the PCM radar receiver. The RF filter protects the active sub-systems of the receiver from being over driven by out of band signals, whereas the $1^{st}$ IF filter attenuates unwanted frequencies generated within the $1^{st}$ mixer.

### 4.3.2 Design of a Parallel-Coupled Microstrip-Line Filter at 3GHz

#### 4.3.2.1 Introduction

The basic configuration of a parallel-coupled microstrip-line bandpass filter is shown in Figure 4.15. It consists of n+1 coupled-lines connected next each other, where n is the order of the filter. The lines are quarter-wavelength long at the midband frequency and coupling is achieved by way of fringing fields between neighbouring lines.
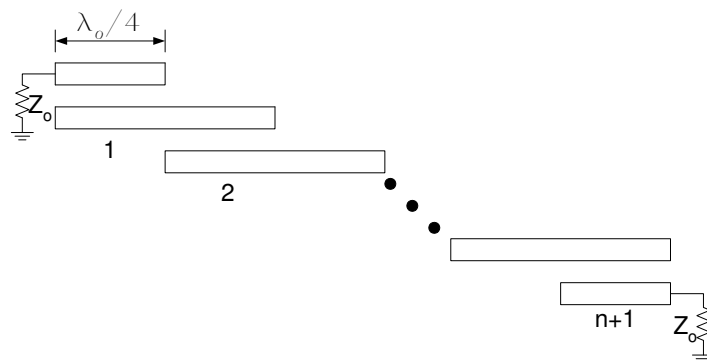


**Figure 4.15:** Layout of an $n^{th}$ order parallel coupled line filter.

### 4.3.2.2  Equivalent Circuit

Figure 4.16 shows a coupled-line with diagonal ports open-circuited. The impedance matrix of the coupled-lines is derived by Jones and Bolljahan [20] as

$$
\begin{bmatrix} V_1 \\ V_3 \end{bmatrix} = \begin{bmatrix} \frac{Z_{oe}+Z_{oo}}{2S} & \frac{Z_{oe}-Z_{oo}}{2S}\sqrt{1-S^2} \\ \frac{Z_{oe}-Z_{oo}}{2S}\sqrt{1-S^2} & \frac{Z_{oe}+Z_{oo}}{2S} \end{bmatrix} \begin{bmatrix} I_1 \\ I_3 \end{bmatrix}
\tag{4.3.1}
$$

where $Z_{oe}$ and $Z_{oo}$ are respectively the even and odd mode characteristic impedances.
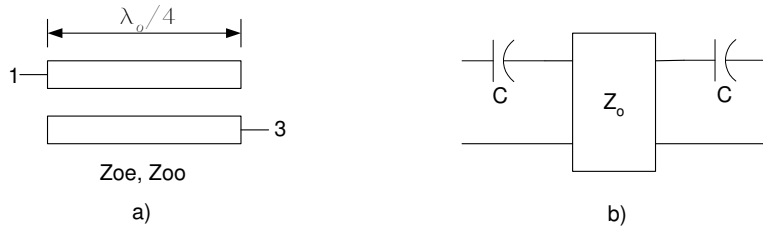


**Figure 4.16:** (a) Diagonal ports open-circuited coupled-line (b) its equivalent circuit.

From Figure 4.16(b), the ABCD matrix of the coupled-line is given by

$$
T = \frac{1}{\sqrt{1-S^2}} \begin{bmatrix} 1+\frac{1}{CZ_o} & \frac{2}{SC}+\frac{1}{SC^2 Z_o}+Z_o S \\ \frac{S}{Z_o} & 1+\frac{1}{CZ_o} \end{bmatrix}
\tag{4.3.2}
$$

where C is series capacitance and $Z_o$ is the characteristic impedance of the unit element.

The equivalent impedance matrix of eqn. (4.3.2) is calculated as

$$
[Z] = \begin{bmatrix} \frac{Z_o\left(1+\frac{1}{CZ_o}\right)}{S} & \frac{Z_o}{S}\sqrt{1-S^2} \\ \frac{Z_o}{S}\sqrt{1-S^2} & \frac{Z_o\left(1+\frac{1}{CZ_o}\right)}{S} \end{bmatrix}
\tag{4.3.3}
$$

Eqns. (4.3.1) and (4.3.3) are electrically equivalent. Thus,

$$
Z_{oe} + Z_{oo} = 2Z_o\left(1+\frac{1}{CZ_o}\right)
\tag{4.3.4}
$$

and

$$
Z_{oe} - Z_{oo} = 2Z_o
\tag{4.3.5}
$$

Simultaneously solving eqn.(4.3.4) and eqn. (4.3.5) results in

$$
Z_{oe} = 2Z_o + \frac{1}{C}
\tag{4.3.6}
$$

$$
Z_{oo} = \frac{1}{C}
\tag{4.3.7}
$$

Therefore, if coupling exists between adjacent sections only, the equivalent circuit of the $n^{th}$ order parallel-coupled microstrip-line filter shown in Figure 4.15 can be derived as shown in Figure 4.17.
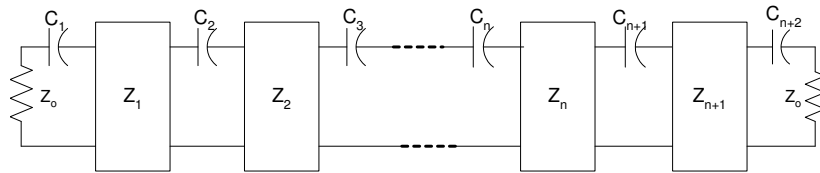


**Figure 4.17:** Equivalent circuit of the parallel-coupled microstrip-line filter.

Leaving the central capacitor in its original position, the equivalent circuit in Figure 4.17 can be simplified further using the Kuroda identity [18] shown in Figure 4.18. The unit elements are transformed out towards the ports, and the transformers resulting from each transformation cancel each other out. The resulting equivalent circuit is shown in Figure 4.19.
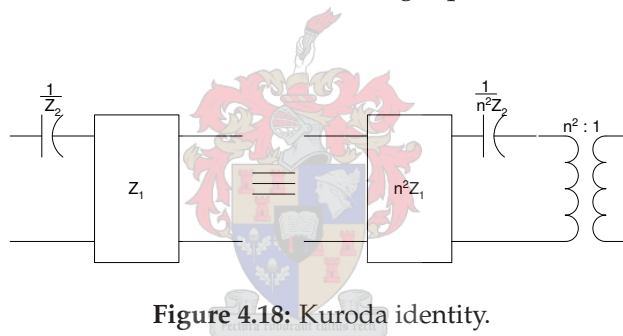


**Figure 4.18:** Kuroda identity.
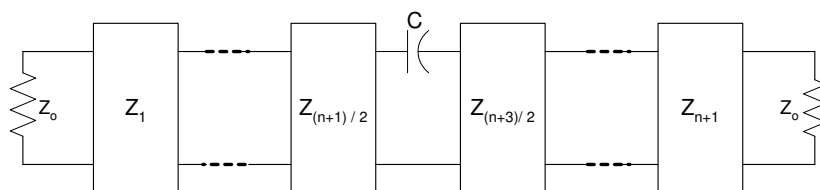


**Figure 4.19:** Simplified equivalent circuit for an $n^{th}$ order parallel-coupled microstrip-line filter.

### 4.3.2.3 Richards' Transformation

Richards' transformation is given by [21],

$$S = j\Omega = j\tan\theta \tag{4.3.8}$$

where $\theta$ is given by

$$\theta = \beta\ell \tag{4.3.9}$$

where $\ell$ and $\beta$ are the electrical length and propagation constant of the transmission line, respectively.

Substituting $\beta = 2\pi/\lambda$ and $\ell = \lambda_o/4$ into eqn. (4.3.9) results in

$$\theta = \frac{\pi\lambda_o}{2\lambda} \tag{4.3.10}$$

Since the propagation velocity, $v = f\lambda$, Richards' transformation for quarter wavelength is given by

$$\Omega = \tan\left(\frac{\pi f}{2f_o}\right) \tag{4.3.11}$$

Eqn. (4.3.11) is graphically illustrated in Figure 4.20, where a highpass response is mapped to a periodic bandpass response with the second passband centered at three times the center frequency of the first passband.
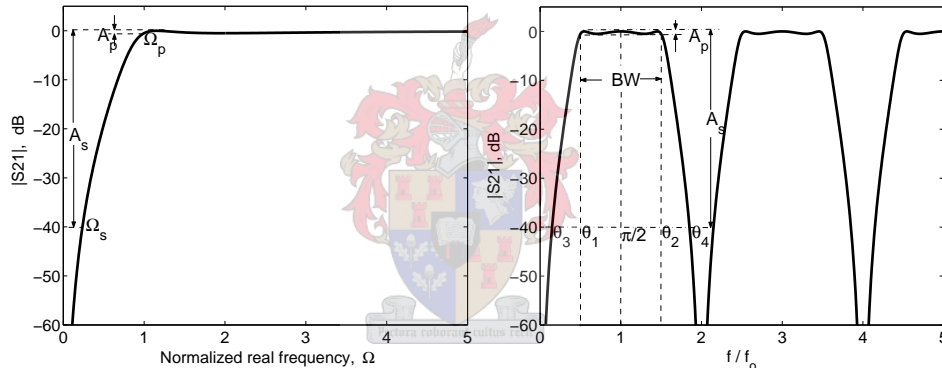


**Figure 4.20:** Richards' highpass transformation.

The first response of the mapping is symmetrical about $\theta = \pi/2$. Thus,

$$\theta_2 - \frac{\pi}{2} = \frac{\pi}{2} - \theta_1 \tag{4.3.12}$$

Eqn. (4.3.12) can be rewritten as

$$\theta_1 + \theta_2 = \pi \tag{4.3.13}$$

The percent bandwidth BW is given by

$$BW = \frac{\theta_2 - \theta_1}{\pi/2}100 \tag{4.3.14}$$

Simultaneously solving eqn. (4.3.13) and eqn. (4.3.14) yields

$$\theta_1 = \left(1 - \frac{BW}{200}\right)\frac{\pi}{2} \tag{4.3.15}$$

Substituting eqn. (4.3.15) into eqn. (4.3.8) yields the corresponding cut off frequency, $\Omega_p$ of the highpass prototype filter.

$$\Omega_p = \tan\left[\left(1 - \frac{BW}{200}\right)\frac{\pi}{2}\right] \tag{4.3.16}$$

Thus, the specifications of the prototype highpass filter can be determined using eqns. (4.3.11) and (4.3.16).

### 4.3.2.4  Design and Implementation

The design specifications of the bandpass filter are summarized in Table. 4.3.

| | |
|---|---|
| Center frequency, $f_o$ | 3GHz |
| Bandwidth, BW | 10% |
| Passband return loss, RL | 20dB |
| Stopband insertion loss, $A_s$ | 40dB for $f < f_s = 2GHz$ |

**Table 4.3:** Parallel-Coupled-line bandpass filter specification

The first step in the design of parallel-coupled-line filter is to obtain a suitable highpass prototype filter that would yield the desired bandpass specification. Table 4.4 summarizes the specifications for the highpass prototype as obtained using eqns. (4.3.11) and (4.3.16).

| | |
|---|---|
| Passband cutoff frequency, $\Omega_p$ | 12.7062rad/sec |
| Stopband cutoff frequency, $\Omega_s$ | 1.732rad/sec |
| Maximum passband ripple, $A_p$ | 0.04321dB |
| Stopband insertion loss, $A_s$ | 40dB |

**Table 4.4:** Highpass prototype filter specification.

The order of a highpass Chebychef prototype filter is given by [22]

$$\begin{aligned} n &\geq \frac{\cosh^{-1}\sqrt{(10^{40/10} - 1)/(10^{0.04321/10} - 1)}}{\cosh^{-1}(12.7062/1.7321)} \\ &\geq 2.835 \end{aligned} \tag{4.3.17}$$

Thus, a $3^{rd}$ highpass prototype filter shown in Figure 4.21 was synthesized with the aid of filter synthesis program ZSYN [23] and the element values are summarized in Table 4.5.

Since, the addition unit elements at ports don't change the amplitude response of the filter [20], two unit elements of unity charateristic impedance are added at the input and output ports of the prototype filter as shown in Figure 4.22.

| Element | Value |
|---------|-------|
| C | $6.05452647784476 \times 10^{-4}$ |
| Z | $10.8890571530265$ |

**Table 4.5:** Normalized element values for the $3^{rd}$ order highpass prototype filter.
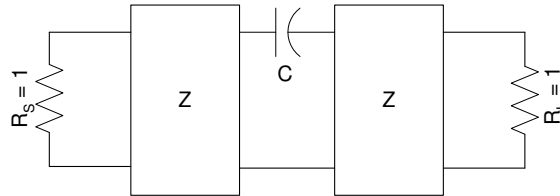


**Figure 4.21:** $3^{rd}$ order highpass prototype filter.
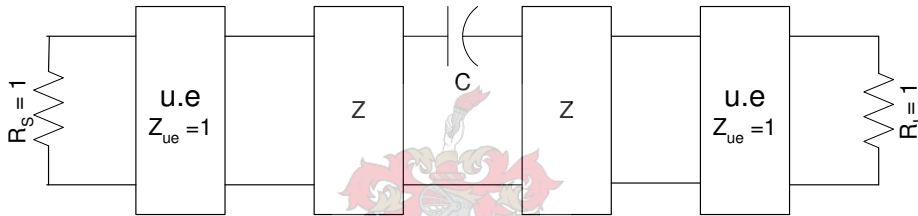


**Figure 4.22:** Highpass prototype filter with added unit elements.

Figure 4.23 shows the equivalent circuit of a symmetrical $3^{rd}$ order parallel-coupled microstrip-line filter.
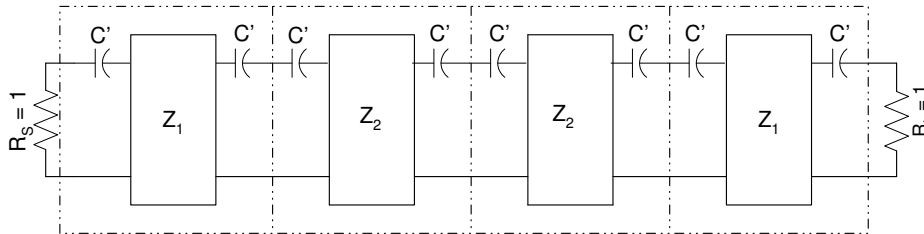


**Figure 4.23:** Equivalent circuit of a symmetrical $3^{rd}$ order parallel-coupled-line filter.

The elastance matrices [24] of Figure 4.23 and Figure 4.22 are respectively given by

$$\begin{bmatrix} Z_1 + 1/C' & -Z_1 & 0 & 0 & 0 \\ -Z_1 & Z_1 + Z_2 + 2/C' & -Z_2 & 0 & 0 \\ 0 & -Z_2 & 2Z_2 + 2/C' & -Z_2 & 0 \\ 0 & 0 & -Z_2 & Z_1 + Z_2 + 2/C' & -Z_1 \\ 0 & 0 & 0 & -Z_1 & Z_1 + 1/C' \end{bmatrix} \quad (4.3.18)$$

and

$$
\begin{array}{c}
\quad n_1 \quad\quad n_2 \quad\quad n_3 \quad\quad n_4 \quad\quad n_5 \\
\quad \downarrow \quad\quad \downarrow \quad\quad \downarrow \quad\quad \downarrow \quad\quad \downarrow \\
\begin{matrix}
n_1 \rightarrow \\
n_2 \rightarrow \\
n_3 \rightarrow \\
n_4 \rightarrow \\
n_5 \rightarrow
\end{matrix}
\left[
\begin{array}{ccccc}
1 & -1 & 0 & 0 & 0 \\
-1 & 1+Z & -Z & 0 & 0 \\
0 & -Z & 2Z+1/C & -Z & 0 \\
0 & 0 & -Z & 1+Z & -1 \\
0 & 0 & 0 & -1 & 1
\end{array}
\right]
\end{array}
\tag{4.3.19}
$$

In order to obtain a configuration similar to Figure 4.23 and evenly distribute the central capacitance, the rows and corresponding columns of eqn. (4.3.19) are multiplied using arbitrary constants, $n_1, \ldots, n_5$. The outer constants $n_1$ and $n_5$ are set to unity in order to maintain the amplitude response of the filter, whereas $n_2 = n_4$ to keep the symmetry. Thus, for eqn. (4.3.18) and eqn. (4.3.19) (after transformation) to be identical, the corresponding entries must be the same. That is,

$$
1 - n_2 = 1/C' \tag{4.3.20}
$$

$$
-n_2 + n_2(1+Z) - n_2 n_3 Z = 2/C' \tag{4.3.21}
$$

$$
-n_2 n_3 Z + n_3^2(2Z+1/C) - n_2 n_3 Z = 2/C' \tag{4.3.22}
$$

Simultaneously solving eqns. (4.3.20) to (4.3.22) and substituting the values of Z and C yields,

$$
C' = 1.62129
$$

$$
n_2 = 0.383206
$$

$$
n_3 = 0.029868
$$

Comparing eqn. (4.3.18) and eqn. (4.3.19) again yields,

$$
Z_1 = n_2 = 0.383206
$$

$$
Z_3 = n_2 n_3 Z = 0.124044
$$

Table 4.6 summarizes the even and odd mode impedances calculated using the values of C', $Z_1$ and $Z_2$ substituted into eqns. (4.3.6) and (4.3.7).

| | $Z_{oe}$ | $Z_{oo}$ |
|---|---|---|
| section 1 and 4 | 69.1354 | 30.8646 |
| section 2 and 3 | 43.2690 | 30.8646 |

**Table 4.6:** Even and odd impedances in a 50$\Omega$ system.

With the aid of synthesis program LINCALC [25], the dimensions of the filter: width and spacing between the lines are summarized in Table 4.7. The synthesis was performed on a 0.635mm and $\epsilon_r$ of 10.2 Rogers substrate.

| Width 1, 4 [mm] | 0.487002 |
|---|---|
| Width 2, 3 [mm] | 0.967848 |
| Spacing 1, 4 [mm] | 0.151774 |
| Spacing 2, 3 [mm] | 0.470748 |

**Table 4.7:** Dimensions of the parallel-coupled microstrip-line filter.

The length of the lines (10.2mm) was calculated using TXLINE. Since the characteristic impedance and propagation constant of microstrip lines are functions of frequency, the filter was first simulated and optimized in MWO. The complete layout of the parallel-coupled microstrip line filter is shown in Figure 4.24.
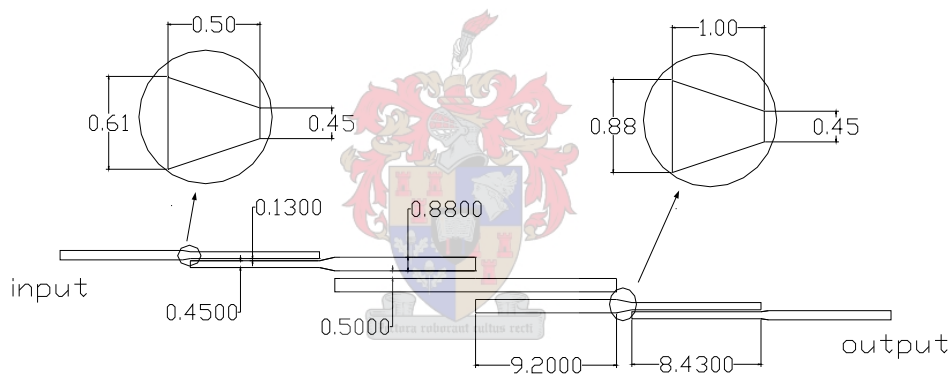


**Figure 4.24:** Layout of the 3GHz parallel-coupled microstrip-line filter.

Short transmission lines, as shown in Figure 4.24, are included for practical realization and reduce the parasitics associated with a sudden change in width. Besides, a 50Ω transmission line is added at both ports to keep the connector to microstrip transitions away from the filter and effectively eliminate higher order mode propagation.

### 4.3.2.5  Measurement and Discussion

The designed filter is measured using a calibrated HP8753C VNA and Figure 4.25 plots the measurement results along with the simulation. The measured passband is centered at 2.94GHz, which is off by 60MHz from the designed center frequency. The fringing capacitance at the open ends each resonator and accuracy of the dielectric constant of the substrate are responsible for lowering the center frequency of the filter. The measured insertion loss and port matching across the passpand bandwidth are respectively 1.25dB and 18.2dB. This inferior performance of the measured return loss over its simulated counterpart is inevitable

because of the discontinuities associated with coaxial to microstrip line transitions at the ports.
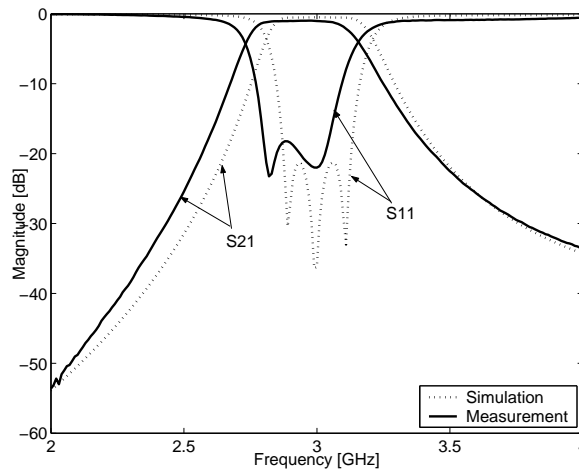


**Figure 4.25:** Simulated and measured response of the first parallel-coupled microstrip-line filter.

Thus, a second filter was reconstructed with open ends cut back by 0.2mm in order to compensate the specified shift in the center frequency. Measurement results of the second filter along with the simulation are plotted in Figure 4.26, where the passband is centered at 3GHz, and the return and insertion loss are respectively 15dB and 1dB across the passband.
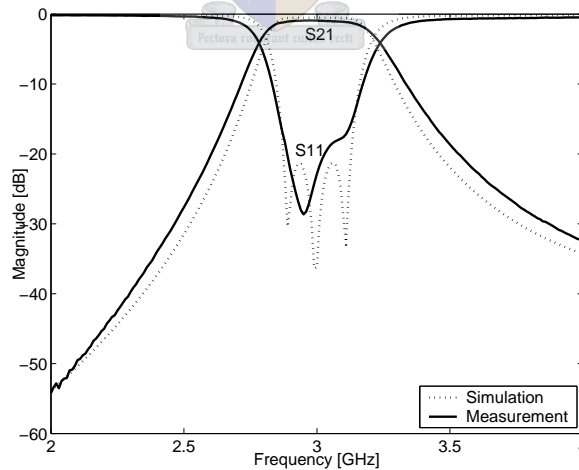


**Figure 4.26:** Simulated and measured response of the modified parallel-coupled microstrip-line filter.

### 4.3.2.6   Conclusion

In this section, two parallel-coupled microstrip-line filters were designed at 3GHz using the equivalent circuit technique. Only 0.2mm adjustments were made to the dimensions of the first filter so as to compensate for the shift in the center frequency. In order to reduce

interference the modified filter was packaged in an aluminum box as shown in Figure 4.27.
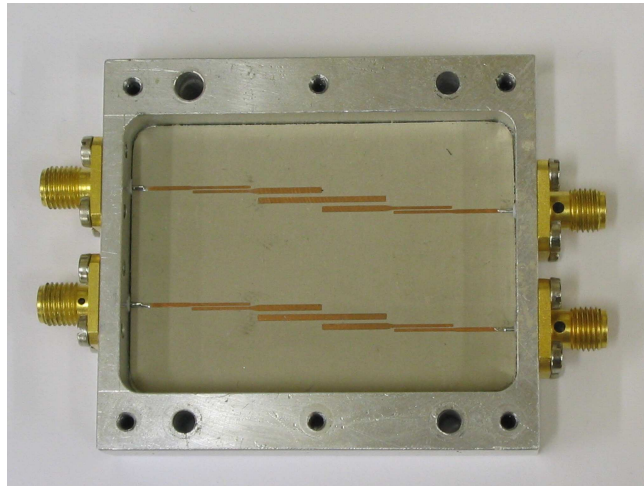


**Figure 4.27:** A photograph of the $3^{rd}$ order parallel-coupled microstrip-line filter.

### 4.3.3 Design of a Combline Filter at 1.1GHz

#### 4.3.3.1 Introduction

Filters that can be designed in the frequency range of 1.1GHz (for the $1^{st}$ IF section of the PCM radar receiver) include lumped element, surface acoustic wave (SAW), interdigital and combline filters [19, 26]. Because of its compactness and ease of fabrication a lumped element bandpass filter was designed as a first choice. However, the measured results failed to meet the design specifications and thus, a combline filter was designed as a second choice. The design and measurement results of the lumped element bandpass filter is available in appendix B.
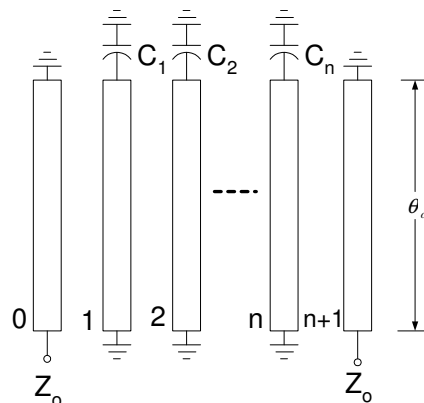


**Figure 4.28:** Combline filter configuration.

Besides its compactness, a combline filter can provide excellent performance with strong stopband rejection and low passband insertion loss [19, 27]. Figure 4.28 shows a basic configuration of an $n^{th}$ order combline filter, which consists of $n$ resonators and input and output transformers. The resonators form an array of transmission lines with one end short-circuited to ground and lumped capacitors $C_1...C_n$ between the other end and ground. Lines 0 and n+1 are part of the impedance-transforming sections.

In a combline filter coupling is achieved by way of the fringing fields between neighboring resonators. With the absence of the lumped capacitors, the resonators would be $\lambda_o/4$ long at resonance and the magnetic and electric couplings would cancel each other out to leave in an all stop response [19]. However, with the lumped capacitors $C_i$ included, resonance occurs at less than $\lambda_o/4$ and coupling between the resonators becomes predominantly magnetic. Besides having efficient coupling between resonators, sufficiently large lumped capacitance ensures resonance to occur at less than $\lambda_o/8$, which makes combline filters suitable for L-band applications.

### 4.3.3.2  Richards' Transformation

The first step in the design of a combline filter is to obtain a suitable prototype structure, which will yield the specified distributed filter. Using Richards' transformation (for $\ell = \lambda_o/8$) [21],

$$\Omega = \tan\left(\frac{\pi f}{4f_o}\right) \tag{4.3.23}$$

a bandpass prototype is mapped to exactly the same but periodic response in a distributed realization as illustrated in Figure 4.29. The second passband is centered four times away from the center of the first passband and can be removed further by for shortening the resonators and accordingly using large lumped capacitors.
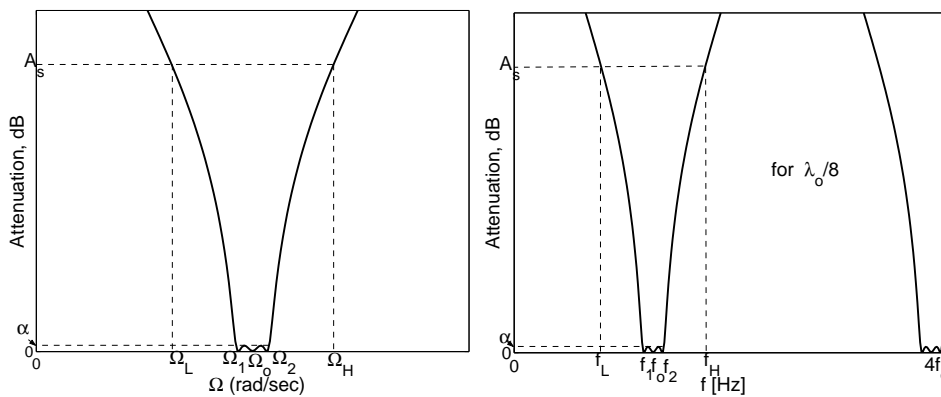


**Figure 4.29:** Richards' transformation for $\ell = \lambda_o/8$.

### 4.3.3.3 Equivalent Circuit

With the assumption that coupling only exists between adjacent resonators, an $n^{th}$ order combline filter comprises two types of coupled lines: the same side short-circuited coupled-lines which exists between the resonators; and opposite side short-circuited coupled-lines which exists between end resonators and port transformers. These coupled lines are shown in Figures 4.30 and 4.31 along with their respective equivalent circuits [28, 18].
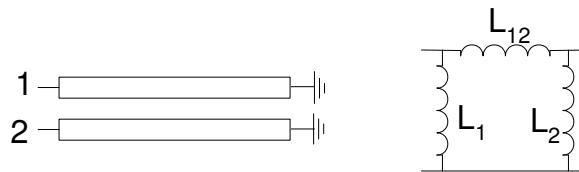
**Figure 4.30:** The same side short-circuited coupled line.
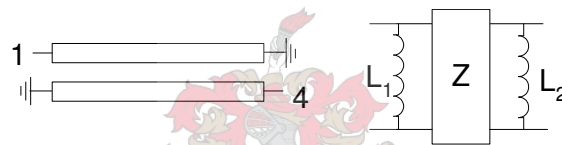
**Figure 4.31:** Opposite side short-circuited coupled line.

Figure 4.32 shows the equivalent circuit of a combline filter obtained by cascading the above equivalent circuits of adjacent coupled lines and lumped capacitors. Applying Kuroda transformation (Figure 4.33) at both ends of the equivalent circuit and performing simple circuit transformations yields the network shown in Figure 4.34.
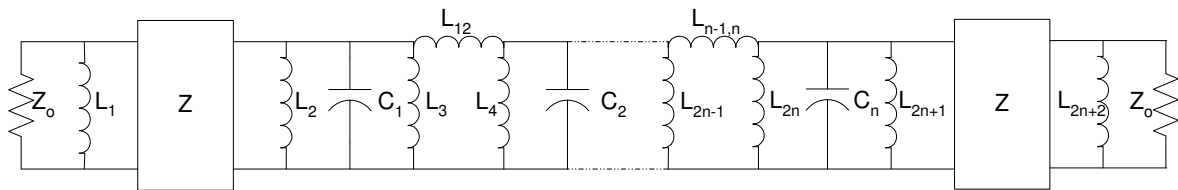
**Figure 4.32:** Equivalent circuit for the combline filter.
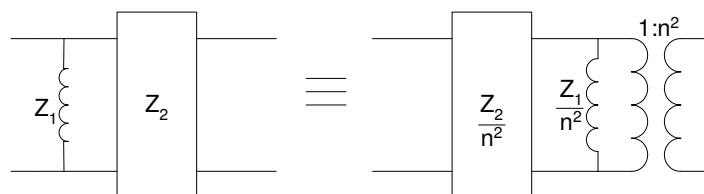
**Figure 4.33:** Kuroda's identity.
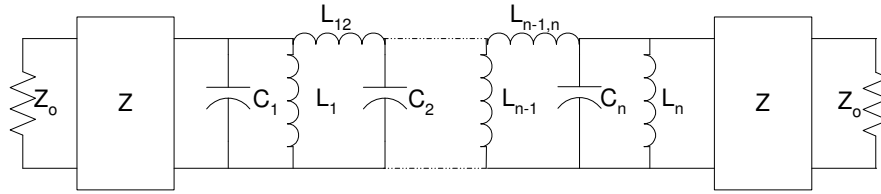
**Figure 4.34:** Equivalent circuit after elimination of the resulting transformers.

In non-redundant form, where there are no adjacent components of the same type, the above equivalent circuit is reduced to the equivalent circuit shown in Figure 4.35. The non-redundant equivalent circuit contains 2n-1 low-pass elements and one high-pass element. Therefore, the attenuation of a combline filter on the high side of the passband is steeper than the low side.
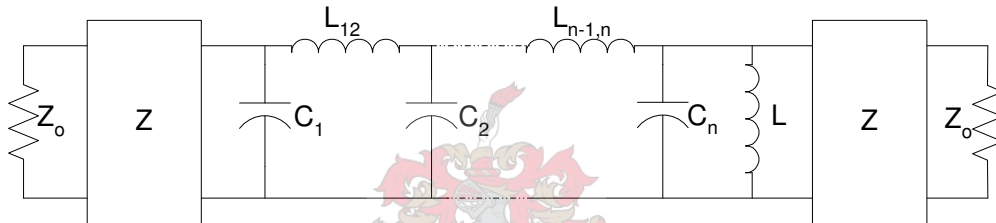


**Figure 4.35:** Combline line filter equivalent circuit in non-redundant form.

#### 4.3.3.4   Capacitance Matrix and Transformation

The array of transmission lines of a combline filter can be described in terms of a capacitance network as shown in Figure 4.36, and the corresponding capacitance matrix [29] is given by

$$[C] = \begin{bmatrix} C_0 + C_{01} & -C_{01} & 0 & 0 & \cdots & 0 \\ -C_{01} & C_{01} + C_1 + C_{12} & -C_{12} & 0 & \cdots & 0 \\ 0 & -C_{12} & C_{12} + C_2 + C_{23} & -C_{23} & \cdots & 0 \\ \vdots & & & \ddots & & \vdots \\ 0 & 0 & 0 & 0 & -C_{n,n+1} & C_{n+1} + C_{n,n+1} \end{bmatrix}$$

$$(4.3.24)$$

where the sum of all capacitances surrounding a specified node appear on the diagonal while the negative of the fringing capacitances are found above or below the diagonal entries. Adding any row or column of the capacitance matrix gives the shunt capacitance to ground of that particular resonator. Since the capacitance network is directly related to the size of the resonators and spacing of the combline filter, it can be linearly transformed as

shown in eqn. (4.3.25) in order to obtain a realizable filter structure.
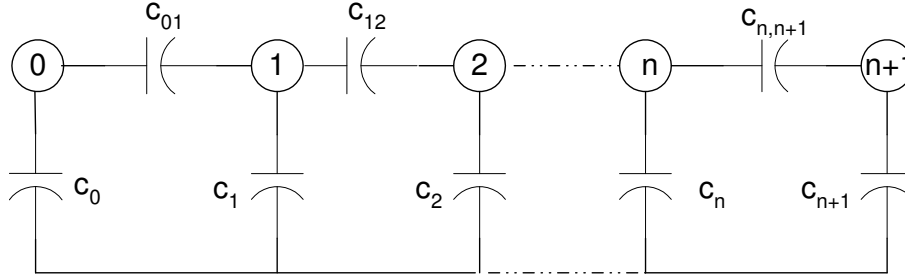


**Figure 4.36:** Capacitance network for combline filter.

$$[C] = \begin{array}{c} n_0 \rightarrow \\ n_1 \rightarrow \\ n_2 \rightarrow \\ n_3 \rightarrow \\ n_{n+1} \rightarrow \end{array} \begin{bmatrix} C_0 + C_{01} & -C_{01} & 0 & 0 & \cdots & 0 \\ -C_{01} & C_{01} + C_1 + C_{12} & -C_{12} & 0 & \cdots & 0 \\ 0 & -C_{12} & C_{12} + C_2 + C_{23} & -C_{23} & \cdots & 0 \\ \vdots & & & \ddots & & \vdots \\ 0 & 0 & 0 & 0 & -C_{n,n+1} & C_{n+1} + C_{n,n+1} \end{bmatrix}$$

$$(4.3.25)$$

The capacitance network shown in Figure 4.36 is directly derived from the prototype equivalent circuit shown in Figure 4.35 using the per unit capacitance given by [18]

$$C = \frac{\eta}{Z\sqrt{\epsilon_r}} \tag{4.3.26}$$

where $\eta$ is the free space characteristic impedance, $376.6\Omega$, $\epsilon$ is the relative permitivity of medium and Z is the impedance between the nodes or a node and ground.

### 4.3.3.5 Physical Implementation of Coupled Lines and Lumped Capacitances

Figure 4.37 shows a cross-sectional view of a combline filter. Applying the even and odd mode analysis [12] on adjacent coupled lines (i and i+1) yields the self and mutual static capacitances as,

$$c_i = c_e \tag{4.3.27}$$

and

$$c_{i,i+1} = 1/4(c_o - c_e) \tag{4.3.28}$$

where $c_e$ and $c_o$ are respectively the even and odd mode normalized capacitances and they are approximately given by [30]

$$\epsilon/c_e = \frac{1}{2\pi} \left| \ln \frac{\frac{\pi d}{4b}}{\sqrt{1 - (\frac{d}{2b})^4}} + \frac{1}{2} \ln \left[ 1 - \left( \frac{d/b}{2c/b} \right)^4 \right] + 2 \sum_{i=0}^{m} \ln \tanh m \frac{\pi c}{2b} \right| \qquad (4.3.29)$$

$$\epsilon/c_o = \frac{1}{2\pi} \left| \ln \frac{\frac{\pi d}{4b}}{\sqrt{1 - (\frac{d}{2b})^4}} - \frac{1}{2} \ln \left[ 1 - \left( \frac{d/b}{2c/b} \right)^4 \right] + 2 \sum_{i=0}^{m} (-1)^m \ln \tanh m \frac{\pi c}{2b} \right| \qquad (4.3.30)$$

where $m$ is the resonator number in the combline filter structure, d is the diameter of the rod, c spacing between the centers of the resonators and b is the spacing between the ground planes.
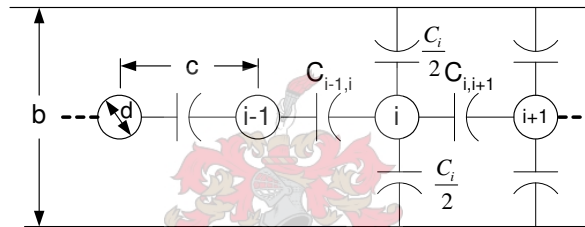


**Figure 4.37:** Cross-section view of a combline filter.

The lumped capacitors are realized using a gap created between the end of the resonators and ground as illustrated in Figure 4.38. Here C is equal to $\frac{\epsilon \pi d^2}{4t}$ and thus, large capacitance realization is extremely difficult.
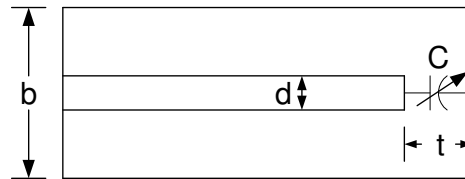


**Figure 4.38:** Lumped capacitance realization.

### 4.3.3.6 Bandwidth Correction Factor

Since Richard's transformation [21] deals only with distributed networks, the effect of the lumped capacitances used at the end of the resonators is invetigated in this section.

The total susceptance at the junction, 'J' of the combline resonator shown in Figure 4.39(a) is given by

$$B_{combline}(\omega) = \omega C - \frac{1}{Z_{osc} \tan \theta}$$

(4.3.31)

where $C$ is lumped capacitance, $Z_{osc}$ is the characteristic impedance of the short-circuited stub and $\theta$ is the angular length of the stub given by

$$\theta = \frac{\omega}{\omega_o} \theta_o$$

(4.3.32)

where $\theta_o$ is the length of the stub at resonance, $\omega = \omega_o$.
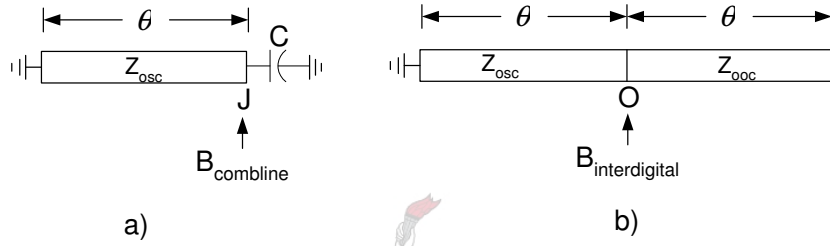


Figure 4.39: Resonators for combline filter (a) and interdigital filter (b).

At resonance $B_{combline}$=0, substituting eqn. (4.3.32) into eqn. (4.3.31) yields

$$C = \frac{1}{\omega_o Z_{osc} \tan \theta_o}$$

(4.3.33)

Substituting eqn.(4.3.32) and eqn.(4.3.33) into eqn.(4.3.31) yields the total suceptance of the combline resonator as a function of angular frequency,

$$B_{combline}(\omega) = \frac{1}{Z_{osc}} \left[ \frac{\omega}{\omega_o \tan \theta_o} - \cot \left( \frac{\omega}{\omega_o} \theta_o \right) \right]$$

(4.3.34)

Eqn. (4.3.34) has been plotted in Figure 4.40 for different values of $\theta_o$, where the slope at $\omega = \omega_o$ increases with $\theta_o$. Thus, the bandwidth of the combline resonator, for that matter the bandwidth of the filter, increases as $\theta_o$ decreases.

The total suceptance at point 'O' of the interdigital filter resonator shown in Figure 4.39(b) is given by

$$B_{interdgital} = \frac{\tan \theta}{Z_{ooc}} - \frac{1}{Z_{osc} \tan \theta}$$

(4.3.35)

At resonance $B_{interdigital}$= 0, eqn. (4.3.35) becomes

$$\frac{\tan \theta_o}{Z_{ooc}} = \frac{1}{Z_{osc} \tan \theta_o}$$
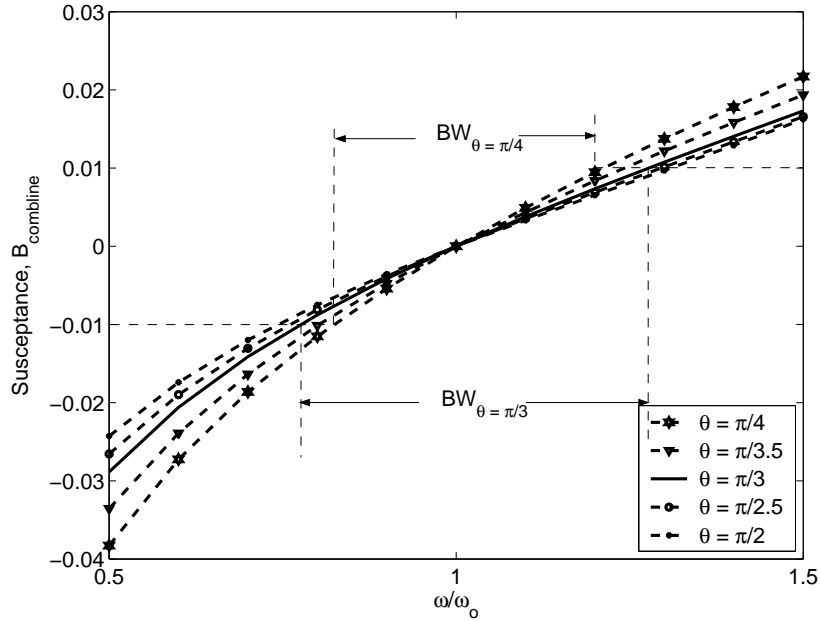
(4.3.36)

**Figure 4.40:** Susceptance of a combline filter resonator for different values of $\theta$.

Substuting eqn. (4.3.32) and eqn. (4.3.36) into eqn. (4.3.35) yields,

$$B_{interdigital}\left(\omega\right) = \frac{1}{Z_{osc}}\left[\frac{\tan\left(\frac{\omega}{\omega_o}\theta_o\right)}{\tan\theta_o} - \cot\left(\frac{\omega}{\omega_o}\theta_o\right)\right] \tag{4.3.37}$$

Eqns. (4.3.36) and (4.3.37) have been plotted in Fig.4.41, where it can be seen that the combline filter resonator has wider bandwidth than that of the interdigital filter. This stretch in bandwidth must be accounted for during cut off frequencies calculation using Richards' transformation.

The bandwidth correction factor can be determined from the ratio of the slopes of eqns. (4.3.36) and (4.3.37) at $\omega = \omega_o$,

$$K = \frac{\left[\frac{dB_{combline}(d\omega)}{\omega}\right]_{\omega=\omega_o}}{\left[\frac{dB_{interdigital}(\omega)}{d\omega}\right]_{\omega=\omega_o}} = \frac{\sin\theta_o\cos\theta_o}{2\theta_o} + 0.5 \tag{4.3.38}$$

The corrected bandwidth $BW_{design}$ is therefore given by

$$BW_{design} = K * BW_{spec} \tag{4.3.39}$$

where $BW_{spec}$ is the specified bandwidth of the filter.

The lower ($\Omega_1$) and upper ($\Omega_2$) cut off frequencies are then determined by substuting eqn. (4.3.39) into Richards' transformation. That is,

$$\Omega_1 \;\; = \;\; \tan\left(\theta_o\left[1 - \frac{KBW_{spec}}{2}\right]\right) \tag{4.3.40}$$

$$\Omega_2 \;\; = \;\; \tan\left(\theta_o\left[1 + \frac{KBW_{spec}}{2}\right]\right) \tag{4.3.41}$$
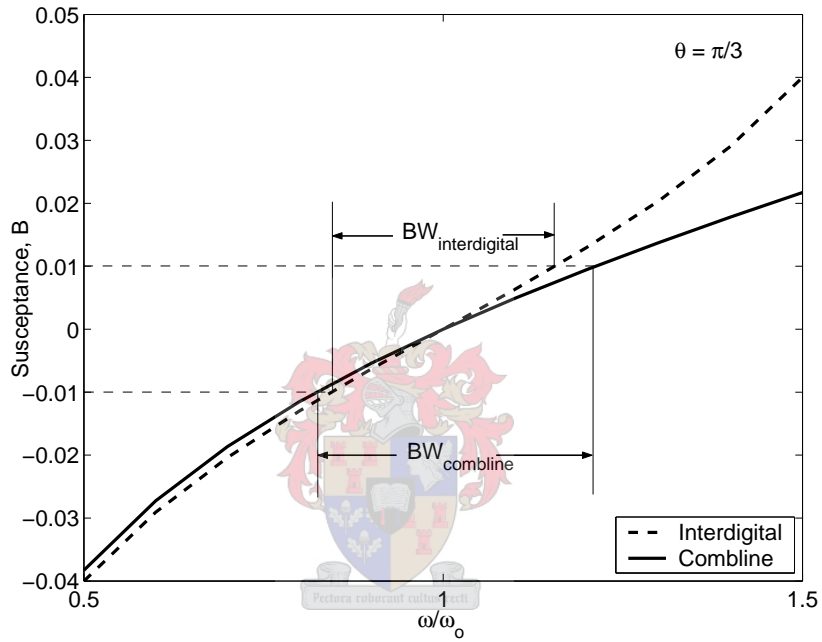


**Figure 4.41:** Susceptances of a combline and an interdigital filter resonators.

### 4.3.3.7   Temperature Coeffcient

In a combline filter, the resonance frequency is solely determined by the parallel combination of the lumped capacitance and short-circuited stub. However, due to the inherent thermal characteristics of the material used to construct the filter, the mechanical dimensions of the filter change with temperature which in turn causes a shift in the resonance frequency.

For a temperature change $\Delta T$, the diameter (d), and gap (t) of the end capacitance expand equally by linear coefficient of thermal expansion of the material, $\alpha$. Thus, the susceptance of the lumped capacitance is given by

$$Bc = 2\pi f_o C \left(1 + \Delta f / f_o\right)\left(1 + \alpha \Delta T\right) \tag{4.3.42}$$

where $\Delta f$ is a shift in resonant frequency.

At resonance, $f = f_o$, the susceptance of the lumped capacitor, $C$ is equal to the suceptance of the short-circuited stub,

$$2\pi f_o C = \frac{1}{Z_{0sc} \tan \theta_o} \tag{4.3.43}$$

Substituting eqn. (4.3.43) into eqn. (4.3.42) yields

$$Bc = \frac{(1 + \Delta f / f_o)(1 + \alpha \Delta T)}{Z_{0sc} \tan \theta_o} \tag{4.3.44}$$

The ground plane spacing, $b$ and diameter of the stubs, $d$ change equally by $\alpha$, leaving the characteristic impedance of the short-circuited stub, $Z_{osc}$ unchanged. The length of the stub, however, changes by $\alpha$. Thus, the susceptance of the shorted-circuited stub will be

$$B_r = \frac{1}{Z_{osc} \tan \left( \theta_o (1 + \Delta f / f_o)(1 + \alpha \Delta T) \right)} \tag{4.3.45}$$

At resonance, $f = f_o$, the susceptance of the short-circuited stub is equal to the susceptance of the lumped capacitance, implying the total suceptance of the resonator is zero,

$$\frac{(1 + \Delta f / f_o)(1 + \alpha \Delta T)}{Z_{0sc} \tan \theta_o} - \frac{1}{Z_{osc} \tan \left( \theta_o (1 + \Delta f / f_o)(1 + \alpha \Delta T) \right)} = 0 \tag{4.3.46}$$

If we let $x = (1 + \Delta f / f_o)(1 + \alpha \Delta T)$ eqn. (4.3.46) becomes

$$x \tan \left( \theta_o x \right) - \tan \theta_o = 0 \tag{4.3.47}$$

$x = 1$ is the solution of eqn. (4.3.47). Thus,

$$(1 + \Delta f / f_o)(1 + \alpha \Delta T) = 1 \tag{4.3.48}$$

Simplifying eqn. (4.3.48) yields,

$$\Delta f / f_o + \alpha \Delta T + \alpha \Delta T \Delta f / f_o = 0 \tag{4.3.49}$$

The contribution $\alpha \Delta T \Delta f / f_o$ is negligible. Thus, the change in resonance frequency, $\Delta f$ for $\Delta T$ in temperature is given by

$$\Delta f \approx -\alpha \Delta T f_o \tag{4.3.50}$$

The thermal expansion coefficient of brass and aluminum are respectively 19 and 24 ppm/°C. A 20°C rise in temperature of a 1100 MHz resonator will cause a change in resonant frequency of 0.627MHz and 0.792MHz for resonators made from brass and aluminum respectively.

### 4.3.3.8 Design

The specifications of the combline bandpass filter are summarized in Table 4.8.

| | |
|---|---|
| Center frequency, $f_o$ | 1.1GHz |
| Bandwidth, BW | 4% |
| Stopband | $f \geq f_o$+75MHz and $f \leq f_o$-75MHz |
| Passband return loss, RL | 20dB |
| Stopband insertion loss, $A_s$ | 40dB |

**Table 4.8:** Combline bandpass filter specification.

The first step in the design of combline filter is to determine the prototype bandpass filter using Table 4.8 and eqns. (4.3.38) to (4.3.41). The specifications of the bandpass prototype filter, for $\theta_o = \frac{\pi}{3}$, are as follows:

| | |
|---|---|
| Passband | 1.67435rad/sec$\leq \Omega \leq$ 1.79282 rad/sec |
| Stopband | $\Omega \leq$ 1.4775 rad/sec and $\Omega \geq$ 2.05859 rad/sec |
| Passband return loss, RL | 20dB |
| Stopband insertion loss, $A_s$ | 40dB |

**Table 4.9:** Bandpass prototype filter specifications.

Figure 4.42 shows a $6^{th}$ order bandpass prototype filter synthesized with the aid of synthesis program ZSYN. The values of the components are summarized in Table 4.10.
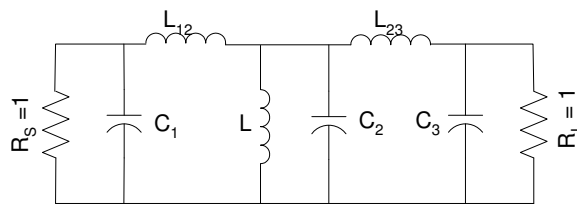


**Figure 4.42:** Bandpass prototype filter realized using ZSYN.

| Element Name | Element Value |
|---|---|
| $C_1$, $C_3$ | 1.44E+1 |
| $C_2$ | 1.16E+4 |
| $L_{12}$, $L_{23}$ | 2.313E-2 |
| L | 2.877E-5 |

**Table 4.10:** Bandpass prototype filter components values.

Two unit elements, each with a characteristic impedance $Z_o = 1$, are added at both ports of the prototype filter to realize the combline filter with input and output transformers. This is

illustrated in Figure 4.43.
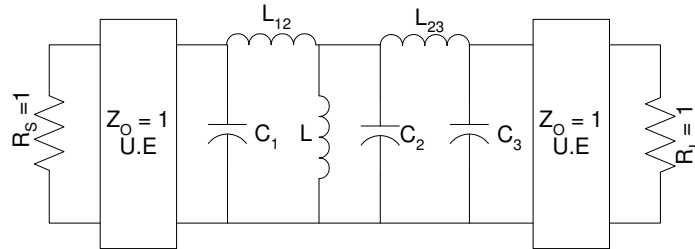


**Figure 4.43:** Bandpass prototype filter with input and output unit elements added.

Figure 4.44 shows the capacitance network of the prototype filter, and Table 4.11 summarizes the corresponding values calculated using eqn. (4.3.26) (for a 50$\Omega$ system).
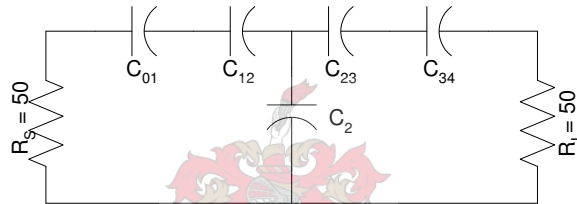


**Figure 4.44:** Prototype filter in capacitance configuration.

| Element Name | Element Value |
|---|---|
| $C_{01}$, $C_{34}$ | 7.534 |
| $C_2$ | 261834.0348 |
| $C_{12}$, $C_{23}$ | 325.7366 |

**Table 4.11:** Prototype filter capacitance values.

The capacitance matrix of Figure 4.44 is then given as

$$
[C] = \begin{array}{c} n_1 \rightarrow \\ n_2 \rightarrow \\ n_3 \rightarrow \\ n_4 \rightarrow \\ n_5 \rightarrow \end{array}
\begin{array}{ccccc} n_1 & n_2 & n_3 & n_4 & n_5 \\ \downarrow & \downarrow & \downarrow & \downarrow & \downarrow \end{array}
\left[ \begin{array}{ccccc}
7.5340 & -7.5340 & 0 & 0 & 0 \\
-7.5340 & 333.2706 & -325.7366 & 0 & 0 \\
0 & -325.7366 & 262485.5080 & -325.7366 & 0 \\
0 & 0 & -325.7366 & 333.2706 & -7.5340 \\
0 & 0 & 0 & -7.5340 & 7.5340
\end{array} \right]
\tag{4.3.51}
$$

The constants were chosen to be $n_1=n_5=1$, $n_2=n_4=0.12525$ and $n_3=0.0041185$, as the aim of the transformation is to achieve a physically realizable filter structure with equal resonator to ground capacitance. The transformed capacitance matrix is given in eqn. (4.3.52).

$$[c_r'] = \begin{bmatrix} 7.5340 & -0.94360 & 0 & 0 & 0 \\ -0.9436 & 5.2282 & -0.1680 & 0 & 0 \\ 0 & -0.1680 & 5.0012 & -0.1782 & 0 \\ 0 & 0 & -0.1680 & 5.2282 & -0.9436 \\ 0 & 0 & 0 & -0.9436 & 7.5340 \end{bmatrix} \quad (4.3.52)$$

The transformed network is shown in Figure 4.45 and the component values are summarized in Table 4.12.
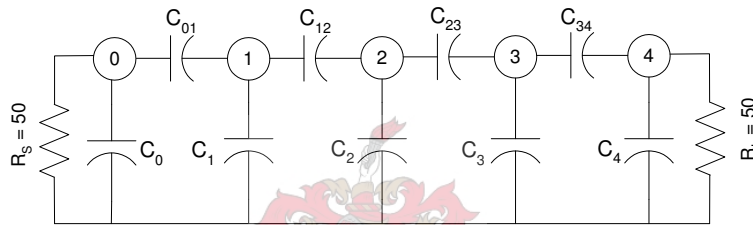


**Figure 4.45:** Prototype filter obtained by capacitance matrix transformation.

| Element Name | Element Value |
|---|---|
| $C_0$, $C_4$ | 6.5904 |
| $C_1$, $C_3$ | 4.1165 |
| $C_2$, | 4.1162 |
| $C_{01}$, $C_{34}$ | 0.9436 |
| $C_{12}$, $C_{23}$ | 0.1680 |

**Table 4.12:** Prototype filter capacitance values after transformation.

With the aid of the synthesis program FILDIM [23], the capacitance network shown in Figure 4.45 was synthesized for round conductors, and Table 4.13 summarizes the corresponding dimensions. Figure 4.46 shows the cross-sectional view of the designed combline filter.
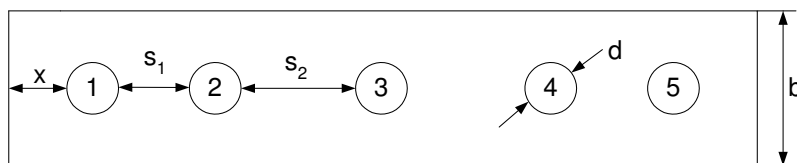


**Figure 4.46:** Cross-sectional view of the designed combline filter.

| Parameter | Value |
|---|---|
| Diameter, d | 4mm |
| Ground plane spacing, b | 11.1mm |
| Side walls to line 1 or line 5 spacing, x | 2.22mm |
| Spacing between line 1 and 2 or 4 and 5, $s_1$ | 3.7mm |
| Spacing between line 2 and 3 or 3 and 4, $s_2$ | 9.3mm |

**Table 4.13:** Physical dimensions of the combline filter.

### 4.3.3.9 Implementation and Simulation

The synthesized filter was first simulated and optimized using CST Microwave Studio [31], where all practical implementation issues were considered. The two important implementation issues considered are transitions at the ports of the filter and practical realization of the lumped capacitors.

The parasitics associated with a sudden change in geometrical size at the port influence the return loss. Thus, 50$\Omega$ conical transmission lines were included at the input and output ports to obtain a smooth transition. The characteristic impedance $Z_o$ of the conical transmission line shown in Figure 4.47 is given by eqn. (4.3.53) [32]. For $Z_o$=50$\Omega$, the value of $\Phi_o$=66.78$^o$.

$$Z_o = \frac{\eta \ln \cot \Phi_o/2}{\pi} \tag{4.3.53}$$
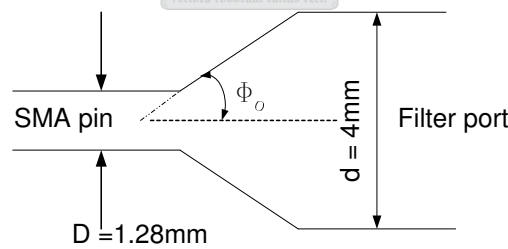


**Figure 4.47:** Conical transmission line.

The lumped capacitors were implemented using AT6926-1 microwave tuning elements obtained from TEMEX. The maximum capacitance that can be realized using this tuning arrangement, however, is limited to less than 1$p$F (which is for d=4mm and t=0.11mm). Thus, a small ridge is added at the top and bottom ground planes but towards the end of the resonators to realize the remaining 3$p$F, as the maximum lumped capacitance required is 4$p$F, after the transformation. The modified structure is illustrated in Figure 4.48.

The depth of the ridge (p) was set to 3mm so that a 0.55mm clearance exists between the resonators and the ridges. The width of the ridge (w) was tuned in CST to obtain optimum
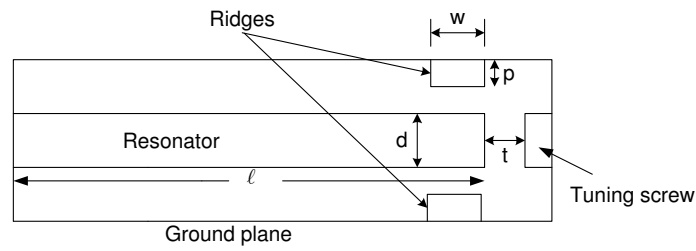
**Figure 4.48:** Lumped capacitance realization.
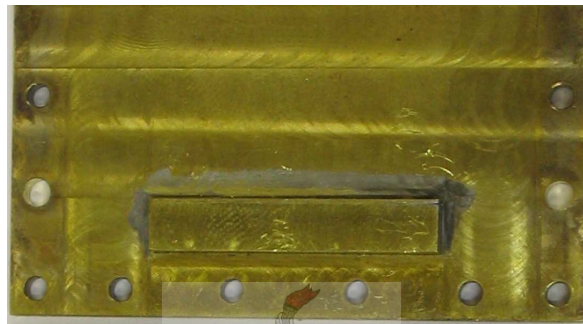


**Figure 4.49:** A photograph of the ridge added at the top and bottom ground planes.

filter response. The simulated frequency response of the filter for different ridge width (w) is plotted in Figure 4.50, where a ridge with 5.4mm width yields the desired frequency response. Figure 4.51 shows the complete layout of the designed combline filter in CST.
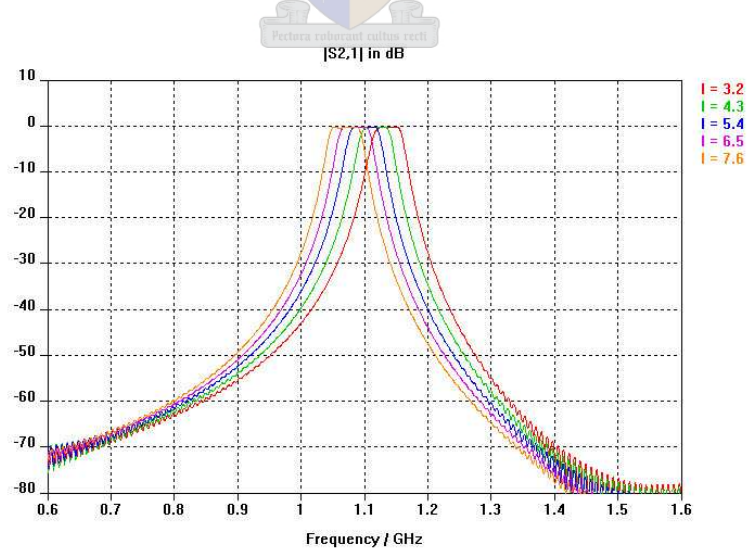


**Figure 4.50:** Simulated frequency response of the combline filter for different ridge width.
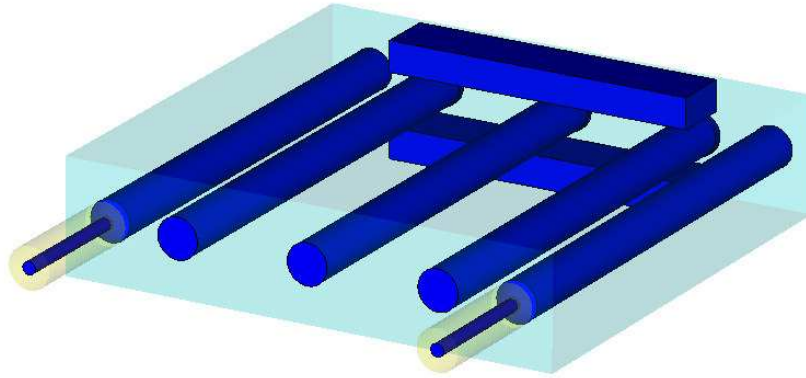
**Figure 4.51:** The layout of the designed combline filter.

#### 4.3.3.10 Measurement and Discussion

The combline filter was fabricated from brass, the same material as the tuning elements, and the resonators were cut from long cylinderical brass rods and pressure fitted into the filter box as shown in Figure 4.52.



**Figure 4.52:** A photograph of the designed combline filter.

The filter was measured on a calibrated HP8753C VNA in the frequency range of 0.5GHz to 1.7GHz. The measured results are plotted in Figure 4.53 against the results obtained from the simulation. The measured and simulated responses of the filter agree well and over the passband the measured return and insertion loss are better than 20dB and 0.9dB, respectively. However, the measured percentage bandwidth is 3.7% instead of the the designed 4%. This might be attributed to manufacturing inaccuracy.
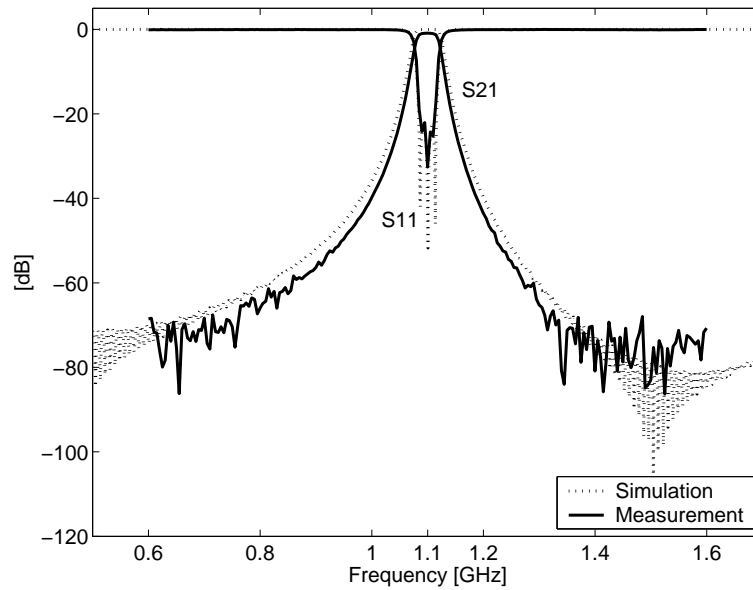
**Figure 4.53:** Measured response of the combline filter.

The tuning range of the filter was also measured and plotted in Figure 4.54. The filter has maintained better than 14dB return loss across the 337.5MHz tuning band with a maximum passband insertion loss of 1.2dB. The bandwidth remains almost the same over this tuning range.
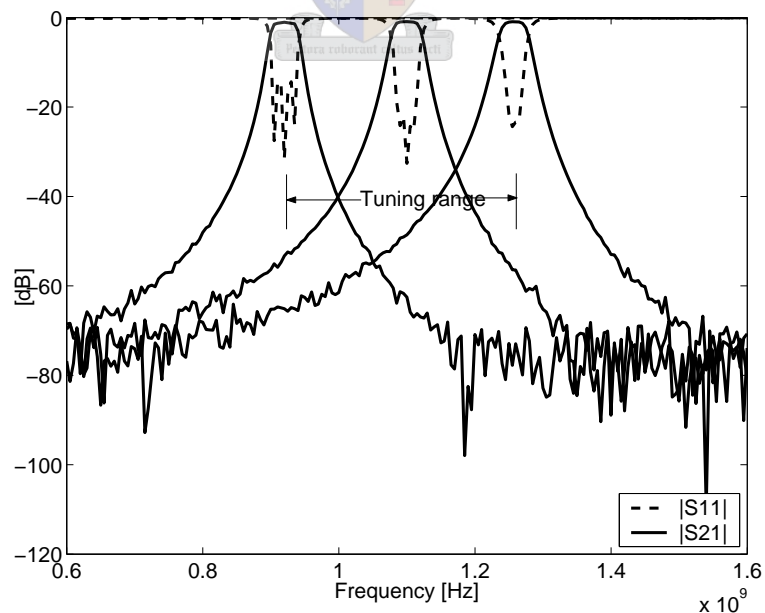


**Figure 4.54:** Measured tuning range of the combline filter.

The performance of the filter was also tested at different temperatures. The filter was heated

on a hotplate equipped with a thermostat. The setup was covered with a lid to ensure uniform heat distribution throughout the filter. Two digital thermometers with K-junction thermocouples were employed to monitor the temperature at the top and bottom parts of the filter. Measurements were made at different settings of the hotplate and each measurement was taken 30 minutes after the readings in each of the thermocouples stabilized. Figure 4.55 shows the measured response of the filter at different temperatures. The center frequency of the filter decreases as the temperature increase. The measured and calculated shift in center frequency, $\Delta F$ (eqn. (4.3.50)) are plotted in Figure 4.56 against temperature change $\Delta T$.
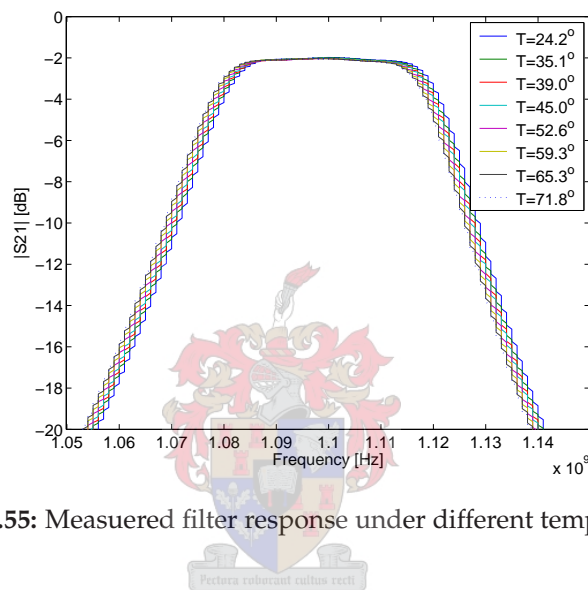


**Figure 4.55:** Measuered filter response under different temperatures.
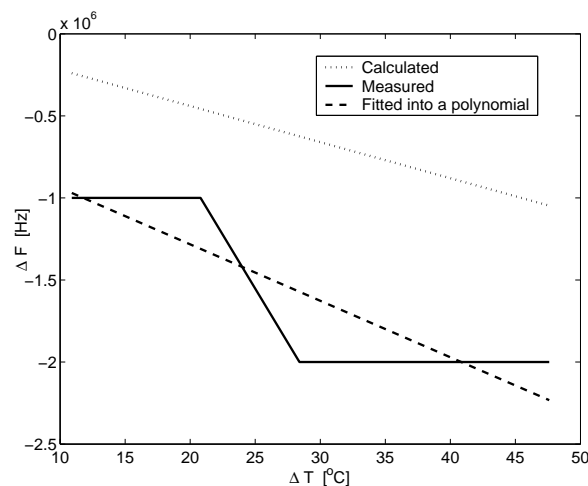


**Figure 4.56:** Shift of filter center frequency $\Delta F$ versus change in temperature $\Delta T$.

Though the best curve fit of the measured data shows a similar trend as the theoretically calculated result, there are still a few hundredths KHz difference between the calculated and the measured result. The dicrepancy is mainly attributed to the fact that the filter was

fabricated from three components (filter box, resonators and tuning elements), all obtained from different sources which might have different coefficients of thermal expansion. The other factors responsible for the discrepancy include the complexity of the ridges and measurement setup accuracy.

### 4.3.3.11   Conclusion

In this section, the design of a 1.1GHz combline filter has been presented. A bandpass prototype filter was realized first to obtain the desired frequency response. To physically realize the filter, the capacitance matrix of the prototype filter was transformed and the corresponding physical dimensions were obtained using the synthesis program called FILDIM. Even though the measured bandwidth of the filter has shrinked from the designed value, excellent frequency response has been achieved.

## 4.4   Design of Power Dividers

### 4.4.1   Introduction

In order to keep the phase coherence between the two channels of the PCM radar (the $\Sigma$ and $\Delta$-channels), corresponding mixers of the receiver must be driven from a single local oscillator (LO). Thus, for the PCM radar receiver shown in Figure 3.1, two two-way power dividers with in-phase and equal power division characteristics will be required. The design of planar Wilkinson power dividers have been done by various authors [33, 34, 35]. Kun-Hui *etal* [36] successfully modified the conventional Wilkinson power divider shown in Figure 4.57 to suppress troublesome harmonics, while keeping the basic characteristics of the conventional Wilkinson power divider. The modified Wilkinson power divider is shown in Figure 4.58. This section presents the design and implementation of two such dividers centered at 1900MHz and 1110.7MHz, and with second harmonic suppression.
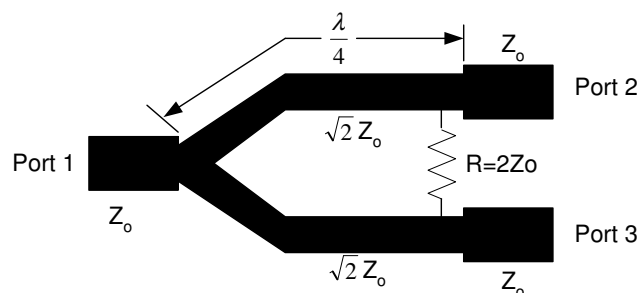


**Figure 4.57:** Conventional two-way Wilkinson power divider.

### 4.4.2  Modified Wilkinson Power Divider for Harmonic Suppression [36]

The schematic configuration of the modified Wilkinson power divider is similar to the conventional one, except the former includes two extra components. These include: two $\lambda/4n$ open-circuited stubs connected at the middle of the $\lambda/4$ branches; and a shunt inductor at the output ports. The detailed configuration of the modified Wilkinson power divider is shown in Figure 4.58. Thus, the two $\lambda/4n$ open-circuited stubs resonate at the $n^{th}$ harmonic frequency $nf_o$, and effectively short-circuit the middle of the branches to stop signal transmission at such frequency.
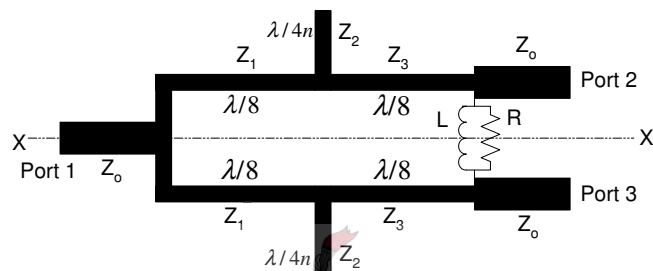


**Figure 4.58:** Modified Wilkinson power divider for $n^{th}$ harmonic suppression.

### 4.4.3  Analysis

Since the modified Wilkinson power divider (Figure **??**) is symmetrical about X-X' plane, one can use the even and odd-mode analysis to determine the circuit parameters [12]. Figures 4.59 and 4.60 show the even and odd-mode bisections of the modified Wilkinson power divider.
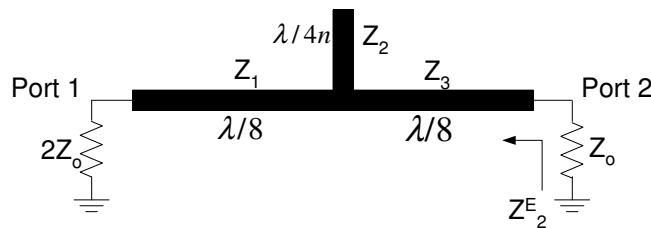


**Figure 4.59:** Bisection for even mode analysis.

The characteristic impedance of the lines are determined from the even mode bisection shown in Figure 4.59, where for $Z_1 = 2Z_o$, the even mode impedance as seen from port
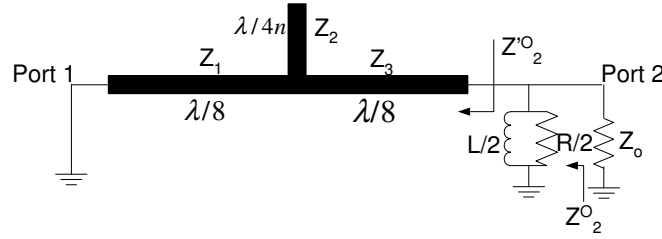
**Figure 4.60:** Bisection for odd mode analysis.

2 is given by

$$Z_2^E = Z_3 \frac{4Z_o Z_2^2 Z_3}{(Z_2 Z_3)^2 + 4Z_o^2 \left[Z_2 + Z_3 \tan(\frac{\pi}{2n})\right]^2} + j Z_3 \frac{(Z_2 Z_3)^2 - 4Z_o^2 \left[Z_2^2 - Z_3^2 \tan^2(\frac{\pi}{2n})\right]}{(Z_2 Z_3)^2 + 4Z_o^2 \left[Z_2^2 + Z_3^2 \tan(\frac{\pi}{2n})\right]^2} \quad (4.4.1)$$

Since all ports are matched to $Z_o$ the imaginary part of eqn. (4.4.1) must be zero, which results in

$$(Z_2 Z_3)^2 - 4Z_o^2 \left[Z_2^2 - Z_3^2 \tan^2(\frac{\pi}{2n})\right] = 0 \quad (4.4.2)$$

Solving eqn. (4.4.2) yields

$$Z_2 = \frac{2Z_o \sqrt{1 - t^2 \tan^2(\frac{\pi}{2n})}}{t} \quad (4.4.3)$$

$$Z_3 = 2Z_o \sqrt{1 - t^2 \tan^2(\frac{\pi}{2n})} \quad (4.4.4)$$

where $t = Z_3/Z_2$.

Substitution of eqn. (4.4.3) and eqn. (4.4.4) into the real part of eqn. (4.4.1) and applying port matching condition $Z_2^E = Z_o$ results in

$$2t^2 \tan^2(\frac{\pi}{2n}) + t \tan(\frac{\pi}{2n}) - 1 = 0 \quad (4.4.5)$$

Since $t > 0$ and $0 < \pi/2n < \pi/2$, the valid solution of eqn. (4.4.5) is

$$t \tan(\frac{\pi}{2n}) = 1/2 \quad (4.4.6)$$

Substituting eqn. (4.4.6) into eqn. (4.4.3) and eqn. (4.4.4) yields

$$Z_2 = 2\sqrt{3} \tan(\frac{\pi}{2n}) Z_o \quad (4.4.7)$$

$$Z_3 = \sqrt{3} Z_o \quad (4.4.8)$$

With the characteristic impedance of the lines obtained as above, the even mode input impedance as seen from port 1 of Figure 4.59 is given by

$$Z_1^E = \frac{Z_2}{j\tan(\frac{\pi}{2n})} || Z_3 \frac{Z_o + jZ_3}{Z_3 + jZ_o} = 2Z_o \qquad (4.4.9)$$

where the symbol $||$ represents a parallel connection. Thus, the impedance looking from port 1 of the complete circuit shown in Figure **??** is $Z_o$, which is independent of n.

The shunt elements of the modified Wilkinson power divider are determined from the odd mode analysis shown in Figure 4.60, where the impedance looking from port 2 is given by

$$Z_2^O = \left( \frac{1}{Z_2^{'O}} + \frac{2}{R} - j\frac{2}{\omega L} \right)^{-1} \qquad (4.4.10)$$

where,

$$Z_2^{'O} = jZ_3 \frac{(Z_1 + Z_3)Z_2 - Z_1 Z_3 \tan(\frac{\pi}{2n})}{(Z_1 - Z_3)Z_2 - Z_1 Z_3 \tan(\frac{\pi}{2n})} = -j(2 + \sqrt{3})Z_o \qquad (4.4.11)$$

For a perfectly matched port $Z_2^O = Z_o$. Thus, the resistance R and inductance L are respectively obtained from the real and imaginary parts of eqn. (4.4.10).

$$R = 2Z_o \qquad (4.4.12)$$

and

$$L = \frac{2\left(2 + \sqrt{3}\right)Z_o}{\omega} \qquad (4.4.13)$$

where $\omega = 2\pi f_o$. The resistance R given in eqn. (4.4.12) is the same as the one for the conventional Wilkinson power divider.

### 4.4.4  Design and Implementation

For $Z_o = 50\Omega$ and second harmonic suppression modified Wilkinson power dividers, the values of the characteristic impedance of the lines and shunt elements calculated using the above equations are listed in Table 4.14.

| $f_o$ (MHz) | 1110.7 | 1900 |
|---|---|---|
| $Z_1$ ($\Omega$) | 100 | 100 |
| $Z_2$ ($\Omega$) | 173.2 | 173.2 |
| $Z_3$ ($\Omega$) | 86.6 | 86.6 |
| R ($\Omega$) | 100 | 100 |
| L (nH) | 53.48 | 31.26 |

**Table 4.14:** Cicruit parameters for 50$\Omega$ and second harmonic suppression modified Wilkinson power dividers.

The two power dividers are fabricated on a 1.581mm-thick TLX-9 substrate from Taconic, which has a relative permitivity of 2.5. Lower values of inductors, 39nH instead of 53.48nH and 27nH instead of 31.26nH, are used in accordance to the respective values of the inductors at high frequency. The data sheet of the inductors used is available appendix C.

The power dividers were simulated and optimised in Microwave Office (MWO). Figures 4.61 and 4.62 show the layouts of the 1110.7MHz and 1900MHz power dividers generated using MWO. The dimensions were calculated using TXLINE. Besides, short tapered transmission lines were added wherever a change in width encountered. This will reduce the parasitic effects associated with sudden change in width.
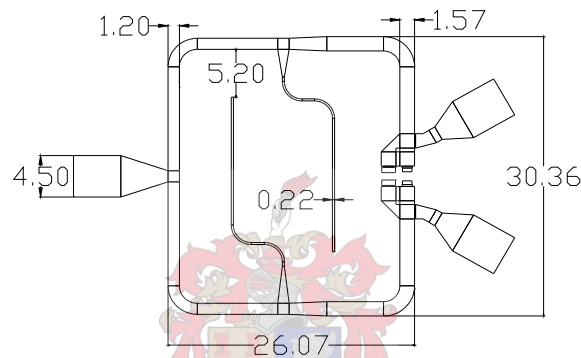


**Figure 4.61:** Layout of the 1110.7MHz modified Wilkinson power divider. Dimensions in mm.
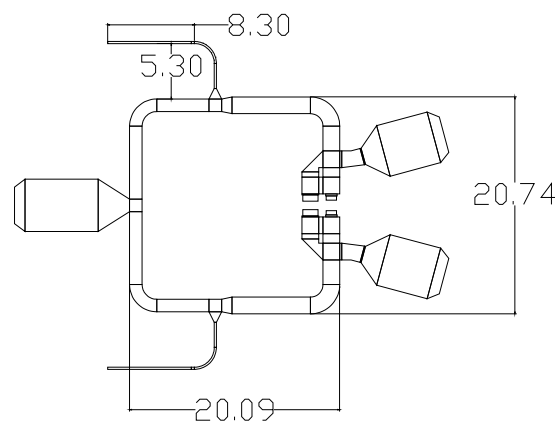


**Figure 4.62:** Layout of the 1900MHz modified Wilkinson power divider. Dimensions in mm.

### 4.4.5 Measurements and Discussion

The experimental results of the 1110.7MHz modified Wilkinson power divider are plotted in Figure 4.63 and Figure 4.64 against simulation results. The measured results agree quite

well with the simulation, except a small shift in centre frequency. This might have been caused due to manufacturing errors.
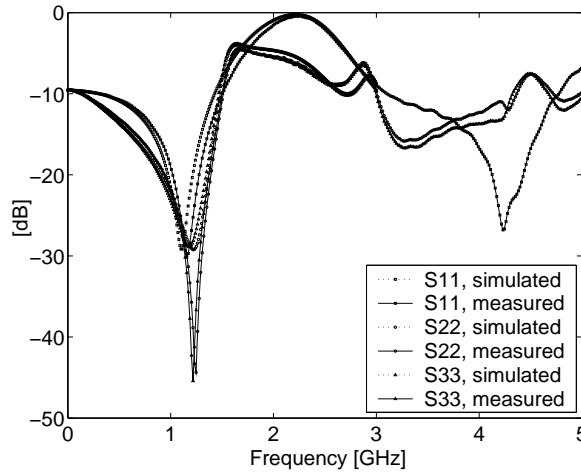


**Figure 4.63:** Simulated and measured return loss of the 1110.7MHz power divider.
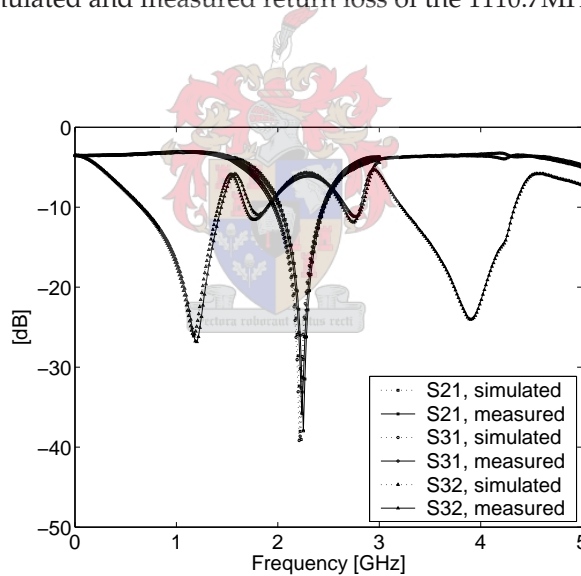


**Figure 4.64:** Simulated and measured insertion loss and isolation of the 1110.7MHz power divider.

At all ports the measured reflection coefficients are better than -26dB and the power split between the output ports is -3.15dB at the centre frequency, 1110.7MHz but the second harmonic, 2221.4MHz is attenuated by 30dB. The measurement also shows an isolation of 22dB between the output ports.

The simulated and measured phase angles of the transmission parameters, S21 and S31 are plotted in Figure 4.65. The measured results show a very small, $0.172^o$ phase unbalance between the outputs.
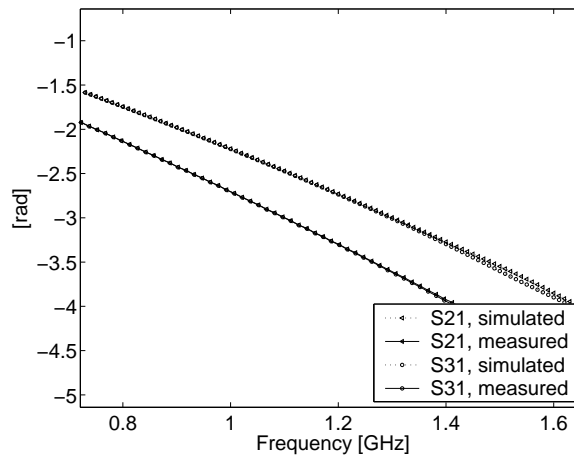
**Figure 4.65:** Simulated and measured transmission angle versus frequency of the 1900MHz modified Wilkinson power divider.

The experimental S-parameters of the 1900MHz modified Wilkinson power divider are plotted in Figure 4.66 and Figure 4.67 against simulation results. The measured results have shifted in frequency, but agree quite well with the simulation.
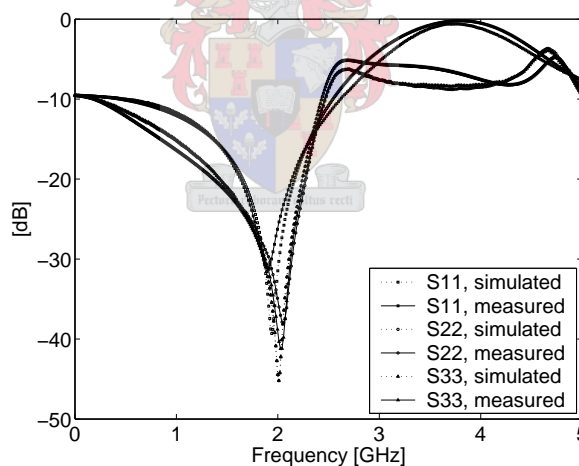


**Figure 4.66:** Simulated and measured return losses versus frequency of the 1900MHz modified Wilkinson power divider.

Measured reflection coefficients at all ports are better than -29dB while the power split between the output ports is -3.15dB at the centre frequency of 1900MHz. The 3800MHz second harmonic is attenuated by 28dB and isolation between the output ports is 31dB.

The experimental results also show a very small ($0.687^o$) phase unbalance between the phase angles of the transmission parameters, S21 and S31 as shown in Fig. 4.68.
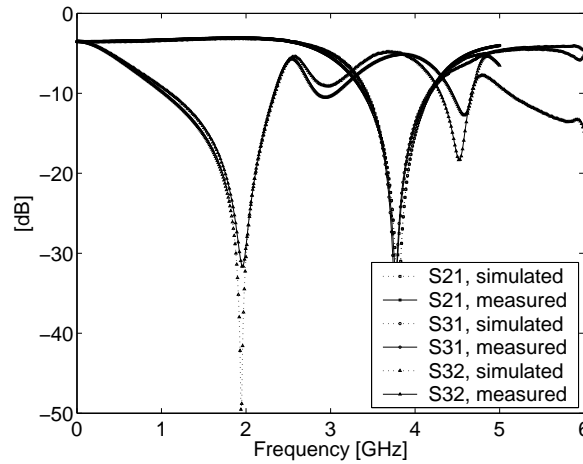
**Figure 4.67:** Simulated and measured insertion losses and isolation versus frequency of the 1900MHz modified Wilkinson power divider.
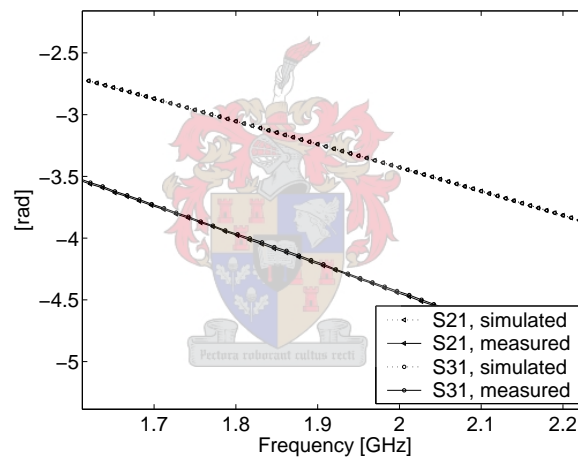


**Figure 4.68:** Simulated and measured transmission angle versus frequency of the 1900MHz modified Wilkinson power divider.

### 4.4.6 Conclusion

In this section, two Wilkinson power dividers of 1110.7MHz and 1900MHz centre frequency and with second harmonic suppression have been designed based on the work of Kun-Hui *etal* [36]. The only limitation in the construction was the physical dimensions of the lines. Low loss thicker substrates were used in order to realize the thinnest tracks ($Z_2 = 173.2\Omega$). The measured S-parameters of the dividers agree very well with the MWO simulated results. The manufactured power dividers are shown in Figures 4.69 and 4.70.
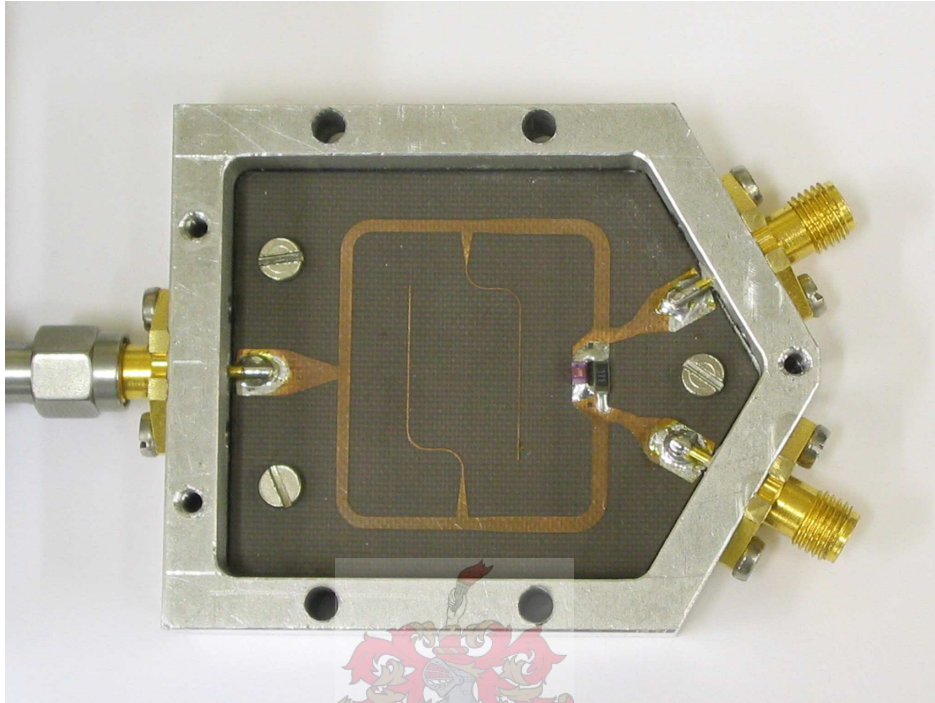
**Figure 4.69:** A photograph of the 1110.7MHz modified Wilkinson power divider.
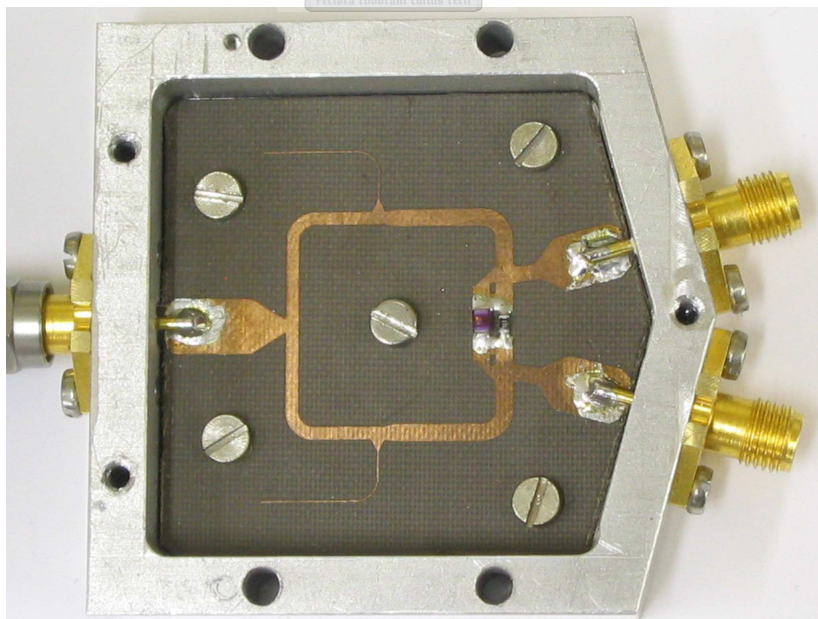


**Figure 4.70:** A photograph of the 1900MGHz modified Wilkinson power divider.

# Chapter 5

# Design and Evaluation of Active Sub-Systems

## 5.1 Introduction

The sum ($\Sigma$) and difference ($\Delta$) signals at the output of the $0^o/180^o$ microwave hybrid are amplified and downconverted using a cascade of active sub-systems, which include amplifiers and mixers. As it is mentioned in chapters 2 and 3, accurate performance of these sub-systems is important to the overall operation and accuracy of the PCM radar. This chapter presents the measurements performed on six RF amplifiers and four double-balanced mixers used in designing the PCM radar receiver. Section 5.2 describes the design of two local oscillators (LOs) required to drive the LO ports of the mixers, while sections 5.3 and 5.4 present the measurements performed on the RF amplifiers and mixers, respectively.

## 5.2 Design of Local Oscillators

Several types of frequency synthesizers can be used to implement a stable and low phase noise LO for receivers. The digital (look-up-table), analogue (direct) and phase-locked (indirect) frequency synthesizers are but few among the most commonly designed types [7]. The latter type enjoys the qualities of a clean and highly stable reference oscillator and can be implemented easily. Thus, it is used to implement the LOs required for the PCM radar receiver.

### 5.2.1 Phase-Locked Frequency Synthesizer

The basic block diagram of a phase-locked frequency synthesizer is shown in Figure 5.1. It is basically a conventional phase-locked loop (PLL) [37], with a dc reference voltage $V_{DC}$ added to the loop-driven control voltage $V_L$. The phase-frequency detector (PFD) compares a divided-down version of the output signal with that of the reference oscillator and out-

puts an up or down signal to a charge pump (CP), which in turn drives/draws current pulses to/from the loop filter (LF) depending on the output of the PFD. The LF smoothes the current pulses into loop-driven control voltage $V_L$, which changes the output of the voltage controlled oscillator (VCO) in a direction to drive the CP's average output towards zero. When the average output of the CP is zero, the synthesizer is said to be in phase lock or locked, and the output frequency $f_{OUT}$ is given as

$$f_{OUT} = \frac{N}{R} f_{REF} \tag{5.2.1}$$

where $f_{REF}$ is the frequency of the reference oscillator; R and N are the reference and feedback counters used to scale the frequencies.
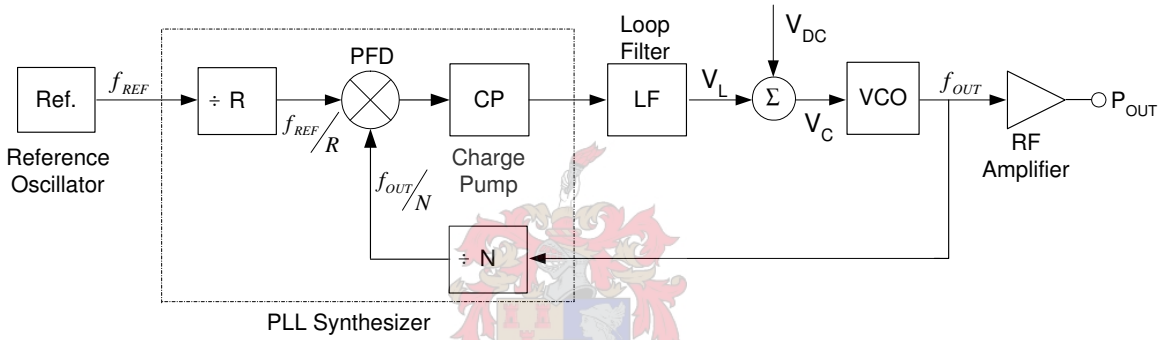


**Figure 5.1:** Block diagram of a phase-locked frequency synthesizer.

The PFD, charge pump (CP), reference counter (R) and feedback counter (N) usually come in a single integrated circuit (IC), called a PLL synthesizer. The external RF amplifier boosts the strength of the output signal to the desired level, and it also buffers the synthesizer circuit from external load variations.

The key performance parameters of a phase-locked frequency synthesizer include the phase noise, reference spurs and lock time [38].

- **Phase noise (PN)** refers to the purity of the synthesizer output signal at a given offset frequency $\Delta f$. It is rougly given by [38]:

$$PN = PN_{SYNTH} + 20 \log N + 10 \log f_{PFD} \tag{5.2.2}$$

where, $PN_{SYNTH}$ is the phase noise contribution of the PLL synthesizer in dB, $20 \log N$ is additional noise due to the feedback counter (N) and $10 \log f_{PFD}$ is the noise contribution due to the synthesizer PFD frequency $f_{PFD}$, where $f_{PFD} = f_{REF}/R$. Thus, the highest feasible PFD frequency $f_{PFD}$ should be used to ensure better phase noise performance.

- **Reference spurs** occur at multiples of the synthesizer PFD frequency $f_{PFD}$, and depend on the internal leakage of the PLL synthesizer and VCO sensitivity. In a receiver, they could get mixed down on the top of the wanted signal and reduce the sensitivity of the receiver. Thus, they must be suppressed using a very narrow loop bandwidth, which will slow the lock time.

- **Lock time** refers to the time required to switch the output from one frequency to another, and depends on the loop bandwidth and PFD frequency. It is however not considered in fixed frequency designs.

### 5.2.2 Mathematical Description of a Phase-Locked Frequency Synthesizer [7]

Figure 5.2 shows a simplified Laplace representation of the phase-locked frequency synthesizer. For simplicity, phase variables are used instead of frequency. Simple analysis yields the output of the VCO as

$$\theta_{OUT}(s) = \frac{K_o}{s} V_c(s) \tag{5.2.3}$$

where, $K_o$ is VCO sensitivity in MHz/volt and $V_c(s)$ is the control voltage given by

$$V_c(s) = K_p F(s)\theta_e(s) + V_{dc}(s) \tag{5.2.4}$$

where, $K_p$ is a constant that depends on PFD and CP, F(s) is the transfer function of the loop filter, and $\theta_e(s)$ is the loop phase error given by

$$\theta_e(s) = \theta_{REF}(s) - \frac{\theta_{OUT}(s)}{N} \tag{5.2.5}$$
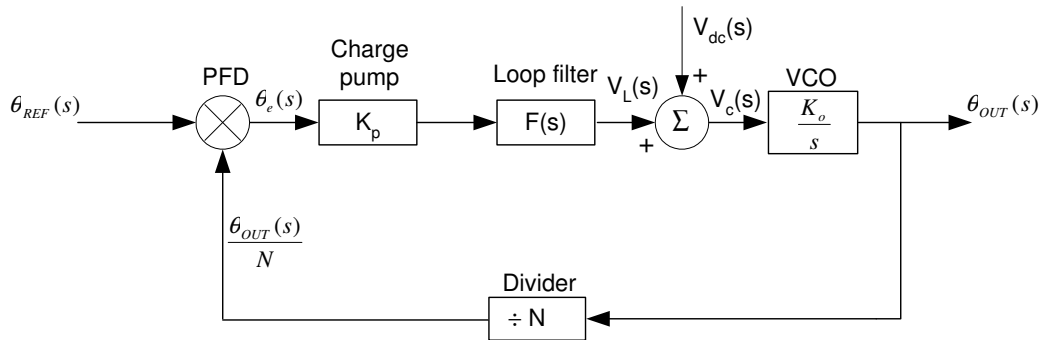


**Figure 5.2:** The phase-locked frequency synthesizer in Laplace representation.

Substituting eqn. (5.2.5) into eqn. (5.2.4) yields

$$V_c(s) = K_p F(s) \left( \theta_{REF}(s) - \frac{\theta_o(s)}{N} \right) + V_{dc}(s) \tag{5.2.6}$$

Using the new expression for $V_c$ in eqn. (5.2.3) yields

$$\theta_{OUT}(s) = \frac{K_p K_o F(s)}{s + K_p K_o F(s)/N}\theta_{REF}(s) + \frac{K_o}{s + K_p K_o F(s)/N}V_{dc}(s) \tag{5.2.7}$$

Thus, the closed-loop transfer function from $\theta_{REF}$ to $\theta_{OUT}$ is given by

$$\frac{\theta_{OUT}(s)}{\theta_{REF}(s)} = \frac{K_p K_o F(s)}{s + K_p K_o F(s)/N} \tag{5.2.8}$$

If no loop filter is used (F(s) = 1) eqn. (5.2.8) becomes

$$\frac{\theta_{OUT}(s)}{\theta_{REF}(s)} = N\frac{\omega_c}{s + \omega_c} \tag{5.2.9}$$

where $\omega_c = K_p K_o/N$ is called the loop bandwidth.
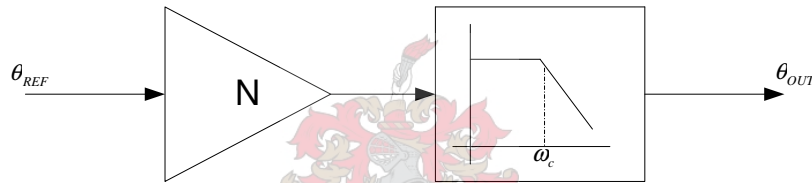


**Figure 5.3:** Simplified equivalent model of a phase-locked frequency synthesizer with F(s)=1.

Eqn. (5.2.9) is equivalent to the transfer function of a simple lowpass filter with gain $N$ and bandwidth equal to $\omega_c$, as shown in Figure 5.3. The frequency of the signal entering at $\theta_{REF}$ is amplified by a factor N and transferred to $\theta_{OUT}$ with little attenuation for frequencies below the loop bandwidth.

## 5.2.3 Design and Implemetation

### 5.2.3.1 Specifications

The specifications of the local oscillators (LOs) required for the PCM radar receiver are summarized Table 5.1.

|  | LO1 | LO2 |
|---|---|---|
| Frequency [GHz] | 1.9 | 1.1107 |
| Output power [dBm] | 13.5 | 13.5 |

**Table 5.1:** The specifications of the LOs required for the PCM radar receiver.

The complete design of a phase-locked frequency synthesizer includes: the design of a stable reference oscillator, selection and programming of the PLL synthesizer, selection of a suitable voltage controlled oscillator (VCO), and the design of a loop filter (LF).

### 5.2.3.2    Design of Stable Reference Oscillator

The stability of a phase-locked frequency synthesizer depends on the qualities of the reference frequency [39]. Thus, a highly stable reference source is required. A crystal resonator-controlled Collpits oscillator shown in Figure 5.4 generates the required reference frequency of 15MHz.
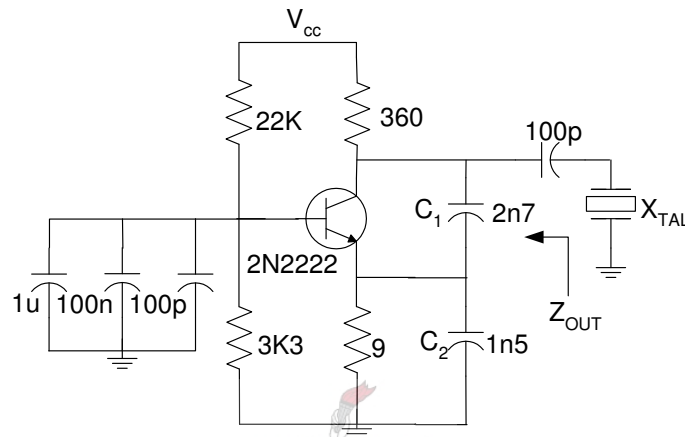


**Figure 5.4:** Crystal resonator-controlled Collpits oscillator.

The feedback capacitors, $C_1$ and $C_2$, of the Collpits oscillator were chosen to achieve maximum negative output resistance and thereby ensure oscillation at the desired reference frequency. Figure 5.5 plots the output impedance $Z_{OUT}$ as a function of $C_1$ and $C_2$.
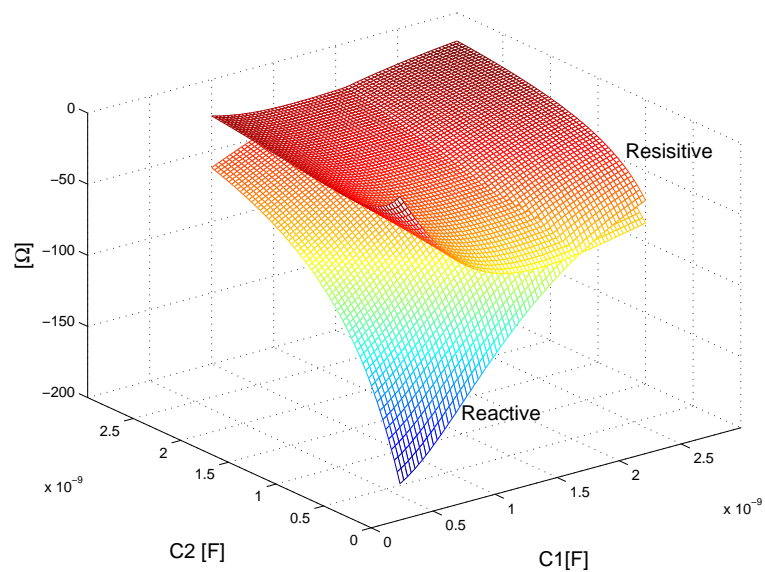


**Figure 5.5:** The output impedance $Z_{OUT}$ of the crystal-controlled Collpits oscillator as a function of $C_1$ and $C_2$.

In the final design, an amplifier and a lowpass filter were added to the Collpits oscillator in order to boost the strength of the reference signal and reduce broadband noise and harmonics entering the synthesizer, respectively.

The measured frequency response of the designed reference oscillator is shown in Figure 5.6. At the designed reference frequency of 15MHz, the power level is read as 2.9dBm and this is big enough to drive two PLL synthesizers.
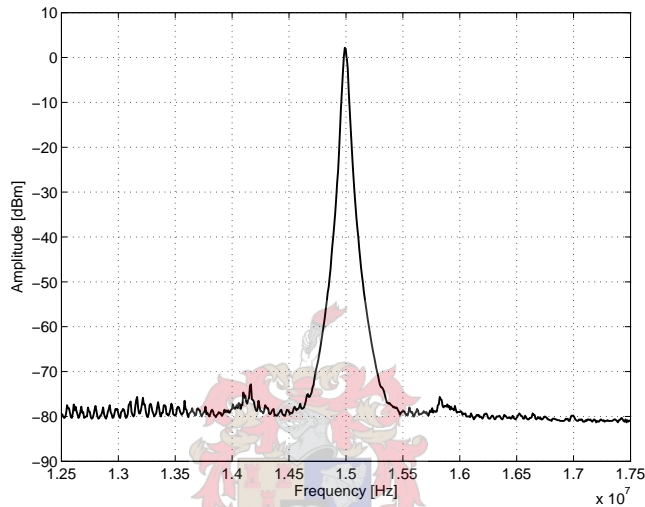


**Figure 5.6:** Measured response of the reference oscillator.

### 5.2.3.3 Selection and Programming of PLL Synthesizer

The ADF4153 PLL synthesizer from Analog Devices was selected for both LO designs as it is specified to operate up to 4GHz and allow fractional-N division with fast lock time and improved phase noise performance [40]. A simplified system architecture used by the ADF4153 PLL synthesizer is shown in Figure 5.7, where the reference and feedback counters are programmed serially using CLK, DATA and LE input pins, and an 24-bit data register. The integer (INT), fraction (FRAC) and modulus (MOD) registers define the overall feedback counter (N=INT+(FRAC/MOD)). In addition, the 4-bit reference counter (R) allows selectable frequencies at the PFD input. Table 5.2 summarizes the reference and feedback counters programmed into the PLL synthesizers.

|  | $f_{REF}$ [MHz] | R-counter | INT | FRAC | MOD | N-counter | $f_{OUT}$ [GHz] |
|---|---|---|---|---|---|---|---|
| LO1 | 15 | 1 | 126 | 2 | 3 | 380/3 | 1.9 |
| LO2 | 15 | 1 | 74 | 7 | 150 | 11107/150 | 1.1107 |

**Table 5.2:** The calculation of reference and feedback counters.
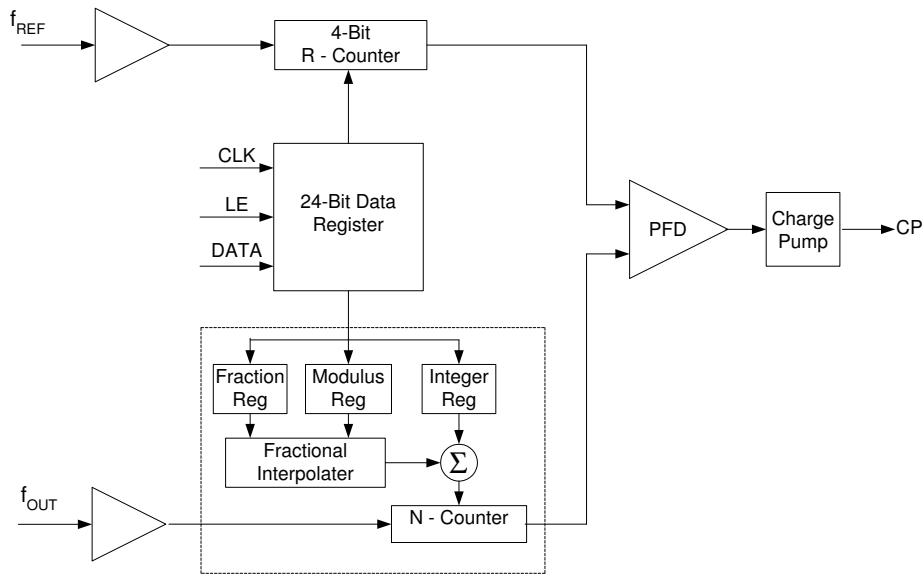
**Figure 5.7:** A simplified system architecture used by ADF4153 PLL synthesizer.

The PLL synthesizers were programmed using an ATmega32 microcontroller. The complete programming code, written in C++ programming language, is available in appendix D.

### 5.2.3.4   Selection of a Suitable VCO

The phase noise further away from the fundamental signal of a phase-locked frequency synthesizer is dominated by the VCO [41]. Thus, a VCO with good phase noise and harmonic suppression must be used. The ROS-2150VW VCO from Mini-Circuits was selected as it covers the required LO frequencies and delivers optimum output power. The features of the VCO, as specified in the datasheet [42], are summarized in Table 5.3.

| Frequency band [MHz] | Tuning sensitivity[Mz/volt] | Output power [dBm] | Phase noise at 1MHz [dBC/Hz] | $2^{nd}$ harmonic suppression [dBc] |
|---|---|---|---|---|
| 970-2150 | 30-70 | 4 | -138 | -15 |

**Table 5.3:** The specifications for the ROS-2150VW VCO.

### 5.2.3.5   Design of Loop Filter

The final step in the design of phase-locked frequency synthesizer is the loop filter (LF). The standard and most commonly used loop filter is shown in Figure 5.8. The element values of the loop filters, calculated with the aid of ADIsimPLL program [43], are summarized in Table 5.4. Nearest available values were used in the final design, which is shown in Figure 5.10.

Various other sub-systems were designed to complete the synthesizers. These include summing networks, DC references, high frequency resistive power dividers, 3dB attenuators

and RF amplifiers. Figure 5.10 shows the complete schematic of the designed LOs.
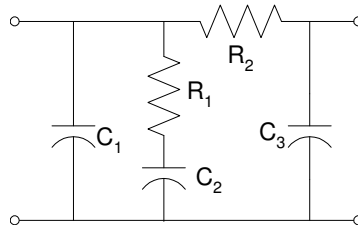


**Figure 5.8:** Third order lowpass filter.

| Element | LO1 | LO2 |
|---------|---------|---------|
| $C_1$ | 83.6nF | 50.1nF |
| $R_1$ | 33.2 $\Omega$ | 32.3$\Omega$ |
| $C_2$ | 1.14uF | 681nF |
| $R_2$ | 67.8$\Omega$ | 22.8$\Omega$ |
| $C_3$ | 38.1nF | 22.8nF |

**Table 5.4:** The element values of the loop filters calculated using ADIsimPLL.

Figure 5.9 shows the a photograph of the designed LOs, where the high and low frequency sections are implemented separately to avoid undesired couplings. The high frequency section as shown in Figure 5.11 includes the VCO, resistive divider, 3dB attenuator and RF amplifier; whereas the low frequency section as shown in Figure 5.12 includes the PLL synthesizer, loop filter, DC reference and summing network.



**Figure 5.9:** A photograph of the designed local oscillators.
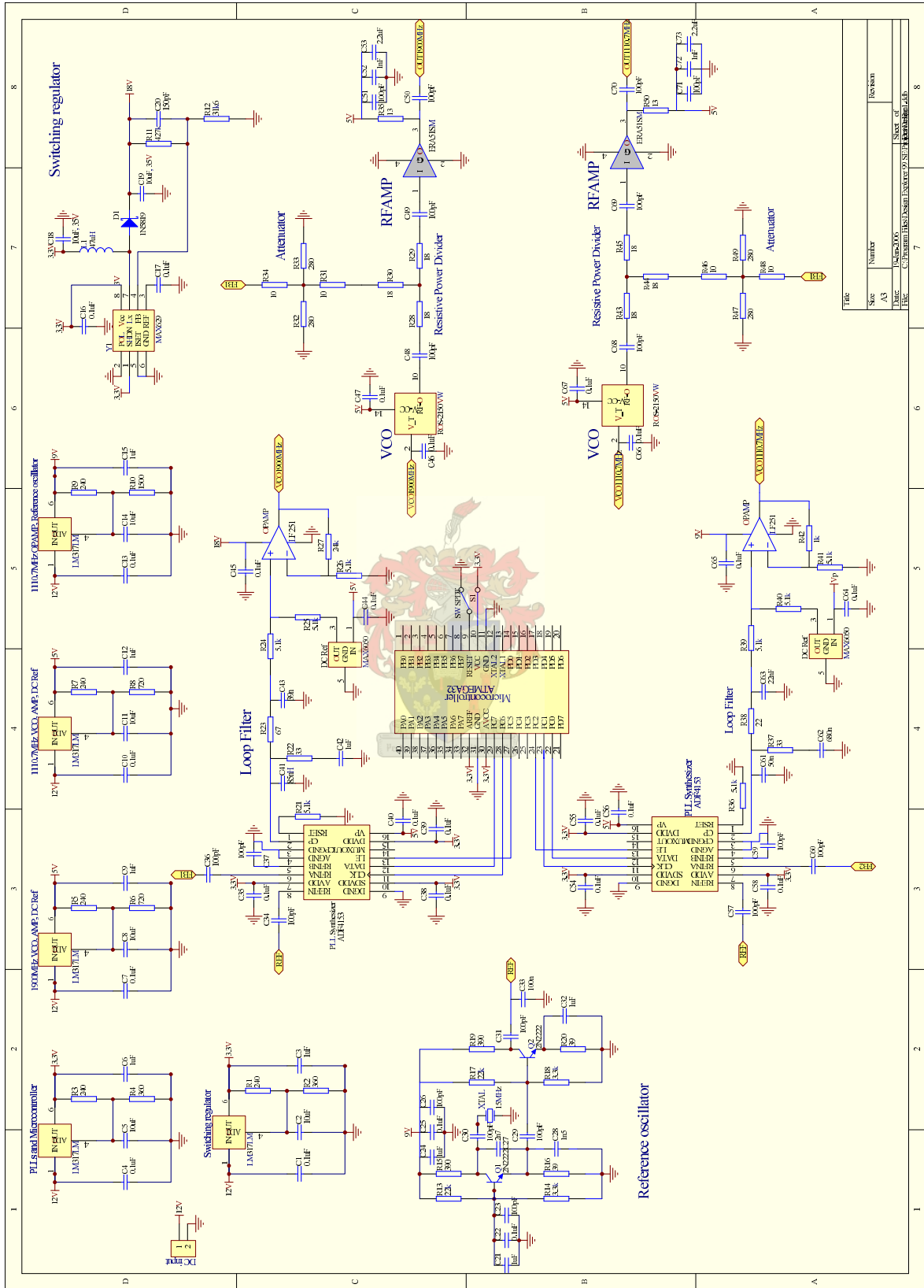
**Figure 5.10:** Complete schematic diagram of the designed LOs.
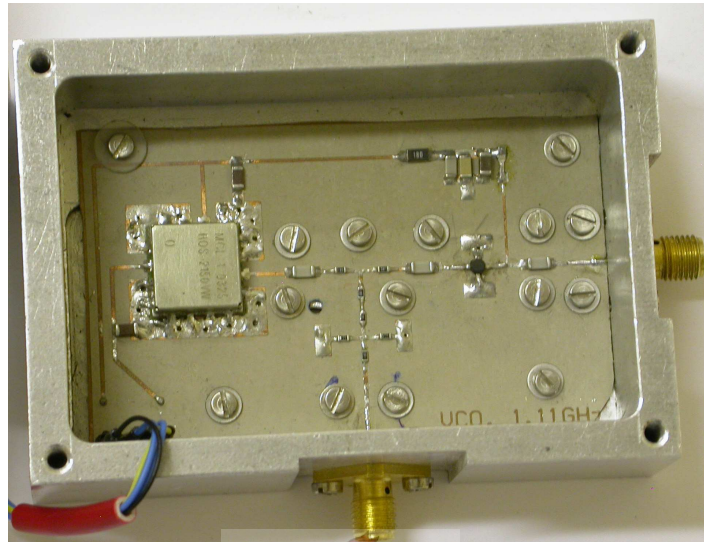
**Figure 5.11:** High frequency section of the designed LOs.
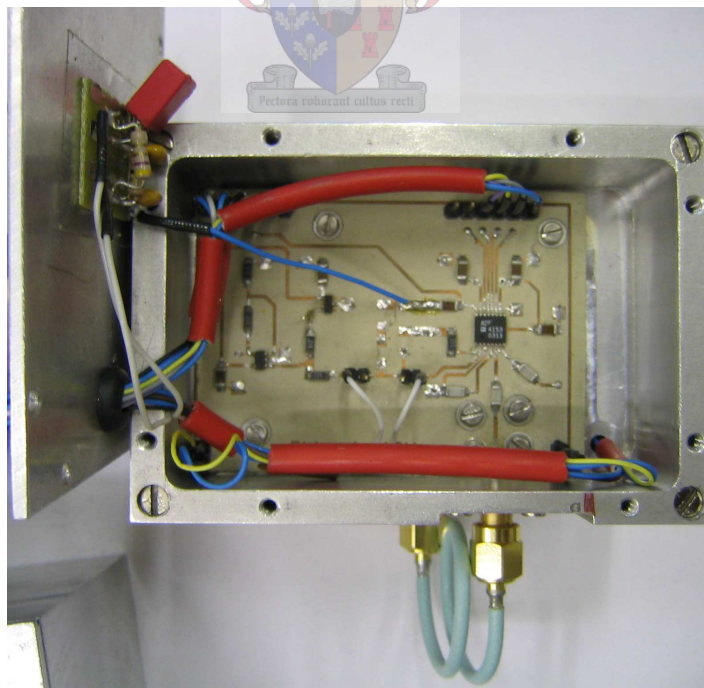


**Figure 5.12:** Low frequency section of the designed LOs.

### 5.2.4 Measurements and Discussions

The designed LOs were measured using the FSK30 spectrum analyzer and the results are presented in this section.

#### 5.2.4.1 Output Power

Figures 5.13 and 5.14 show the fundamental output response of the 1.9GHz and 1.1107GHz LOs, respectively. The output powers at the respective fundamental frequencies can be read as 11.12dBm and 12.87dBm, which are 2.38dB and 0.63dB below the desired LO levels. These drops could be attributed to the variations of the VCO output power with frequency and power loss in the measurement cables.
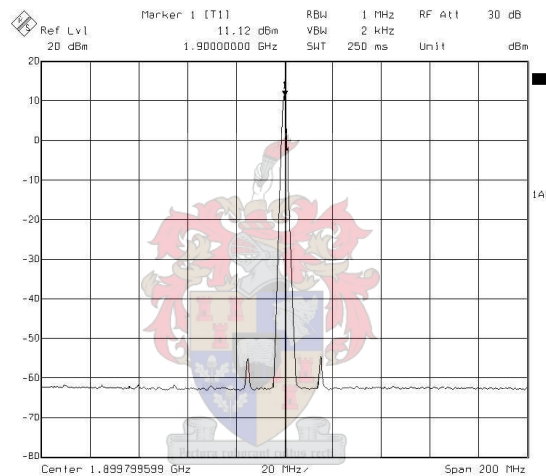


**Figure 5.13:** Fundamental output response of the 1.9GHz LO.
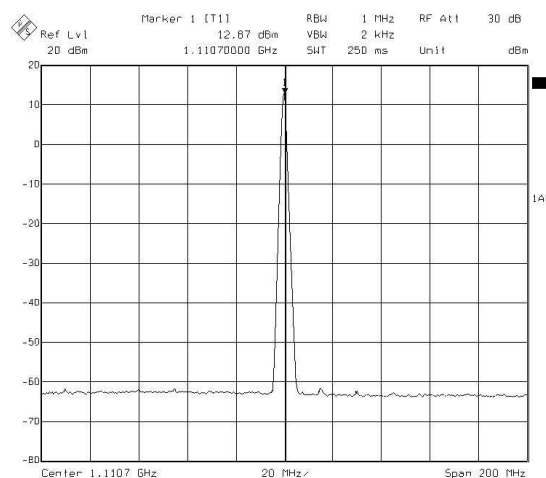


**Figure 5.14:** Fundamental output response of the 1.1107GHz LO.

The reference spurs at $\pm15$ MHz are suppressed by 66dB and 74.5dB respectively for the 1.9GHz and 1.1107GHz LOs. The improvement in the latter case could be attributed to low loop bandwidth. The loop bandwidths calculated using ADIsimPLL program are 20.3KHz and 11.8KHz respectively for the 1.9GHz and 1.1107GHz LOs.

### 5.2.4.2 Harmonic Suppression

Figure 5.15 and 5.16 show the spectrum of the 1.9GHz and 1.1107GHz LOs, respectively up to $3^{rd}$ harmonics. The $2^{nd}$ harmonics [marker 3] are suppressed by 32.19dB and 17.91dB below the fundamentals of the 1.9GHz and 1.1107GHz LOs, respectively; whereas the $3^{rd}$ harmonics [marker 4] are suppressed by 34dB and 41.42dB.
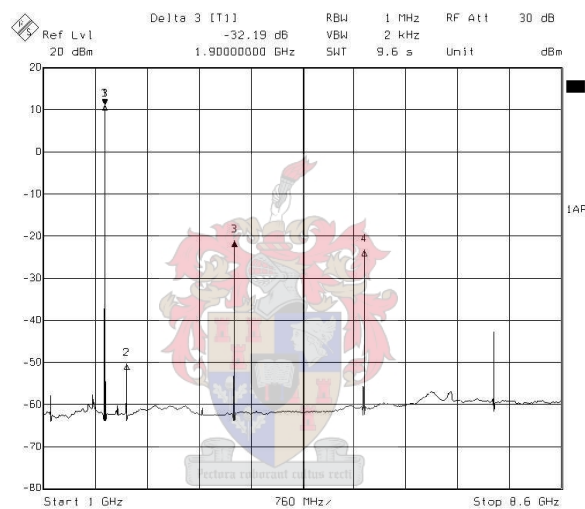


**Figure 5.15:** Harmonics of the 1.9GHz LO.
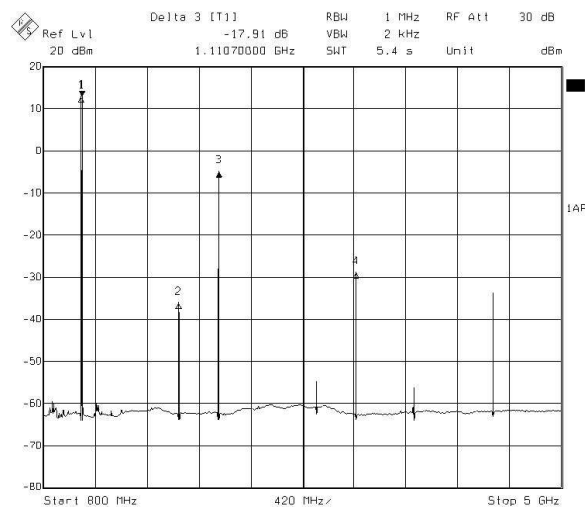


**Figure 5.16:** Harmonics of the 1.1107GHz LO.

Beside the harmonics, the $2^{nd}$ harmonic of the 1.1107GHz LO [marker 2 of Figure 5.15] and the fundamental frequency of the 1.9GHz LO [marker 2 of Figure 5.16] appear at the outputs of the 1.9GHz and 1.1107GHz, respectively. This could be attributed to the common mode currents induced in the wiring.

### 5.2.4.3   Phase Noise

Figures 5.17 and 5.18 show the measured single side band (SSB) phase noises of the 1.9GHz and 1.1107GHz LOs, respectively. At 1MHz offset frequency, the SSB phase noises of the 1.9GHz and 1.1107GHz LOs are respectively read as -132.13dBc/Hz and -134.53dBc/Hz. These values are respectively 6dB and 3dB worse compared to the specified phase noise of the ROS-2150VW VCO [42].
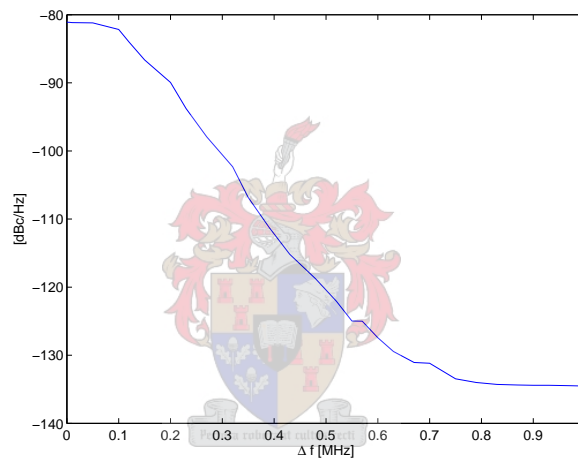


**Figure 5.17:** Measured SSB phase noise of the 1.9GHz LO.
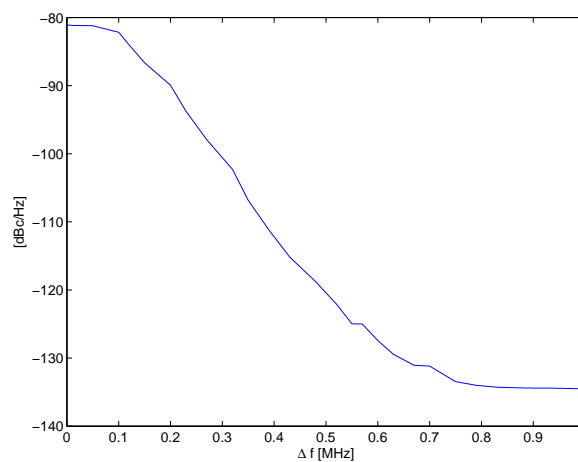


**Figure 5.18:** Measured SSB phase noise of the 1.1107GHz LO.

### 5.2.4.4   Conclusion

In this section, two local oscillators (LOs) at frequency of 1.9GHz and 1.1107GHz were designed and implemented using phase-locked frequency synthesizers. The measurements showed that the LOs performed very well and agree with their respective specifications, except the output power of the 1.9GHz LO which is 2.3dB below the required level. This, however, will not be a concern as it is still sufficient enough to drive the mixers of the PCM radar receiver. Besides, both LOs operate from a single power supply of 12V and draw a total current of 165mA.

## 5.3   Amplifiers Measurement

### 5.3.1   RF Amplifiers

Two HMC476MP86 amplifiers from Hittite are used at the RF sections of sum ($\Sigma$) and difference ($\Delta$) channels of the PCM radar receiver. The properties of the amplfiers, as obtained from the datasheet [44], are summarized in Table 5.5.

| Min. Gain [dB] | Noise Figure [dB] | Min. Output 1 dB pt. [dBm] | Input Return loss [dB] | Output Return loss [dB] |
|---|---|---|---|---|
| 13.5 | 2.5 | 9.0 | 15 | 20 |

**Table 5.5:** Properties of the HMC476MP86.

Figure 5.19 shows the physical implementation of the amplifiers with biasing circuit and DC blocking capacitors.
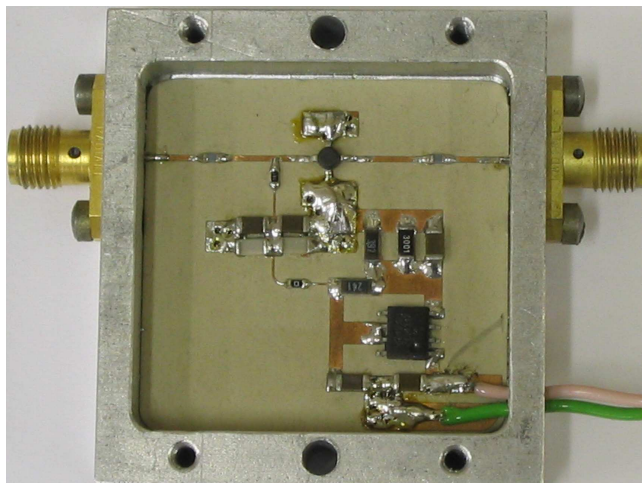


**Figure 5.19:** Physical implementation of the amplifiers.

Figure 5.20(a) shows the measurement setup used to measure the S-parameters of the amplifiers. For accurate measurement, the HP8753 VNA was first calibrated using the short-open-

load-through (SOLT) calibration technique. Figure 5.21 shows the measured S-parameters of the HMC476MP86 amplifiers.
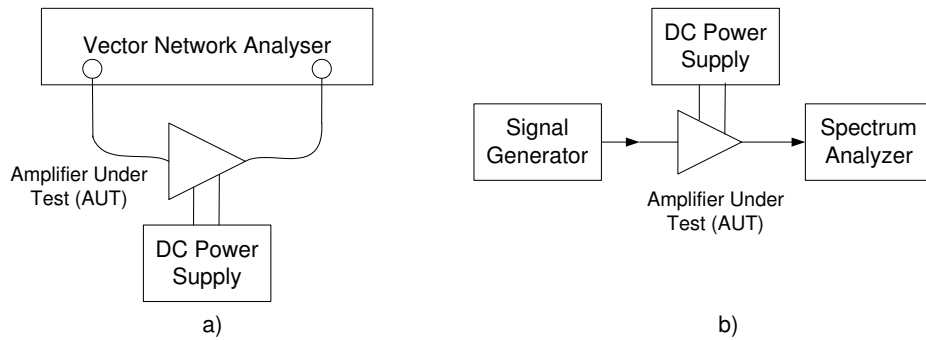


**Figure 5.20:** Amplifier measurement setup.
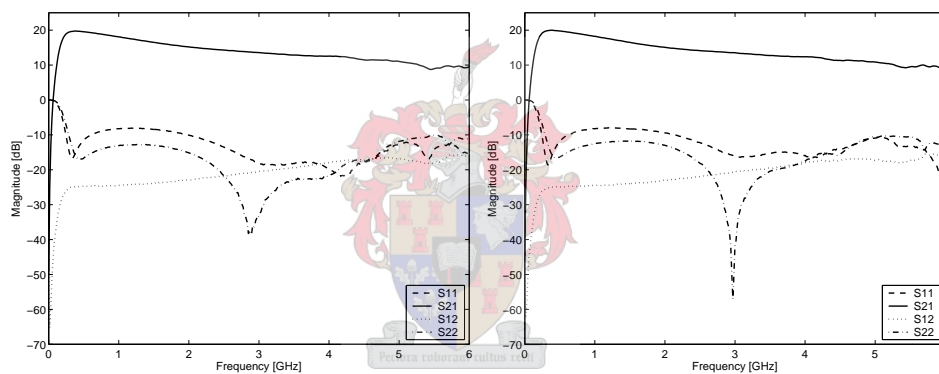


**Figure 5.21:** Measured S-parameters of the HMC476MP86 amplifiers.

The measurement setup shown in Figure 5.20(b) was used to evaluate the 1dB compression point of the amplifiers. The signal generator was set to 3GHz and swept from -80 to 10dBm while noting the output power on the HP8562 spectrum analyzer. Figure 5.22 shows the measured output power response of the HMC476MP86 amplifiers. Table 5.6 summarizes the measurements of the HMC476MP86 amplifiers at 3GHz.

### 5.3.2 IF Amplifiers

The test setups used in section 5.3.1 are repeated for amplifiers in the $1^{st}$ IF stage. Table 5.7 summarizes the specifications of the ERA3 and ERA51SM amplifiers from MiniCircuits [42].

Figures 5.23 and 5.24 show the measured s-parameters and output power response of the ERA3 amplifiers. Table 5.9 summarizes the measurements of the ERA3 amplifiers at 1.1GHz.
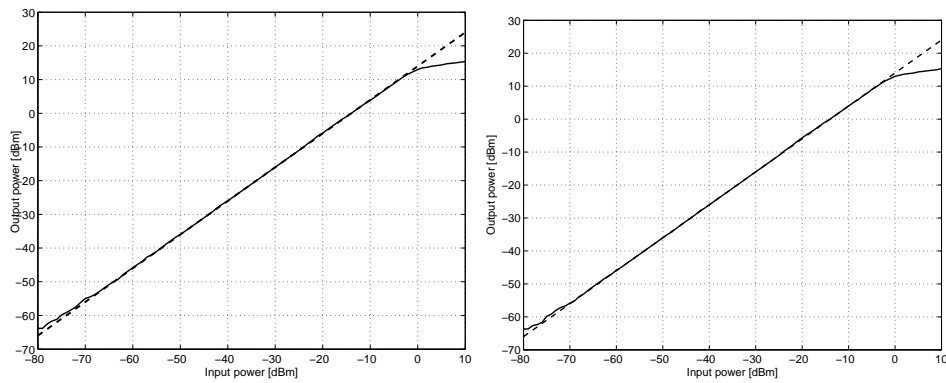
**Figure 5.22:** Measured output power response of the HMC476MP86 amplifiers.

| Gain [dB] | Output 1 dB pt. [dBm] | Input Return loss [dB] | Output Return loss [dB] |
|-----------|------------------------|-------------------------|--------------------------|
| 13.5 | 11 | 16.2 | 41.9 |
| 13.6 | 11 | 18.2 | 33.1 |

**Table 5.6:** Measured performance of the HMC476MP86 amplifiers.

| | Min. Gain [dB] | Noise Figure [dB] | Min. Output 1 dB pt. [dBm] | Input Return loss [dB] | Output Return loss [dB] |
|---------|----------------|--------------------|-----------------------------|-------------------------|--------------------------|
| ERA3 | 22 | 3.8 | 12.1 | 11.7 | 11.7 |
| ERA51SM | 17 | 4.1 | 18 | 26 | 20.83 |

**Table 5.7:** Properties of the ERA3 and ERA51SM amplifiers.

| | Gain [dB] | Output 1 dB pt. [dBm] | Input Return loss [dB] | Output Return loss [dB] |
|-----------|-----------|------------------------|-------------------------|--------------------------|
| Σ-channel | 19.5 | 13 | 9.4 | 25.3 |
| Δ-channel | 19.4 | 13 | 8.8 | 15.7 |

**Table 5.8:** Measured performance of the ERA3 amplifiers.
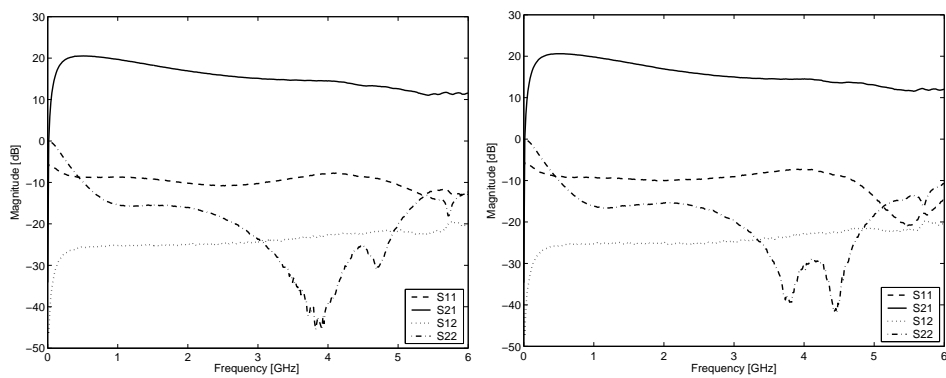


**Figure 5.23:** Measured S-parameters of the ERA3 amplifiers.
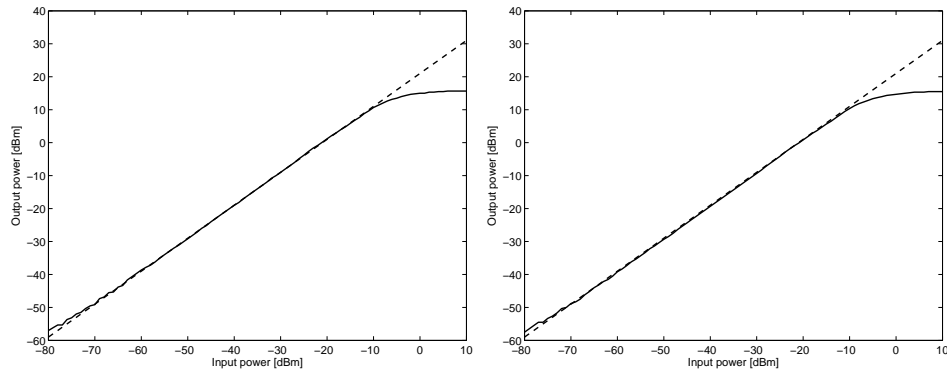
**Figure 5.24:** Measured output power response of the ERA3 amplifiers.

The measurements performed on the ERA51SM amplifiers are shown in Figures 5.25 and 5.26.
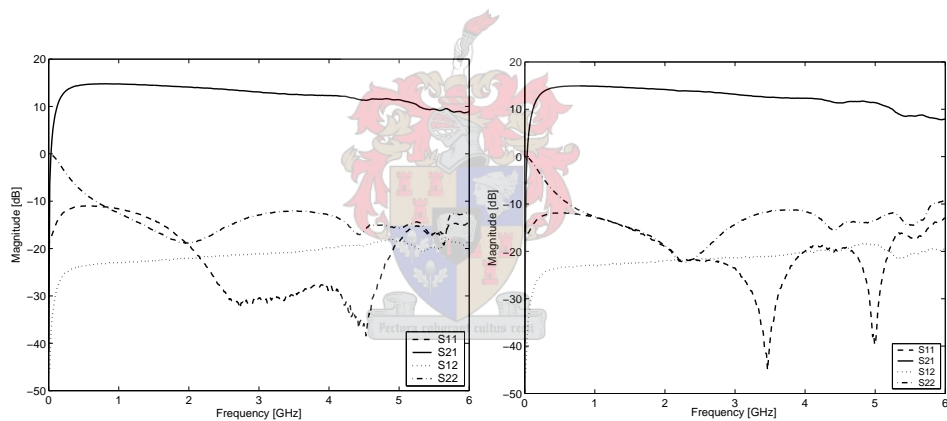


**Figure 5.25:** Measured S-parameters of the ERA51SM amplifiers.
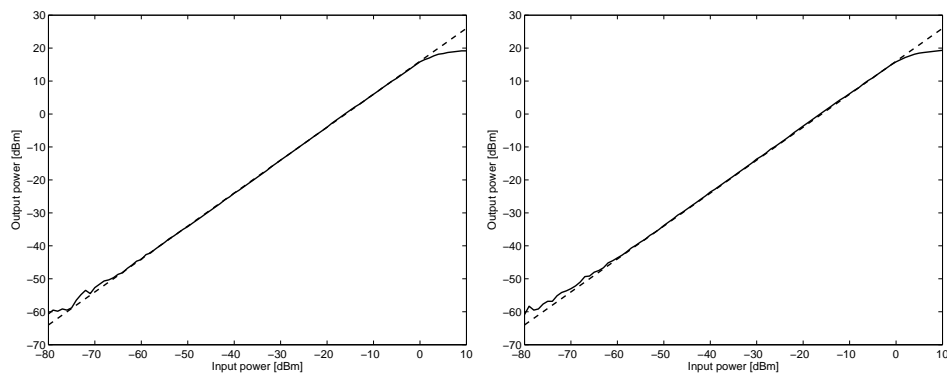


**Figure 5.26:** Measured output power response of the ERA51SM amplifiers.

Table 5.9 summarizes the measurements of the ERA51SM amplifiers at 1.1GHz.

|  | Gain [dB] | Output 1 dB pt. [dBm] | Input Return loss [dB] | Output Return loss [dB] |
|---|---|---|---|---|
| Σ-channel | 14.8 | 18 | 13.1 | 13.1 |
| Δ-channel | 14.7 | 18 | 11.9 | 13.2 |

**Table 5.9:** Measured performance of the ERA51SM amplifiers.

### 5.3.2.1 Conclusion

The tests performed in this section are to verify the performance of the amplifiers used in designing the PCM radar receiver. The amplifiers performs as expected, except the gains of the ERA3 and ERA51SM amplifiers are 2.5dB and 2.2dB below their respectively expected values.

## 5.4 Mixers Measurement

### 5.4.1 Local Oscillator Signals

The LOs designed in section 5.2 were used to drive the LO ports of the $1^{st}$ and $2^{nd}$ mixers. The output powers, however, divided equally in order to supply both channels of the PCM radar receiver. Figure 5.27 shows a photograph of the LOs connected to the harmonic suppression power dividers designed in chapter 4.



**Figure 5.27:** A photograph of the designed LOs with power dividers.

The spectrum of the 1.9GHz and 1.1107GHz LOs, after power division are shown in Figures 5.28 and 5.29, respectively. The output power levels are read as 7.92dBm and 9.58dBm respectively for the 1.9GHz and 1.1107GHz LOs. The $2^{nd}$ harmonics are suppressed by 51.15dB and 45.26dB respectively for the 1.9GHz and 1.1107GHz LOs. The additional $2^{nd}$ harmonic attenuation comes from the power dividers, which were specifically designed to attenuate the even harmonics.
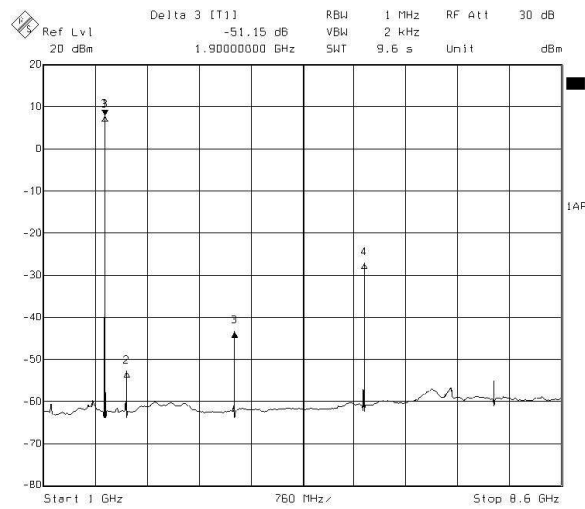
**Figure 5.28:** Output spectrum of the 1.9GHz LO after power division.
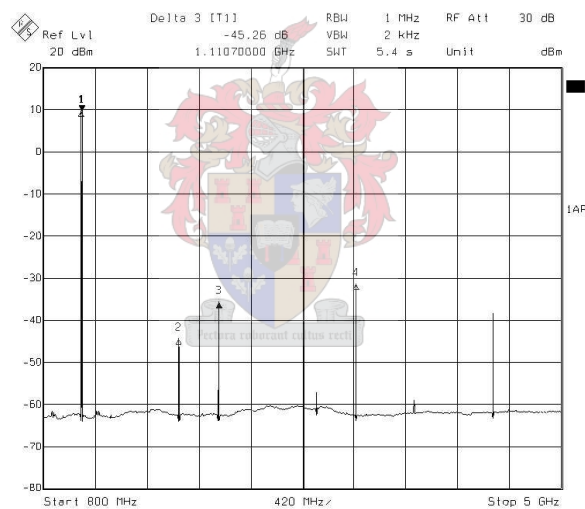


**Figure 5.29:** Output spectrum of the 1.1107GHz LO after power division.

## 5.4.2   $1^{st}$ **Mixers**

Two HMC213MS8 mixers from Hittite translate the received S-band signals to L-band. The properties of these mixers, as obtained from the datasheet [44], are summarized in Table 5.10.

| Conversion loss [dB] | Input 1dB pt [dBm] | RF return loss [dB] | IF return loss [dB] | Isolation[dB] | |
|---|---|---|---|---|---|
| | | | | RF to IF | LO to IF |
| 9 | 8 | 11.2 | 9 | 23 | 26 |

**Table 5.10:** Properties of the HMC213MS8 mixer.

Figure 5.30 shows the physical implementation of the HMC213MS8 mixers, where matching

circuits are included for better performance.
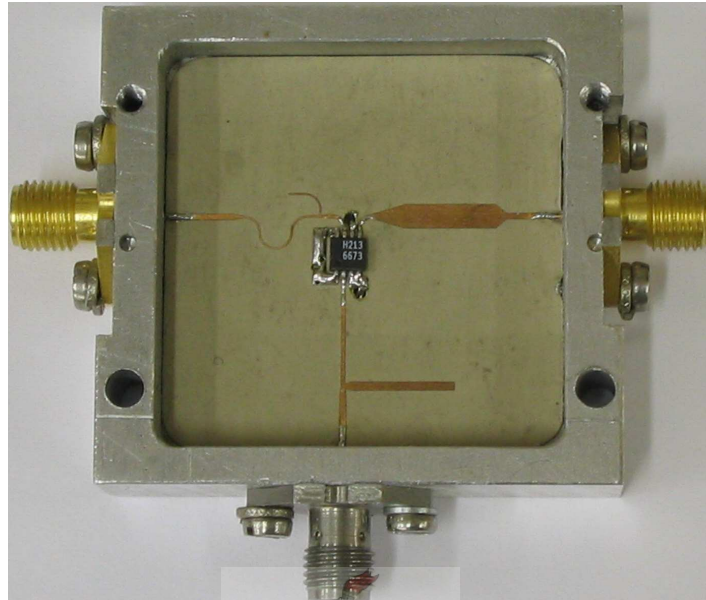


**Figure 5.30:** Physical implementation of the HMC213MS8 mixer.

Figure 5.31(a) shows the test setup used to measure the RF and IF port return losses of the mixers, where one of the ports is terminated in a matched load while taking measurement of the other port.
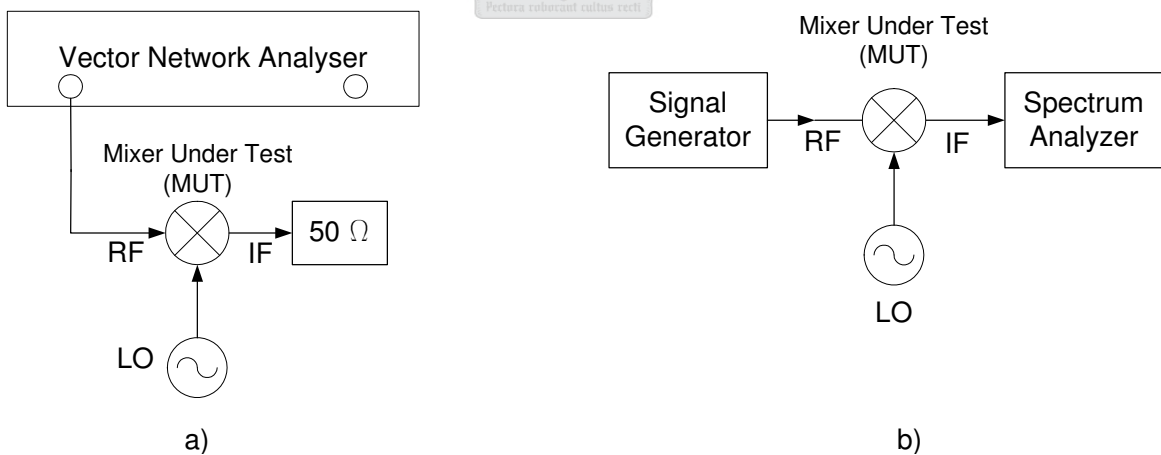


**Figure 5.31:** Mixer measurement setup.

The conversion loss, isolation between the ports and the 1dB compression point are measured using the setup shown in Figure 5.31(b). In conversion loss and isolation measurement, the signal generator frequency and power are swept from 2 to 4GHz and -80 to 10dBm, respectively. In the 1dB compression point measurement, the signal generator is set to 3GHz and the power at the RF port is swept from -80 to 10dBm . The measurements

of the HMC213MS8 mixers are plotted in Figures 5.32 to 5.35.
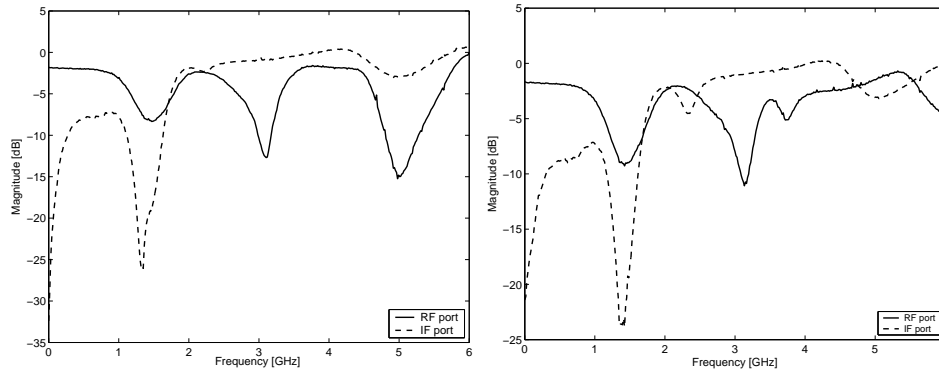


**Figure 5.32:** Measured return losses of the RF and IF ports of the HMC213MS8 mixers.
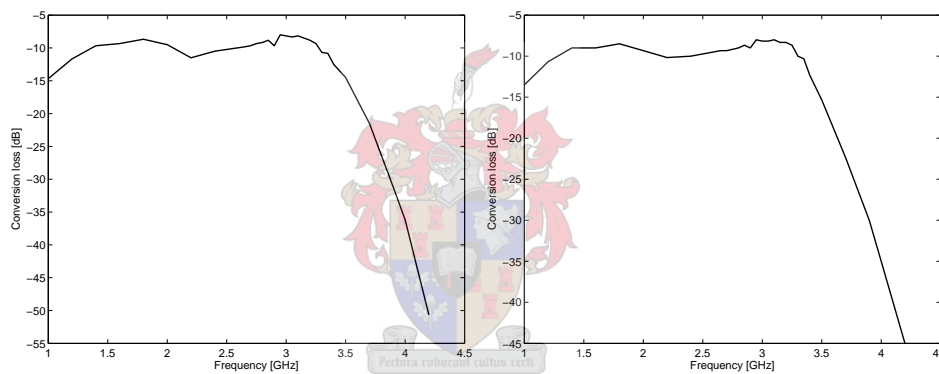


**Figure 5.33:** Measured conversion losses of the HMC213MS8 mixers.
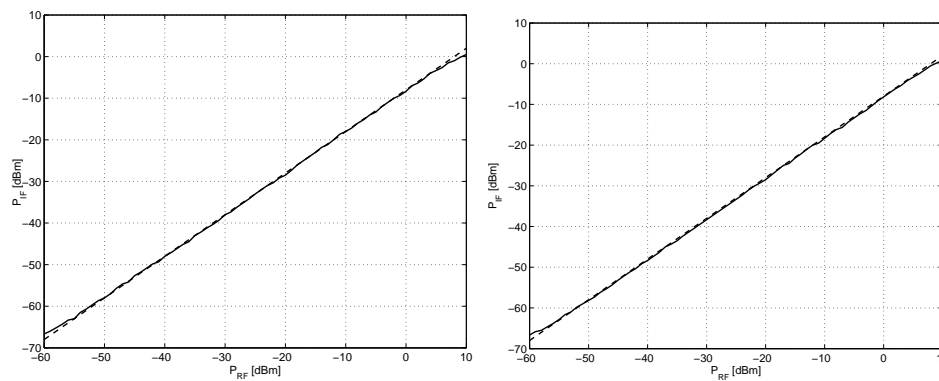


**Figure 5.34:** Measured input versus output powers of the HMC213MS8 mixers.

Table 5.11 summarizes the results of the HMC213 mixers at RF=3GHz and IF = 1.1GHz.
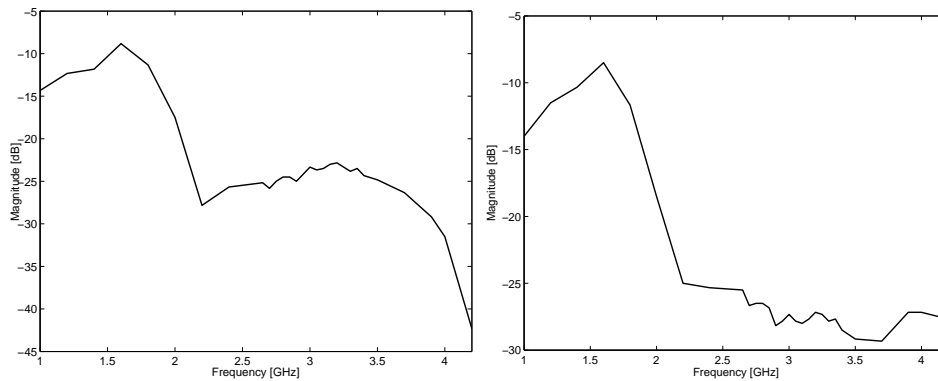
**Figure 5.35:** Measured RF to IF isloation of the HMC213MS8 mixers.

| | Conversion loss [dB] | Input 1dB pt [dBm] | RF return loss [dB] | IF return loss [dB] | Isolation[dB] | |
|---|---|---|---|---|---|---|
| | | | | | RF to IF | LO to IF |
| $\Sigma$-channel | 8.17 | 8 | 10.2 | 9.2 | 23.34 | 20.33 |
| $\Delta$-channel | 8.17 | 8 | 7.94 | 8.3 | 27.33 | 22 |

**Table 5.11:** Measured performance of the $1^{st}$ mixers.

### 5.4.3  $2^{nd}$ **Mixers**

The measurement setups employed in section 5.4.2 are exactly repeated to measure the performance of the $2^{nd}$ IF stage mixers. Two HMC213MS8 mixers from Hittite were used to downconvert the L-band signals(1.1GHz) to 10.7MHz. Table 5.12 summarizes the properties of the $2^{nd}$ mixers as obtained from the datasheet [44].

| Conversion loss [dB] | Input 1dB pt [dBm] | RF return loss [dB] | IF return loss [dB] | Isolation[dB] | |
|---|---|---|---|---|---|
| | | | | RF to IF | LO to IF |
| 7.5 | 7 | 10 | 12 | 18 | 40 |

**Table 5.12:** Properties of HMC207S8

Figure 5.36 shows the physical implementation of the HMC213MS8 mixers, where matching circuits are included to improve port return losses. The complete measurement of the HMC207 mixers are shown in Figures 5.37 - 5.40, while Table 5.13 summarizes the results of the HMC207 mixers at RF=1.1GHz and IF = 10.7MHz.

## 5.5  Conclusion

The performance of the $1^{st}$ and $2^{2nd}$ mixers were investigated by measuring different characteristics of the mixers such as port return losses, conversion loss and isolation between ports. The mixers performs as expected, except a small deterioration in the conversion and
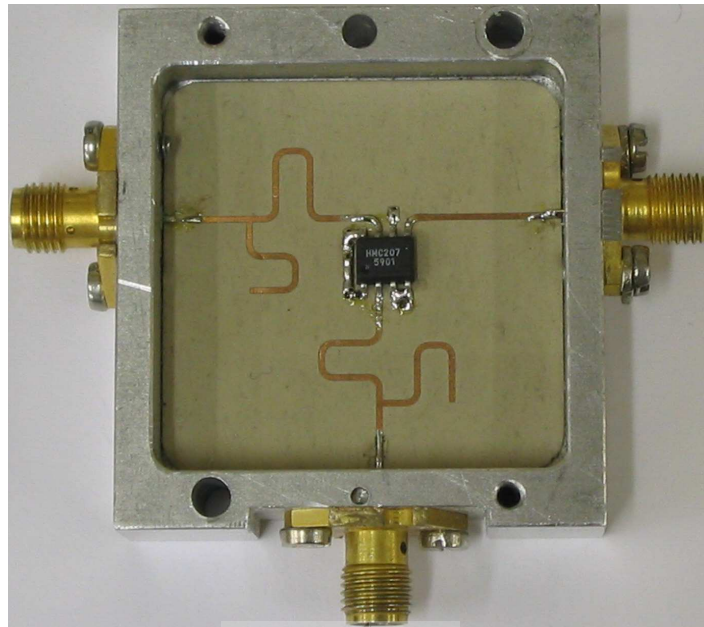
**Figure 5.36:** Physical implementation of the HMC207 mixer.
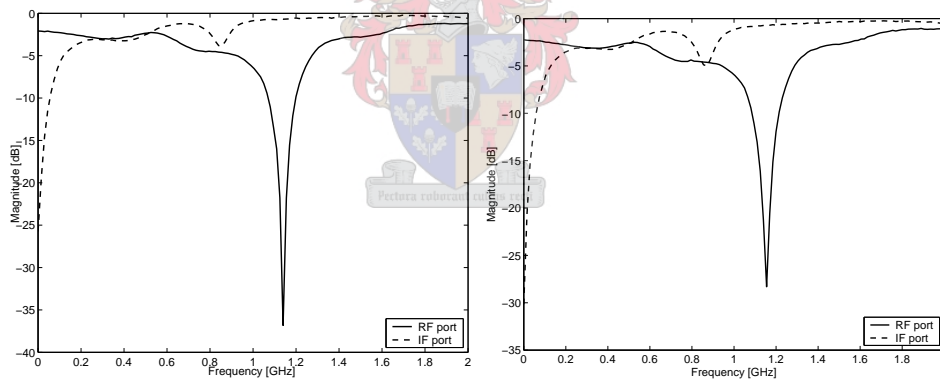


**Figure 5.37:** Measured return losses of the RF and IF ports of the HMC207 mixers.
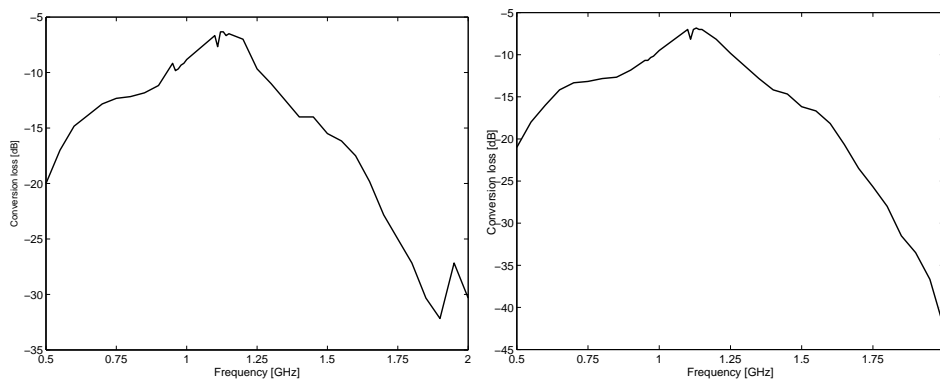


**Figure 5.38:** Measured conversion losses of the HMC207 mixers.
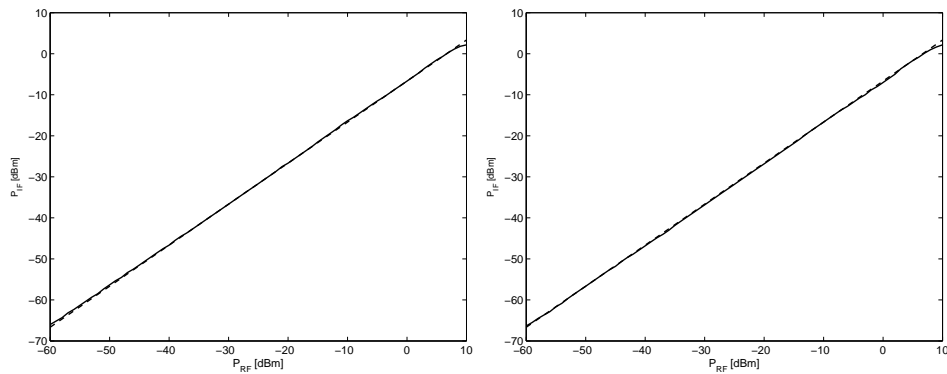
**Figure 5.39:** Measured input versus output powers of the HMC207 mixers.
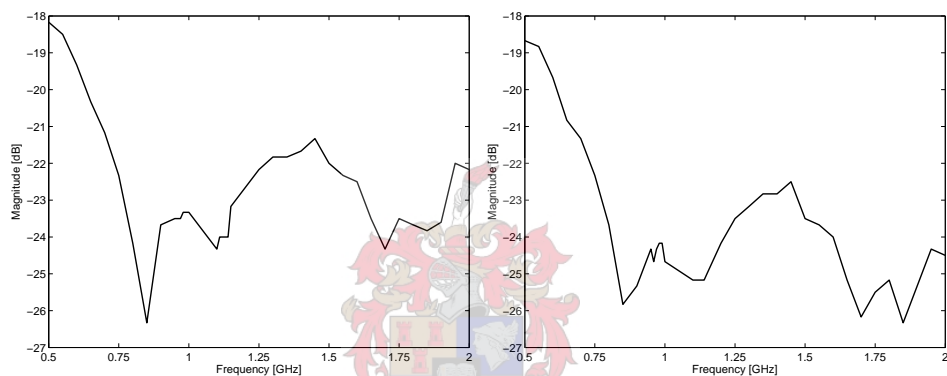


**Figure 5.40:** Measured RF to IF isolation of the HMC207 mixers.

| Conversion loss [dB] | Input 1dB pt [dBm] | RF return loss [dB] | IF return loss [dB] | Isolation[dB] | |
|---|---|---|---|---|---|
| | | | | RF to IF | LO to IF |
| 7.8 | 9.7 | 14.4 | 21.2 | 24 | 36.83 |
| 7.8 | 9.6 | 11.7 | 23.46 | 25 | 40.17 |

**Table 5.13:** Measured performance of the $2^{nd}$ mixers.

return losses. These discrepancies can be attributed to the decrease of LO strength and man-ufacturing inconsistency of the matching networks added at the ports of the mixers.

# Chapter 6

# PCM Radar Performance Evaluation

## 6.1  Introduction

In chapters 4 and 5 the focus was on the design and evaluation of the various passive and active sub-systems of the PCM radar receiver. The sub-systems were connected via low loss and phase stable coaxial cables, to form the complete PCM radar receiver shown in Figure 6.1. The aim of this chapter is to investigate the performance of the receiver and the complete PCM radar. Section 6.2 presents the performance of the receiver in terms of insertion loss and noise figure, while section 6.3 deals with the preliminary test results of the complete PCM radar tracking a moving target.
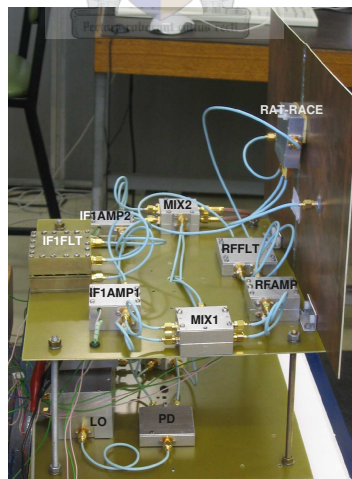


**Figure 6.1:** Final implementation of the PCM radar receiver.

## 6.2  Receiver Performance Evaluation

In this section the performance of the $\Sigma$ and $\Delta$-channels of the PCM radar receiver are evaluated in terms of insertion loss and noise figure measurements.

### 6.2.1 Insertion Loss

This test determines the losses in the two channels of the PCM radar receiver when a signal is fed through the RFFLTs from a signal generator and the output is measured using the Rohde and Schwarz FSEK 30 spectrum analyzer. The measurement setup used is shown in Figure 6.2.
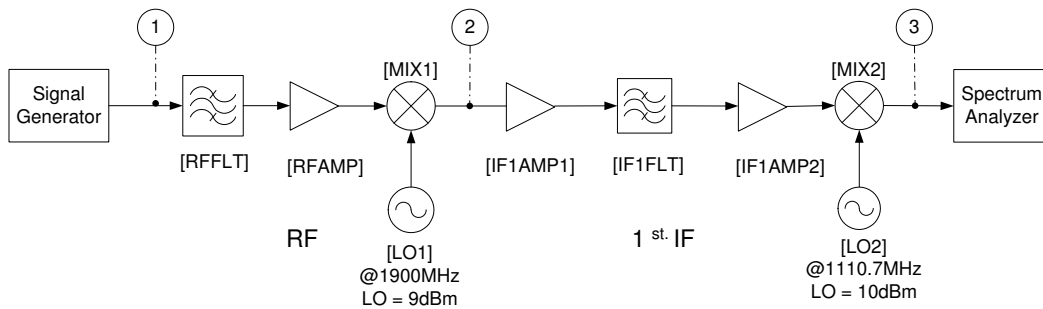


**Figure 6.2:** Receiver insertion loss measurement setup.

Before any measurements were done, the power level and frequency of the input signal was monitored on the spectrum analyzer to verify that it would not saturate or damage the active sub-systems. The input power level was set to -31dBm, at a frequency of 3GHz. Figure 6.3 shows the input signal as measured on the spectrum analyzer.
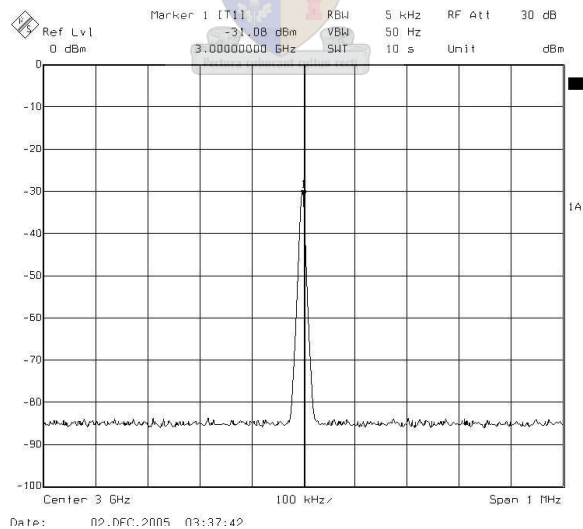


**Figure 6.3:** Input signal level.

The spectrum analyzer was connected at the output of each sub-system. The measured results at the $1^{st}$ IF [point 2] and $2^{nd}$ IF [point 3] of the Σ-channel of the PCM radar receiver are respectively shown in Figures 6.4 and 6.5, whereas that of the Δ-channel are respectively shown in Figures 6.6 and 6.7. As expected, the $1^{st}$ IF (point 2 of Figure 6.2) and $2^{nd}$ (point 3

of Figure 6.2) IFs are centered at 1.1GHz and 10.7MHz, respectively.
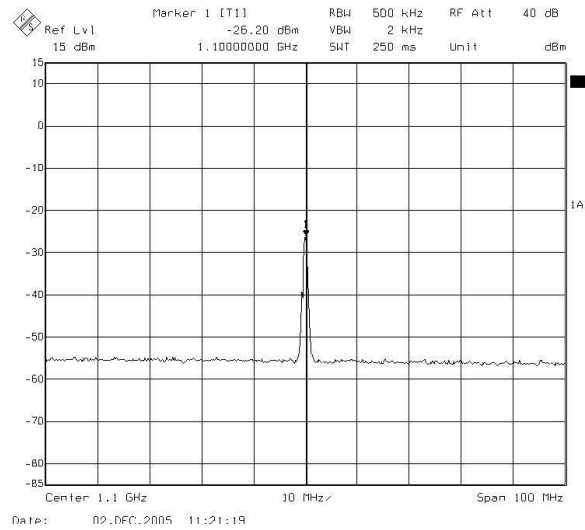


**Figure 6.4:** Measured output power level at the $1^{st}$ IF of the $\Sigma$-channel.
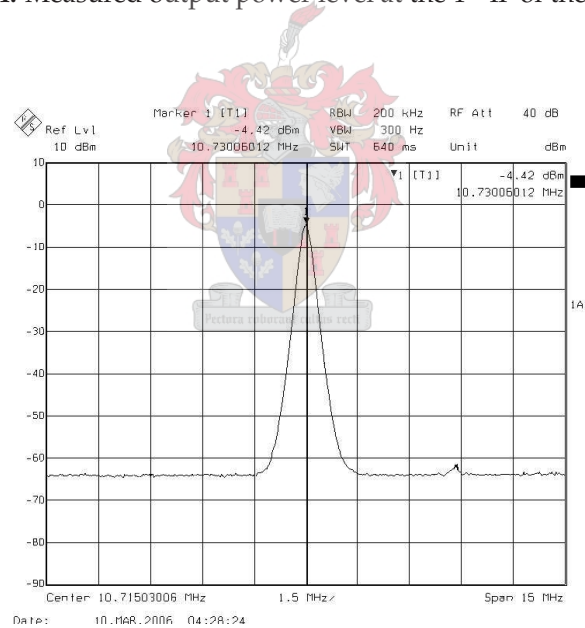


**Figure 6.5:** Measured output power level at the $2^{nd}$ IF of the $\Sigma$-channel.

Table 6.1 shows the power levels measured at different sections of the PCM radar receiver. The cumulative gains of the $\Sigma$ and $\Delta$-channels are respectively 26.66dB and 26.81dB, which are respectively 7.84dB and 7.69dB below the theoretical gain of 34.5dB (upto MIX2 of Table 3.1). The difference between the measured and calculated gains can be attributed to the difference beween the specified and measured gains of the IF amplifers and losses in the interconnecting coaxial cables. The measurements taken at various sections of the PCM radar receiver are available in appendix E.
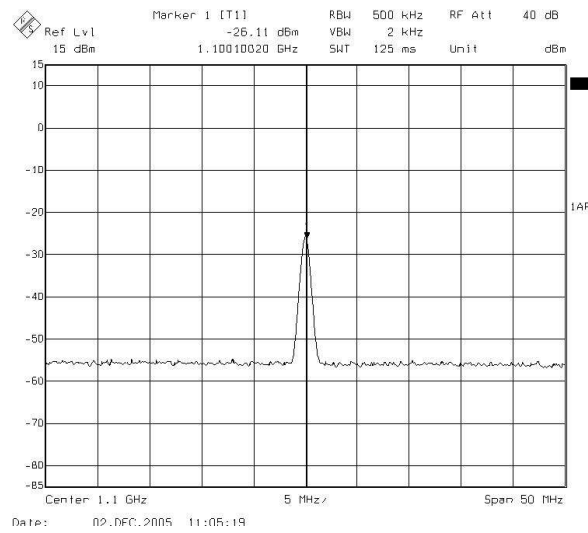
**Figure 6.6:** Measured output power level at the $1^{st}$ IF of the $\Delta$-channel.
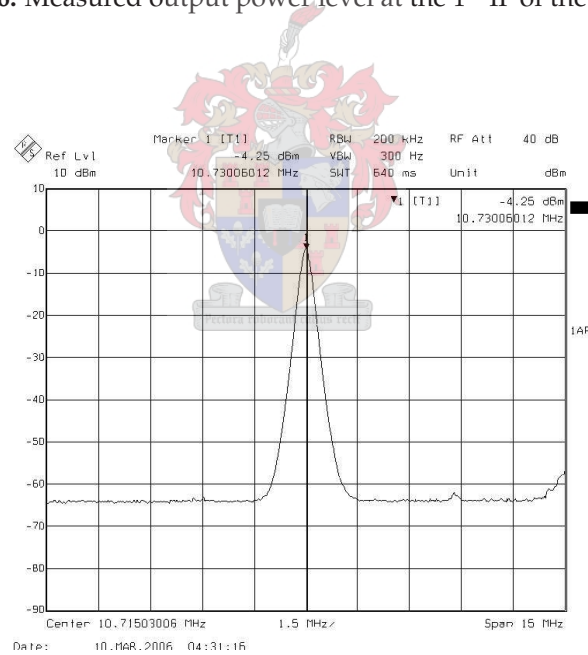


**Figure 6.7:** Measured output level at the $2^{nd}$ IF of the $\Delta$-channel.

|  | Input | RFFLT | RFAMP | MIX1 | IF1AMP1 | IF1FLT | IF1AMP2 | MIX2 |
|---|---|---|---|---|---|---|---|---|
| $\Sigma$-channel | -31.08 | -32.08 | -18.76 | -26.20 | -7.15 | -8.98 | 5.01 | -2.76 |
| $\Delta$-channel | -31.08 | -32.08 | -18.65 | -25.62 | -7.22 | -9.02 | 4.73 | -3.09 |

**Table 6.1:** Measured output levels of the PCM radar receiver.

### 6.2.2    Noise Figure Measurement

The noise figures of the Σ and Δ-channels of the PCM radar receiver were measured on the HP8970B noise figure meter. The measurement setup used is shown in Figure 6.8, where the HP 346B noise source is connected to RFFLT while the noise figure is connected to MIX2. The measurement setup was calibrated to compensate for possible noise contribution to the receiver.
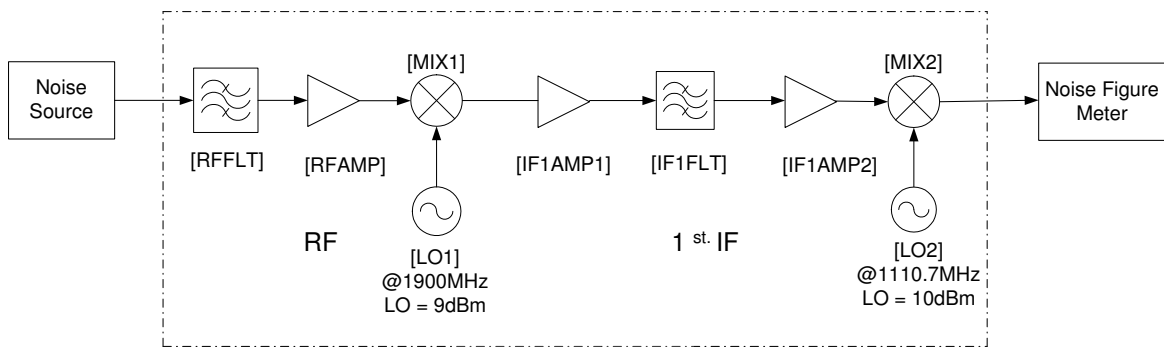


**Figure 6.8:** Noise figure measurement setup.

Figure 6.9 show the measured noise figure of the Σ and Δ-channels of the receiver over a bandwidth of 500MHz. The measured noise figures of the Σ and Δ-channels of the PCM radar receiver are respectively 7.45 and 7.80dB at 3GHz, which are 2.12dB and 2.47dB higher than the theoretical noise figure of 5.33dB (Table 3.1). The difference between measured and calculated noise figures can be attributed to the mismatches at the front ends of the receiver.
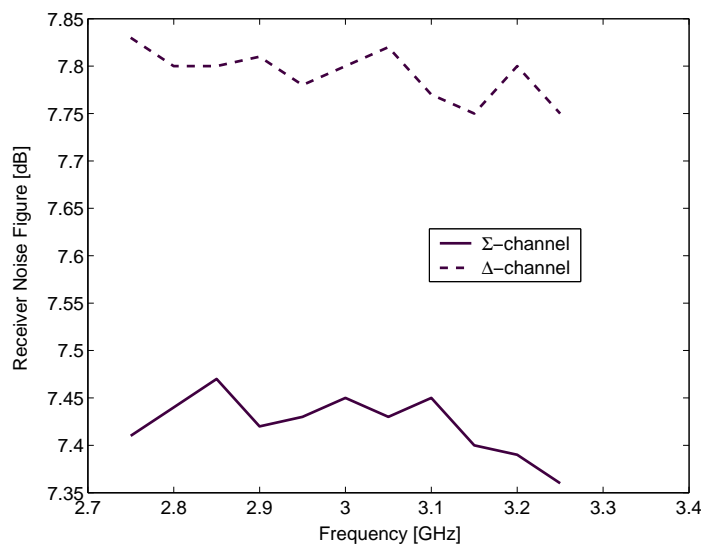


**Figure 6.9:** Measured noise figure of the Σ and Δ-channels of PCM radar receiver.

As a secondary result of the noise figure measurement, the cumulative gain of the $\Sigma$ and $\Delta$-channels of the PCM radar receiver are shown in Figure 6.10 over an RF frequency of 2.75GHz to 3.25GHz. The cumulative gain of the $\Sigma$ and $\Delta$-channels at 3GHz are respectively 30.54dB and 29.74dB.
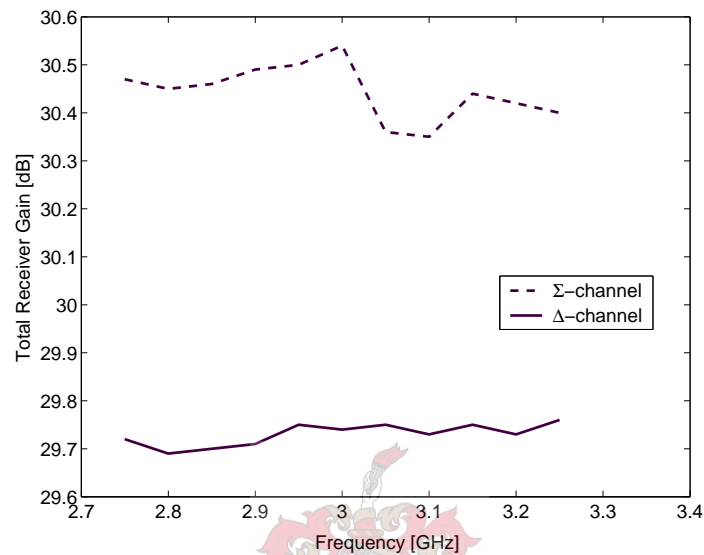


**Figure 6.10:** Measured gain of the $\Sigma$ and $\Delta$-channels of PCM radar receiver.

A photograph of the PCM radar receiver measurement setup is shown in Figure 6.11.
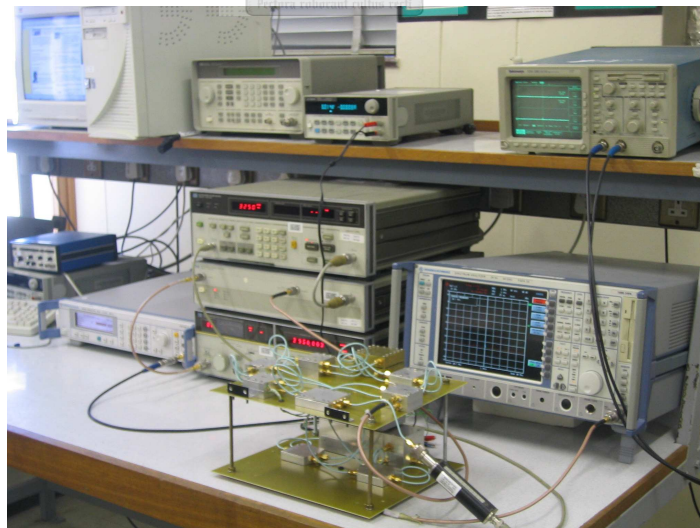


**Figure 6.11:** A photograph of the PCM radar receiver measurement setup.

## 6.3 PCM Radar Performance Evaluation

To evaluate the performance of the PCM radar, the $0^o/180^o$ microwave hybrid designed in section 4.2 was connected to the existing antennas via short, low-loss and phase stable coaxial cables. A photograph of the PCM radar measurement setup is shown in Figure 6.12, a target (a monopole antenna transmitting continuous RF signal at 3GHz) was horizontally moved while measuring the output of the $\Sigma$ and $\Delta$-channels of the PCM radar receiver on an oscilloscope. Figures 6.13 and 6.14 show the measured $\Sigma$ and $\Delta$-signals for target at -4.38$^o$ and 4.38$^o$ relative to the system boresight-axis. Comparison of the phase angles of the $\Sigma$ and $\Delta$-signals shows that they switch from -90$^o$ to 90$^o$ as the target passes the system boresight-axis.



**Figure 6.12:** PCM radar measurement setup.
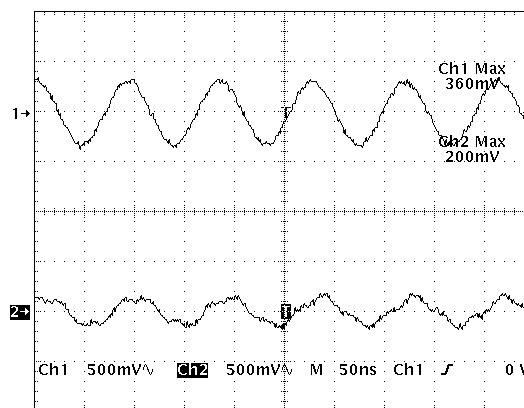


**Figure 6.13:** Measured output of the $\Sigma$ and $\Delta$-channels for target at $\theta$=-4.38$^o$ relative to the system boresight-axis.
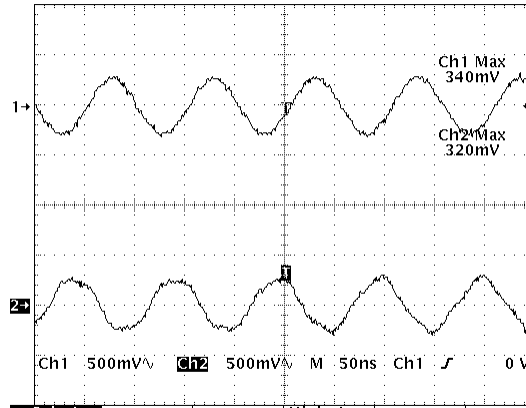
**Figure 6.14:** Measured output of the Σ and Δ-channels for target at $\theta$=4.38$^o$ relative to the system boresight-axis.

The Σ and Δ-signals measured for various tracking angles are included in appendix F. Table 6.2 summarizes the measured amplitude of the sum (Σ) and difference (Δ)-signals for the target at various tracking angles $\theta$ relative to system boresight-axis.

| Tracking angle $\theta$ [degrees] | -7.3 | -5.84 | -4.38 | -2.92 | -1.46 | 0 | 1.46 | 2.92 | 4.38 | 5.84 | 7.3 |
|---|---|---|---|---|---|---|---|---|---|---|---|
| Σ-signal [mv] | 260 | 280 | 360 | 480 | 500 | 460 | 440 | 360 | 340 | 280 | 260 |
| Δ-signal [mv] | 320 | 280 | 200 | 140 | 80 | 100 | 180 | 280 | 320 | 320 | 380 |

**Table 6.2:** Measured amplitude of the Σ and Δ-channels for various target tracking angles $\theta$.
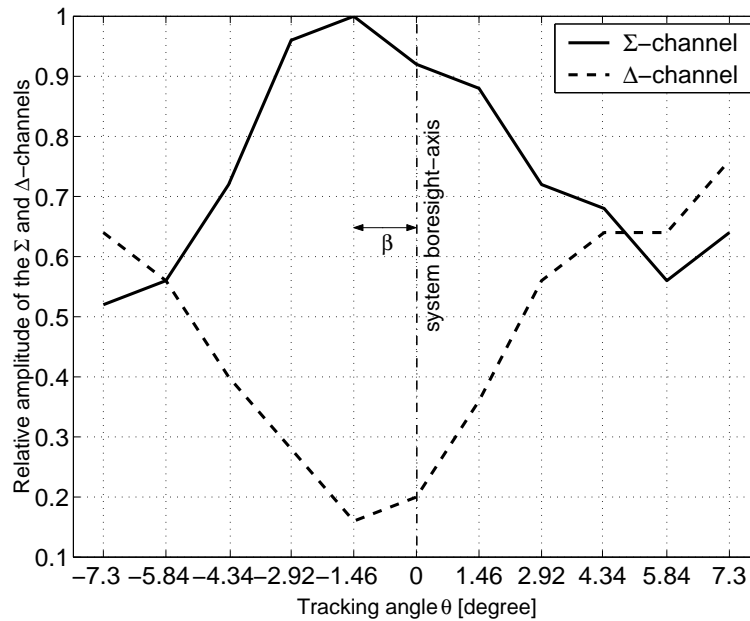


**Figure 6.15:** Measured relative amplitude of the Σ and Δ-channels the PCM radar receiver.

The relative amplitude of the $\Sigma$ and $\Delta$-channels has been plotted in Figure 6.15, where it can be seen that the null occurs at $\theta$=-1.46$^o$ relative to the system boresight-axis. The shift in system boresight-axis $\beta$ is attributed directly to pre-comparator phase unbalance $\gamma$ of 18.38$^o$, as obtained using eqn. (2.3.2).

## 6.4 Conclusion

In this chapter, the evaluations of the designed receiver and PCM radar were performed. The measured results of the receiver proved to meet the design specifications, except approximately 7.5dB and 2dB deterioration in gain and noise figure of both channels, respectively. The measured results of the PCM radar receiver can be summarized as:

|                  | $\Sigma$-channel | $\Delta$-channel |
|------------------|------------------|------------------|
| Gain [dB]        | 28.32            | 27.99            |
| Noise figure [dB]| 7.45             | 7.80             |

In the complete PCM radar measurement, the system is able to track a moving target over $\pm$7.3$^o$ with 80% accuracy, which can be still minimized by introducing a pre-comparator phase delay of 18.38$^o$.

# Chapter 7

# Conclusions and Recommendations

## 7.1 Conclusion

The main aim of thesis was to design, build and test an S-band receiver for phase-comparison monopulse (PCM) radar. During the design and implementation process, special attention was given to the optimization and balancing the corresponding sub-systems of the receiver which showed in accurate tracking.

A detailed investigation of the PCM radar was made. This led to a better understanding of the PCM radar operation and the influence of phase and amplitude unbalance between the channels of the receiver on the performance of the radar.

Prior to actual implementation of the receiver, a system level analysis was performed to decide on the architecture of the receiver and specification of the several sub-systems used to design the receiver. With dual downconversion stages ensuring image frequency rejection, the receiver gain was set to 30dB, which is sufficient in boosting the received signal to within the specifications of the phase sensitive detector selected for error signal (ES) detection.

Several passive and active sub-systems of the PCM radar receiver were designed and evaluated. These include:

- Two $0^o/180^o$ microwave hybrid structures were investigated and implemented. The modified $0^o/180^o$ microwave hybrid, which uses compensated T-junction at its ports, outperformed the conventional counter part in terms of return loss and bandwidth. Thus, it was chosen to perform the combination at the front of the PCM radar.

- Two microwave filters, a parallel-coupled microstrip-line and combline filters, were designed and manufactured. The measured results showed that both designs were

successful, except the bandwidth of the combline filter shrunk from the designed value.

- Two modified Wilkinson power dividers of equal power division and second harmonic suppression were designed for coherent operation of both channels of the PCM radar receiver. The measured results showed that both designs were successful.

- Two PLL synthesizer based local oscillators were also designed and manufactured to drive the LO ports of the mixers. The measured results show that both designs were successful, except the power level of the 1900MHz LO is 2.38dB below the designed value.

- The RF amplifiers and mixers are within the manufactures specifications, but the measured gains of the IF amplifiers are below the manufactures' specifications and this led to reduction of the complete receiver gain.

Both channels of the receiver were measured and worked very well in downconverting the RF signals from 3GHz to an IF of 10.7MHz, but the power levels at the output of both channels of the receiver are lower than the expected 4.5dBm (at the output of the second mixer). Losses in the cabling and connectors are the main contributing factors in attenuating the output signal. The noise figures were also measured to be 7.7.45dB and 7.80dB for the $\Sigma$ and $\Delta$-channels, respectively. Besides, the complete receiver operates from a single DC supply voltage of 12V and draws a maximum current of 584mA.

The designed receiver was connected to the existing antenna and the complete PCM radar was able track a moving target in 4.3m range and over $\pm 7.3^o$ of the system boresight-axis with 80% accuracy.

## 7.2 Recommendation for Future Development

Even though a successful receiver was implemented that proved in tracking a moving target, more development work is needed to improve the tracking accuracy of the radar. This mostly involves the introduction of additional phase delay to the antenna feed that is connected to port 2 of the $0^o/180^o$ microwave hybrid. The other areas, which require further modifications, are the active sub-systems used to implement the receiver. The VCOs used to realize the LOs; the amplifiers; and mixers should be accurately measured and characterized for the necessary optimization. Thus, new measurement setups and appropriate calibration kit need to be developed to remove errors associated with the measurement of these sub-systems. Once these modifications have been achieved, the $2^{nd}$ IF filters and phase sensitive detector, which could not be implemented due to shortage of time, should be implemented and interfaced with the servo-system to achieve the final objective - automatic tracking.

# Appendices

# Appendix A

# PCM Radar Analysis

## A.1 Introduction

Discussed in this appendix is the mathematical description of the PCM radar. Figure A.1 shows a two-dimensional PCM radar. For a target at an angle $\theta$ relative to the system boresight-axis, the antenna voltages may be given as follows:

$$V_A(t) \quad = \quad K\sin\omega_c t \tag{A.1.1}$$

$$V_B(t) \quad = \quad K\sin(\omega_c t + \phi) \tag{A.1.2}$$

where $\omega_c$ is the center frequency of the transmitted signal; $\phi$ is the phase delay between the received signals, which depends on the angular position of the target; and K is a constant, which is related to the transmitted power, range, scattering conditions and antenna parameters.
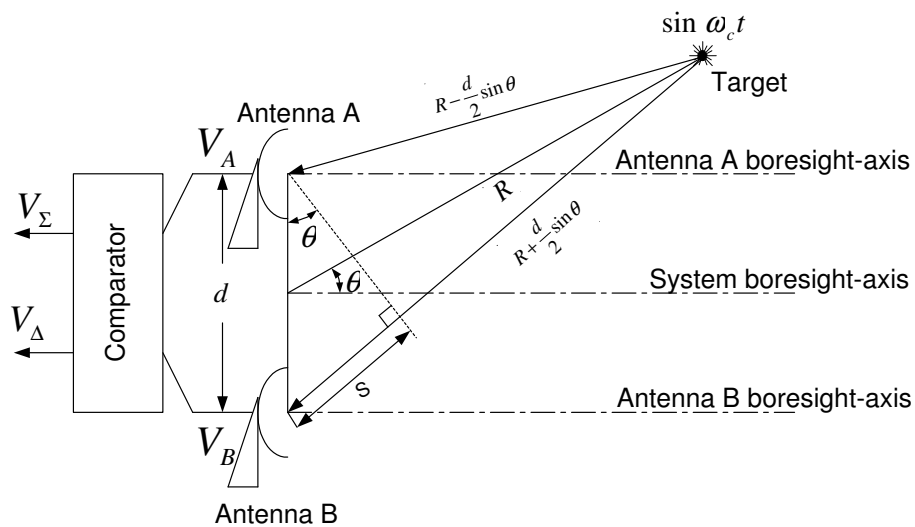


**Figure A.1:** PCM radar operation.

The signals received at the antennas are fed to a comparator to form the sum ($V_\Sigma$) and difference ($V_\Delta$) signals.

$$V_\Sigma = K\sin\omega_c t + K\sin(\omega_c t + \phi) \tag{A.1.3}$$

$$V_\Delta = K\sin\omega_c t - K\sin(\omega_c t + \phi) \tag{A.1.4}$$

Eqns. (A.1.3) and (A.1.4) can be rewritten as a single resultant voltage and phase angle as follows:

$$V_\Sigma = 2K\cos\left(\frac{\phi}{2}\right)\sin\left[\omega_c t + \tan^{-1}\left(\frac{\sin\phi}{\cos\phi + 1}\right)\right] \tag{A.1.5}$$

$$V_\Delta = 2K\sin\left(\frac{\phi}{2}\right)\sin\left[\omega_c t + \tan^{-1}\left(\frac{\sin\phi}{\cos\phi - 1}\right)\right] \tag{A.1.6}$$

Using the above derived equations, the relative amplitude and phase of the sum and difference channels, as a function of $\theta$, are respectively plotted in Figures 2.9 and 2.10. The phase reversal occurs at the system boresight-axis. With the basic operation of PCM radar discussed, an attempt is also made to evaluate the performance of the radar under pre-comparator phase and amplitude unbalances.

## A.2   Phase Unbalance Effects

For a pre-comparator phase unbalance $\gamma$, the voltages at the antennas are given as

$$V_{A\gamma}(t) = K\sin(\omega_c t - \gamma) \tag{A.2.1}$$

$$V_{B\gamma}(t) = K\sin(\omega_c t + \phi) \tag{A.2.2}$$

The corresponding sum ($V_{\Sigma\gamma}$) and difference ($V_{\Delta\gamma}$) signals are given as follows:

$$V_{\Sigma\gamma} = K\sin(\omega_c t - \gamma) + K\sin(\omega_c t + \phi) \tag{A.2.3}$$

$$V_{\Delta\gamma} = K\sin(\omega_c t - \gamma) - K\sin(\omega_c t + \phi) \tag{A.2.4}$$

Eqns. (A.2.3) and (A.2.4) can be rewritten as a single resultant voltage and phase angle as follows:

$$V_{\Sigma d} = 2K\cos\left(\frac{\phi + \gamma}{2}\right)\sin\left[\omega_c t + \tan^{-1}\left(\frac{\sin\phi - \sin\gamma}{\cos\phi + \cos\gamma}\right)\right] \tag{A.2.5}$$

$$V_{\Delta d} = 2K\sin\left(\frac{\phi + \gamma}{2}\right)\sin\left[\omega_c t + \tan^{-1}\left(\frac{\sin\phi + \sin\gamma}{\cos\phi - \cos\gamma}\right)\right] \tag{A.2.6}$$

The relative phase and amplitude of eqns. (A.2.5) to (A.2.6) have been plotted in Figures 2.11 and 2.12, where it can be seen that for $\gamma \neq 0$, a shift in the system's boresight-axis. This corresponds to an error in the pointing accuracy of the PCM radar.

## A.3   Amplitude Unbalance Effects

For pre-comparator amplitude unbalance $\ell$, the voltages at the antennas are given as

$$V_{A\ell}(t) \quad = \quad K\ell \sin \omega_c t \tag{A.3.1}$$

$$V_{B\ell}(t) \quad = \quad K \sin (\omega_c t + \phi) \tag{A.3.2}$$

The corresponding sum ($V_{\Sigma\gamma}$) and difference ($V_{\Delta\gamma}$) signals are given as follows:

$$V_{\Sigma\ell} = K\ell \sin \omega_c t + K \sin (\omega_c t + \phi) \tag{A.3.3}$$

$$V_{\Delta\ell} = K\ell \sin \omega_c t - K \sin (\omega_c t + \phi) \tag{A.3.4}$$

Eqns. (A.3.3) and (A.3.4) can be rewritten as a single resultant voltage and phase angle as follows:

$$V_{\Sigma a} \quad = \quad K\sqrt{(\ell \cos \phi + 1)^2 + (\ell \sin \phi)^2} \sin \left[ \omega_c t + \tan^{-1} \left( \frac{\ell \sin \phi}{\ell \cos \phi + 1} \right) \right] \tag{A.3.5}$$

$$V_{\Delta a} \quad = \quad K\sqrt{(\ell \cos \phi - 1)^2 + (\ell \sin \phi)^2} \sin \left[ \omega_c t + \tan^{-1} \left( \frac{\ell \sin \phi}{\ell \cos \phi - 1} \right) \right] \tag{A.3.6}$$

The relative phase and amplitude of eqns. (A.3.5) to (A.3.6) have been plotted in Figures 2.14 and 2.15, where there is no shift in system boresight axis. There is, however, 'fill in' in the null of the $\Delta$ signal, which will effectively reduce the resolution of the PCM radar.

# Appendix B

# L-Band Lumped Element Bandpass Filter Design

## B.1   Introduction

Discussed in this appendix is the design and implementation of an L-band lumped element bandpass filter. The specifications of the filter are as follows:

| | |
|---|---|
| Center frequency, $f_o$ | 1.1GHz |
| Bandwidth, BW | 2% |
| Stopband | $f \geq f_o$+44MHz and $f \leq f_o$-44MHz |
| Passband return loss, RL | 20dB |
| Stopband insertion loss, $A_s$ | 38dB |

**Table B.1:** Lumped element bandpass filter specifications.

## B.2   Design

The first step in the design is to obtain a suitable lowpass prototype that would yield the specified bandpass filter. Table B.2 summarizes the specifications of the lowpass prototype obtained using the lowpass to bandpass transformation [45].

| | |
|---|---|
| Passband cutoff frequency, $\omega_p$ | 1rad/sec |
| Stopband cutoff frequency, $\omega_s$ | 3.923rad/sec |
| Passband return loss, RL | 20dB |
| Stopband insertion loss, $A_s$ | 38dB |

**Table B.2:** Lowpass prototype specifications.

The order of a Chebyshev lowpass prototype is calculated as

$$
\begin{aligned}
n &\geq \frac{\cosh^{-1}\sqrt{\left(10^{A_s/10}-1\right)/\left(10^{A_p/10}-1\right)}}{\cosh^{-1}(\omega_s)}\\
&= \frac{\cosh^{-1}\sqrt{\left(10^{35/10}-1\right)/\left(10^{0.436/10}-1\right)}}{\cosh^{-1}(3.923)} = 2.995
\end{aligned}
$$

Thus, a $3^{rd}$ order lowpass prototype filter shown in Figure B.4(a) is synthesized. The element values are obtained from Table 8.4 of [5]. Figure B.4(b) shows the corresponding bandpass filter obtained using the lowpass to bandpass transformation illustrated in Figure B.1.
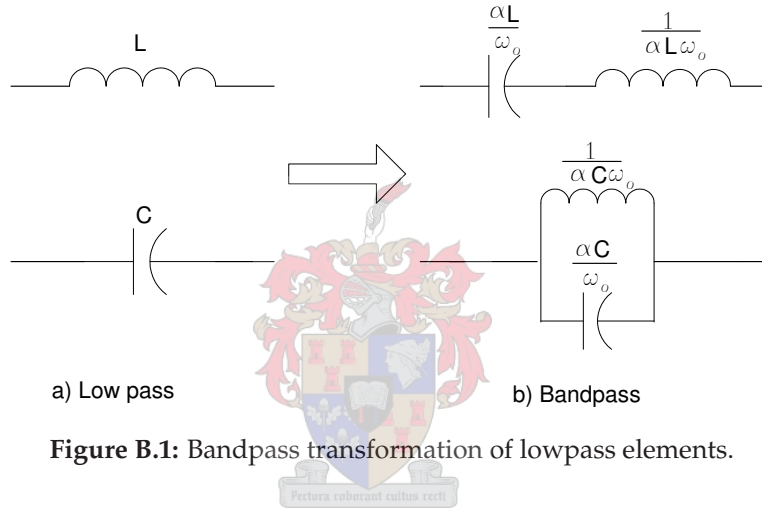


**Figure B.1:** Bandpass transformation of lowpass elements.

The bandwidth scaling factor, $\alpha$ in Figure B.1, is given by

$$
\alpha = \frac{\omega_o}{\omega_2 - \omega_1} \tag{B.2.1}
$$

where $\omega_o$, $\omega_2$ and $\omega_1$ are respectively the center, upper and lower cutoff angular frequencies of the bandpass filter.

Various transformations were performed on the bandpass filter to obtain the final filter configuration shown in Figure B.4(f), which can be easily implemented using microstrip transmission lines. First, the parallel resonant networks are converted into series resonant using the impedance inversion technique illustrated in Figure B.2. From Figure B.2, $C_2$ and $L_2$ can derived as

$$
C_2 = L_1(\omega_o C)^2 \tag{B.2.2}
$$

$$
L_2 = \frac{C_1}{(\omega_o C)^2} \tag{B.2.3}
$$

where C, in this design, was set to 174.69pF in order to get identical inductances over the entire filter. A narrow band capacitance transformer shown in Figure B.3 is used to transform the port impedances to 50Ω. The values of $C_a$ and $C_b$ are given by [24]

$$C_a = \frac{1}{\omega_o \sqrt{n^2 - 1}} \tag{B.2.4}$$

$$C_b = \frac{-\sqrt{n^2 - 1}}{n^2 \omega_o} \tag{B.2.5}$$

where n is equal to $\sqrt{50}$ for a 50Ω system. The resulting configuration is shown Figure B.4(c). A simple star (Y)-to-delta (Δ) and delta (Δ)-to-star (Y) transformations were carried on Figure B.4(c) and subsequent configurations (Figures B.4(d) and B.4(e)) to obtain the final configuration shown in Figure B.4(f). The complete procedure is illustrated in Figure B.4.
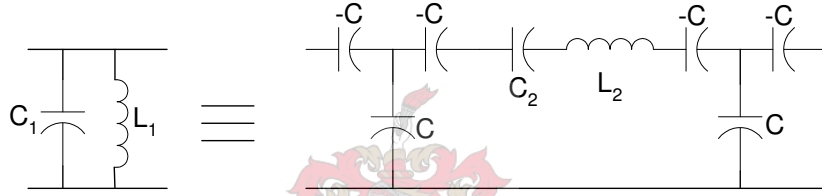


**Figure B.2:** Impedance inversion technique.
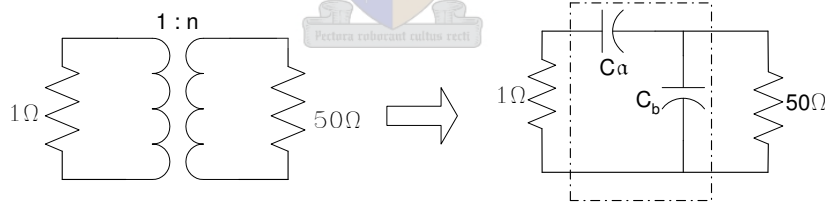


**Figure B.3:** Narrowband capacitance transformation.

## B.3 MWO Simulation

Shown in Figure B.5 is the Microwave Office (MWO) simulated response of the designed bandpass filter realized using ideal lumped elements. In the actual design, however, the parasitic effects of the lumped elemens should be accounted for. Thus, the capacitors were replaced by equivalent models of multilayer C06CF capacitors from Dielectric Laboratories, which is generated with the aid of CapCad software [46]; while the inductors were realized using microstrip transmission lines. Figure B.6 shows the MWO implementation of the designed bandpass filter. Several capacitors are connected in parallel to realize the required capacitances with on the shelf values. The emperical formula 1nH/mm/GHz was

**Figure B.4:** a) Lowpass prototype filter b) bandpass filter c) port impedance transformed series-resonant bandpass filter d) bandpass filter after Υ-Δ transformation e) bandpass filter after circuit combination and Δ-Y transformation f) final bandpass filter

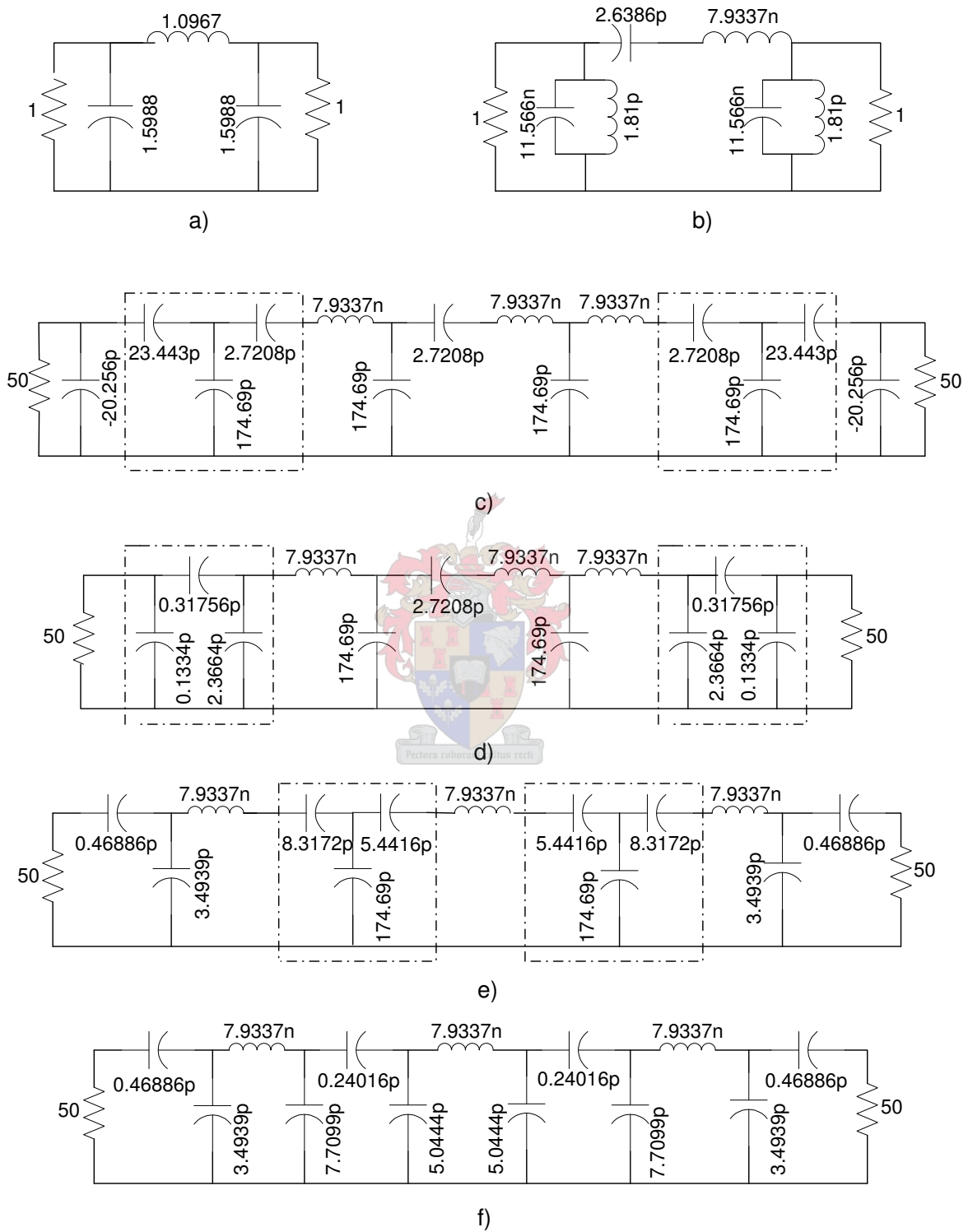used to calculate the intial length of the microstrip transmission lines used to realize the inductors. Both the capacitors and inductors were optimized to obtain the response shown in Figure B.7. One can see that the series capacitors are almost double of the design values, while shunt capacitors remain remain pretty much the same as the design values. This is attributed to the inherent shunt parasitic capacitances exist between the ground and conductor. The simulated insertion loss is 3.64dB at 1.1GHz, while the retun loss is better than 15dB across the bandwidth of the filter. The layout of the final bandpass filter is shown in Figure B.8.
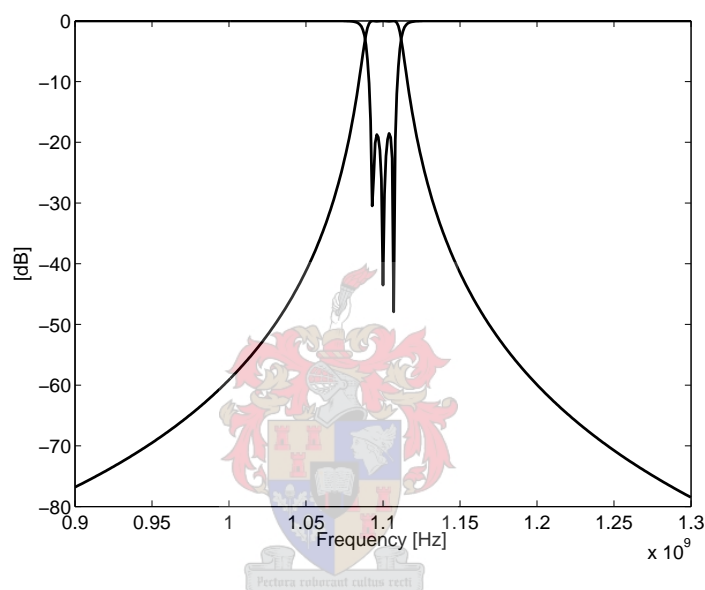


**Figure B.5:** Lumped element bandpass filter ideal response
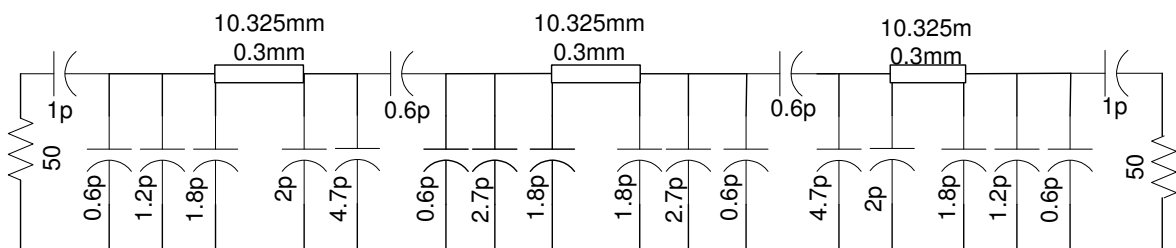


**Figure B.6:** MWO implementation of the designed bandpass filter.

## B.4   Measurement and Discussion

Shown in Figure B.9 is the actual lumped element bandpass filter fabricated on a RT/6010LM substrate of 10.2 dielectric constant and 0.635mm thickness.   The measured return and insertion loss of the designed bandpass filter are respectively shown in Figures B.10 and B.11.
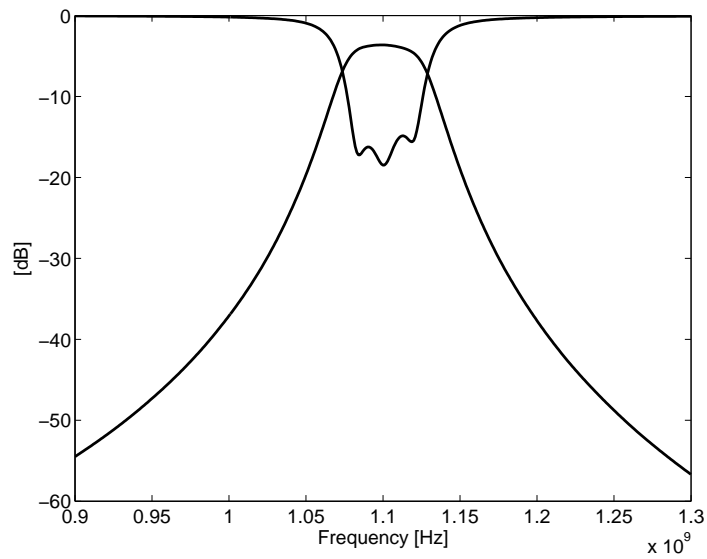
**Figure B.7:** Simulated response of the lumped element bandpass filter realized using CapCad capacitor models and microstrip transmission lines.
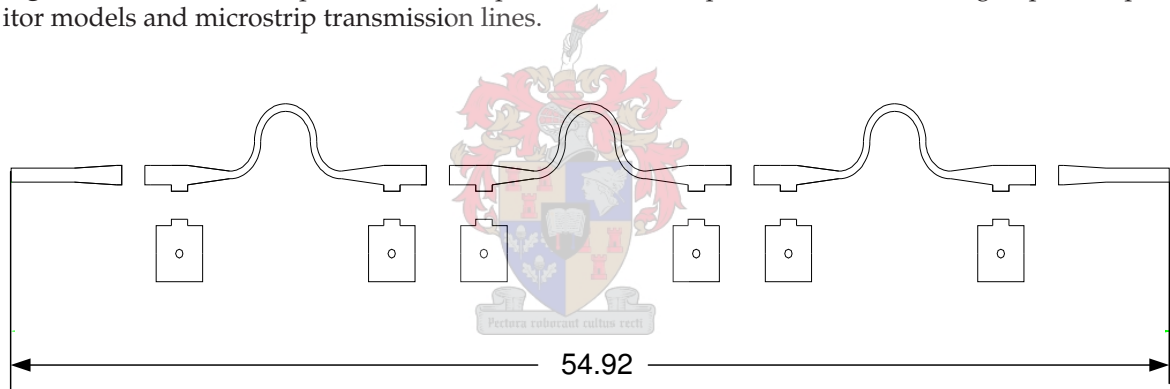


**Figure B.8:** Layout of the lumped element bandpass filter.
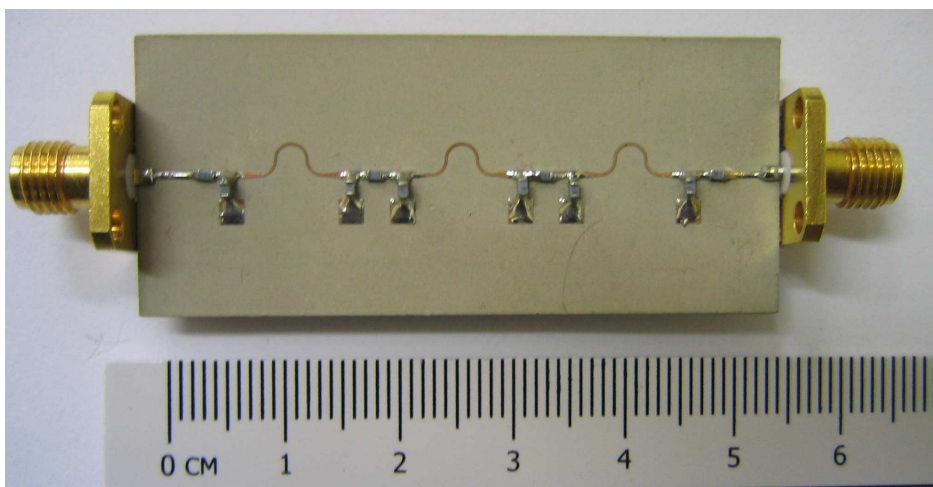


**Figure B.9:** A photograph of the designed lumped element bandpass filter.

Comparing the measured response with the simulated response, one can see a very significant difference between the results. The center frequency has shifted to 992.5MHz from the designed 1.1GHz, while the measured insertion and return loss have deteriorated to -16.77dB and -8.272dB, respectively.
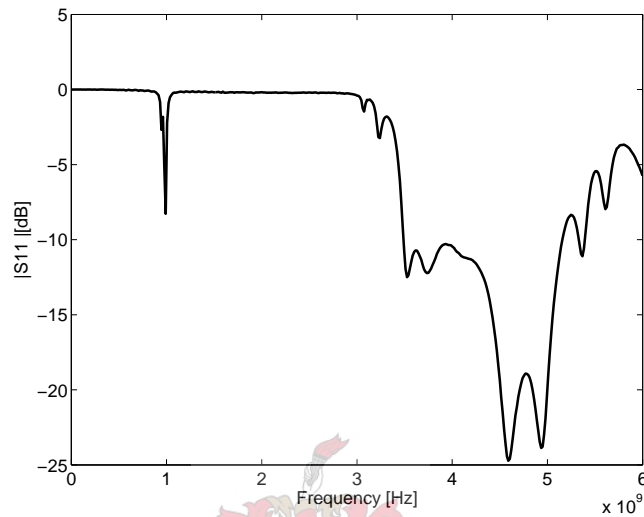


**Figure B.10:** Measured return loss.
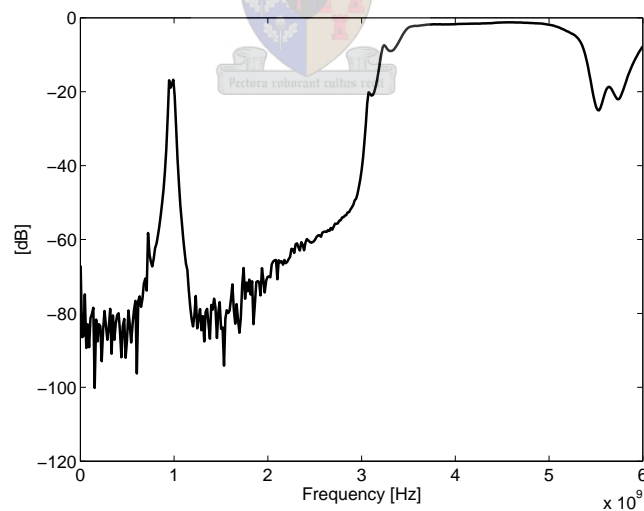


**Figure B.11:** Measured insertion loss.

The shift in the center frequency can be attributed to the accuracy of the dielectric permitivity of the substrate used to build the filter. Besides, the significant deterioration in insertion loss, having an 8.272dB return loss at the measured center frequency (992.5MHz), indicates that the input power is being lost in the capacitors.

## B.5 Conclusion

In this appendix, the design and implementation of an L-band lumped element bandpass filter was discussed. Even though the designed filter has failed to meet the design specifications, it can be optimized for better performance. The insertion loss can be improved using capacitors with small insertion loss, while shortening the microstrip lines used to realize the inductors will shift the center frequency to the desired value.
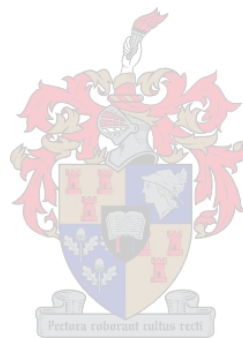
# Appendix C

# Data Sheet of 0805HQ Chip Inductors

## Chip Inductors – 0805HQ Series (2012)

RoHS COMPLIANT

The 0805HQ Series offers our highest Q factors in an 0805 form factor. In addition, current handling has been improved with significantly lower DCR values.

Like all Coilcraft wire wound ceramic chip inductors, the 0805HQ Series provides exceptional SRFs, tight inductance tolerance and batch consistency.

For even higher Qs, consider our surface mount spring inductors that combine the high Q of an air wound coil with the convenience of automatic placement.

Coilcraft **Designer's Kit C325** contains samples of all 5% inductance tolerance parts. To order, contact Coilcraft or visit **http://order.coilcraft.com**.

| Part number[1] | Inductance[2] (nH) | Percent tolerance[3] | Q min[4] | SRF min[5] (GHz) | DCR max[6] (Ohms) | Irms[7] (A) | Color code |
|---|---|---|---|---|---|---|---|
| 0805HQ-2N5X_L_ | 2.5 @ 250 MHz | **5** | 80 @ 1500 MHz | 10.30 | 0.020 | 1.6 | Black |
| 0805HQ-5N6X_L_ | 5.6 @ 250 MHz | **5** | 98 @ 1500 MHz | 6.10 | 0.035 | 1.6 | Brown |
| 0805HQ-6N2X_L_ | 6.2 @ 250 MHz | **5** | 88 @ 1000 MHz | 4.75 | 0.035 | 1.6 | Red |
| 0805HQ-12NX_L_ | 12 @ 250 MHz | **5** | 80 @ 1000 MHz | 3.00 | 0.045 | 1.6 | Orange |
| 0805HQ-16NX_L_ | 16 @ 250 MHz | **5,2** | 72 @ 500 MHz | 2.95 | 0.060 | 1.5 | Yellow |
| 0805HQ-18NX_L_ | 18 @ 250 MHz | **5,2** | 75 @ 500 MHz | 2.55 | 0.060 | 1.4 | Green |
| 0805HQ-20NX_L_ | 20 @ 250 MHz | **5,2** | 70 @ 500 MHz | 2.05 | 0.055 | 1.4 | Blue |
| 0805HQ-27NX_L_ | 27 @ 250 MHz | **5,2** | 75 @ 500 MHz | 2.00 | 0.070 | 1.3 | Violet |
| 0805HQ-30NX_L_ | 30 @ 250 MHz | **5,2** | 65 @ 500 MHz | 1.95 | 0.095 | 1.2 | Gray |
| 0805HQ-39NX_L_ | 39 @ 250 MHz | **5,2** | 65 @ 500 MHz | 1.60 | 0.110 | 1.1 | White |
| 0805HQ-48NX_L_ | 48 @ 200 MHz | **5,2** | 65 @ 500 MHz | 1.40 | 0.095 | 1.2 | Black |
| 0805HQ-51NX_L_ | 51 @ 200 MHz | **5,2** | 65 @ 500 MHz | 1.40 | 0.120 | 1.0 | Brown |

1. When ordering, please specify **tolerance** and **packaging** codes:

**0805HQ-51NX J L C**

   **Tolerance: G** = 2%   **J** = 5%  (Table shows stock tolerances in bold.)
   **Packaging: C** = 7″ machine-ready reel. EIA-481 embossed plastic tape (2000 parts per full reel).
       **B** = Less than full reel. In tape, but not machine ready. To have a leader and trailer added ($25 charge), use code letter C instead.
       **D** = 13″ machine-ready reel. EIA-481 embossed plastic tape. Factory order only, not stocked (7500 parts per full reel).

2. Inductance measured using a Coilcraft SMD-A fixture in an Agilent/HP 4286 impedance analyzer with Coilcraft-provided correlation pieces.

3. Tolerances in bold are stocked for immediate shipment.
4. Q measured using an Agilent/HP 4291A with an Agilent/HP 16193 test fixture.
5. For SRF less than 6 GHz, measured using an Agilent/HP 8753D network analyzer and a Coilcraft SMD-D test fixture. For SRF greater than 6 GHz, measured using an Agilent/HP 8722ES network analyzer and a Coilcraft SMD-D test fixture.
6. DCR measured on a Cambridge Technology micro-ohmmeter and a Coilcraft CCF840 test fixture.
7. Average current for a 15°C rise above 25°C ambient.
8. Operating temperature range –40°C to +125°C.
9. Electrical specifications at 25°C.
See Qualification Standards section for environmental and test data.

**COILCRAFT PRECISION** SEE INDEX   ACCURATE REPEATABLE MEASUREMENTS **TEST FIXTURES**

**S-Parameter files**
ON OUR WEB SITE OR CD

**SPICE models**
ON OUR WEB SITE OR CD

# Chip Inductors 0805HQ Series (2012)

## Typical Q vs Frequency



## Typical L vs Frequency





Terminal wraparound:
approx 0.015/0,38 both ends

**Recommended Land Pattern**
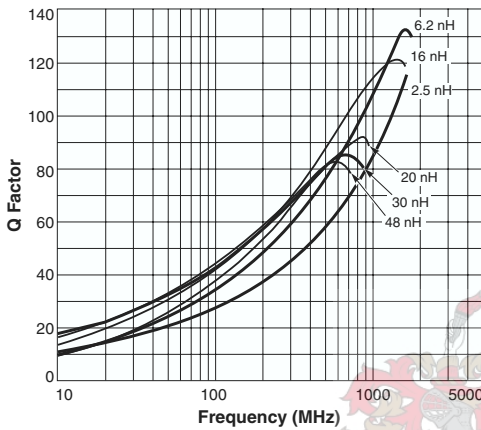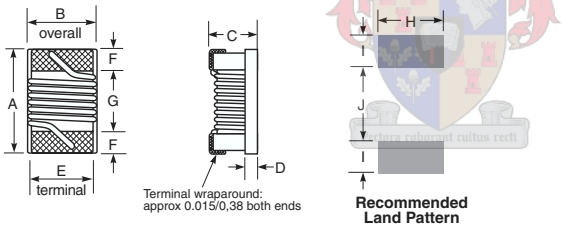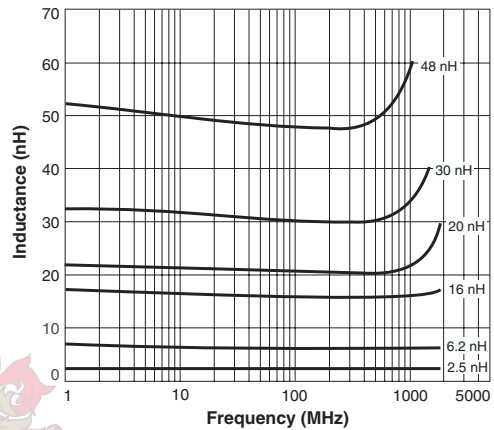
| A max | B max | C max | D | E | F | G | H | I | J |
|-------|-------|-------|------|------|------|------|------|------|------|
| 0.090 | 0.068 | 0.060 | 0.020 | 0.050 | 0.020 | 0.040 | 0.070 | 0.040 | 0.030 |
| 2,29 | 1,73 | 1,52 | 0,51 | 1,27 | 0,51 | 1,02 | 1,78 | 1,02 | 0,76 |

**Weight:** 10.5 – 12.5 mg
**Terminations:** Silver-palladium-platinum-glass frit
**Tape and reel:** 2000/7″ reel; 7500/13″ reel   8 mm tape width
For packaging data see Tape and Reel Specifications section.

## Coilcraft®

# Appendix D

# PLL Programming

## D.1 ADF4153 PLL Synthesizer

Figure D.1 shows the timing diagram of the ADF4153 PLL synthesizer from Analog Devices. Data is clocked into the 24-bit shift register on each rising edge of CLK. The data is clocked in MSB first and transfered from the shift register to one of the four latches (N divider register, R divider register, control register and noise and spur register) on the rising edge of LE.
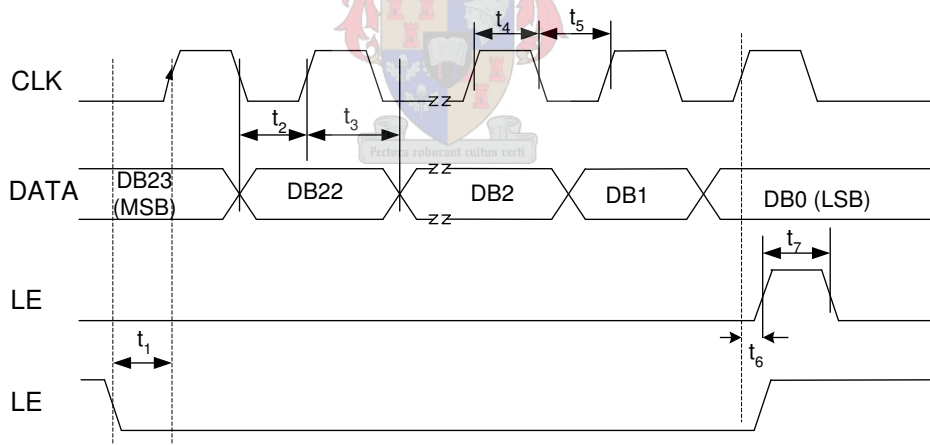


**Figure D.1:** Timing Diagram.

Two ADF4153 PLL synthesizers were programmed for 1900MHz and 1110.7MHz using a single ATmega32 microcontroller. Pins C1 to C3 of the microcontroller were assigned for DATA, CLK and LE of the 1900MHz PLL synthesizer; while Pins C6 to C8 were used for LE, CLK and DATA of the 1110.7MHz PLL synthesizer. The latches were programmed using Table 5.2 for low phase noise and spur mode [40]. The programming code was written using C++ as discussed in the following section.

## D.2 Program Code

```
#include <avr/io.h>
#include <avr/delay.h>

//Pins used for 1900MHz: DATA=PINC1; CLK=PINC2; LE = PINC3
//Pins used for 1110.7MHz: DATA=PINC8; CLK =PINC7; LE = PINC6

//Declare Variables

int counter;
unsigned char Control_reg[3];
unsigned char Noise_Spur_reg[3];
unsigned char R_divider_reg1900MHz[3];
unsigned char N_divider_reg1900MHz[3];
unsigned char R_divider_reg11107MHz[3];
unsigned char N_divider_reg11107MHz[3];

//Declare functions

void setupPLL1900MHz(unsigned char setup);
void setup_PLLvalues1900MHz(void)
void setupPLL11107MHz(unsigned char setup);
void setup_PLLvalues11107MHz(void)

//Functions

//For 1900MHz

void setupPLL1900MHz(unsigned char setup)
{
    int i;
    int DATA;
    for(i=7;i>=0;i--)
      {
         PORTC &= 0xFD;              //set CLK low
         DATA= setup»i;
         if (PORTC & 0x01)
           {
               DATA |=0xFE;
               PORTC &=DATA;
```

```
            }
        else
            {
                DATA &=0x01;
                PORTC |=DATA;
            }
        PORTC |= 0x02;              //set CLK high
        }
}

void setup_PLLvalues1900MHz(void)
{
    for(counter=0;counter<=2;counter++)
        setupPLL1900MHz_reg[counter]);
        PORTC |= 0x04;              //set LE high
        PORTC &=0xFB;              //Set LE low
    for(counter=0;counter<=2;counter++)
        setupPLL1900MHz(Noise_Spur_reg[counter]);
        PORTC |= 0x04;              //set LE high
        PORTC &=0xFB;              //Set LE low
    for(counter=0;counter<=2;counter++)
        setupPLL1900MHz(R_divider_reg1900MHz[counter]);
        PORTC |= 0x04;              //set LE high
        PORTC &=0xFB;              //set LE high
    for(counter=0;counter<=2;counter++)
        setupPLL1900MHz(N_divider_reg1900MHz[counter]);
        PORTC |= 0x04;              //set LE high
        PORTC &=0xFB;              //set LE high
}

//For 1110.7MHz

void setupPLL11107MHz(unsigned char setup)
{
    int i;
    int DATA;
    for(i=7;i<=0;i++)
        {
            PORTC &= 0xBF;              //set CLK low
            DATA= setup«i;
            if (PORTC & 0x80)
```

```
            {
                DATA |=0x7F;
                PORTC &=DATA;
            }
        else
            {
                DATA &=0x80;
                PORTC |=DATA;
            }
        PORTC |= 0x40;              //set CLK high
        }
}

void setup_PLLvalues11107MHz(void)
{
    for(counter=0;counter<=2;counter++)
        setupPLL11107MHz_reg[counter]);
        PORTC |= 0x20;             //set LE high
        PORTC &=0xDF;              //Set LE low
    for(counter=0;counter<=2;counter++)
        setupPLL11107MHz(Noise_Spur_reg[counter]);
        PORTC |= 0x20;             //set LE high
        PORTC &=0xDF;              //Set LE low
    for(counter=0;counter<=2;counter++)
        setupPLL11107MHz(R_divider_reg11107MHz[counter]);
        PORTC |= 0x20;             //set LE high
        PORTC &=0xDF;              //Set LE low
    for(counter=0;counter<=2;counter++)
        setupPLL11107MHz(N_divider_reg11107MHz[counter]);
        PORTC |= 0x20;             //set LE high
        PORTC &=0xDF;              //Set LE low
}

//Main function

int main(void)
{
//Data entry
    Control_reg[2]=0xE2;                   //Control register input
    Control_reg[1]=0x03;
    Control_reg[0]=0x00;
```

```
        Noise_Spur_reg[2]=0x83;                    //Noise and spur register input
        Noise_Spur_reg[1]=0x03;
        Noise_Spur_reg[0]=0x00;

        R_divider_reg1900MHz[2]=0x0D;                      //R divider register for 1900MHz
        R_divider_reg1900MHz[1]=0x40;
        R_divider_reg1900MHz[0]=0x14;

        N_divider_reg1900MHz[2]=0x08;                      //N divider register for 1900MHz
        N_divider_reg1900MHz[1]=0x80;
        N_divider_reg1900MHz[0]=0x1F;

        R_divider_reg11107MHz[2]=0x59;                       //R divider register for 1110.7MHz
        R_divider_reg11107MHz[1]=0x42;
        R_divider_reg11107MHz[0]=0x10;

        N_divider_reg11107MHz[2]=0x1C;                       //N divider register for 1110.7MHz
        N_divider_reg11107MHz[1]=0x80;
        N_divider_reg11107MHz[0]=0x12;

        DDRC = 0xFF;                    //Sets PORTC of ATmega32 as output

        PORTC &= 0x00;                  // Sets all pins low
        setup_PLLvalues1900MHz();

        PORTC &= 0x00;                  // Sets all pins low
        setup_PLLvalues11107MHz();

        return 1;
}
```

# Appendix E

# PCM Radar Receiver Measurements

The sub-systems designed in chapters 4 and 5 were integrated to form the complete PCM radar receiver, and measurements were performed to evaluate the performance of the receiver. A single channel of the final PCM radar receiver and measurement setup is shown in Figure E.1. For the input signal shown in Figure 6.3 of section 6.2.1 applied to RFFLT, the output of each sub-system was measured on the FSEK 30 spectrum analyzer. The measured results are shown in Figures E.2 to E.9.
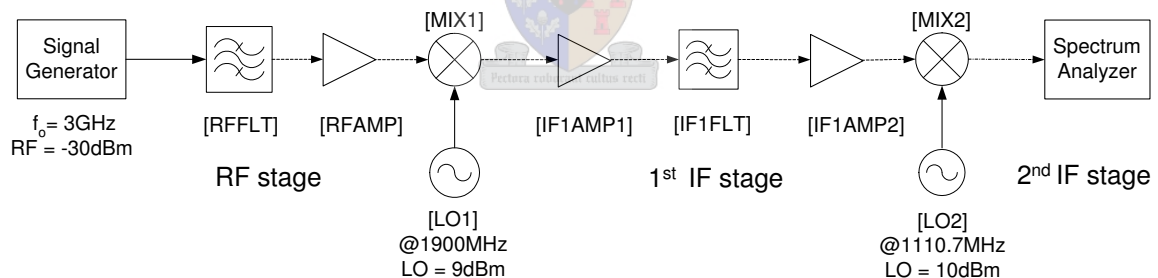


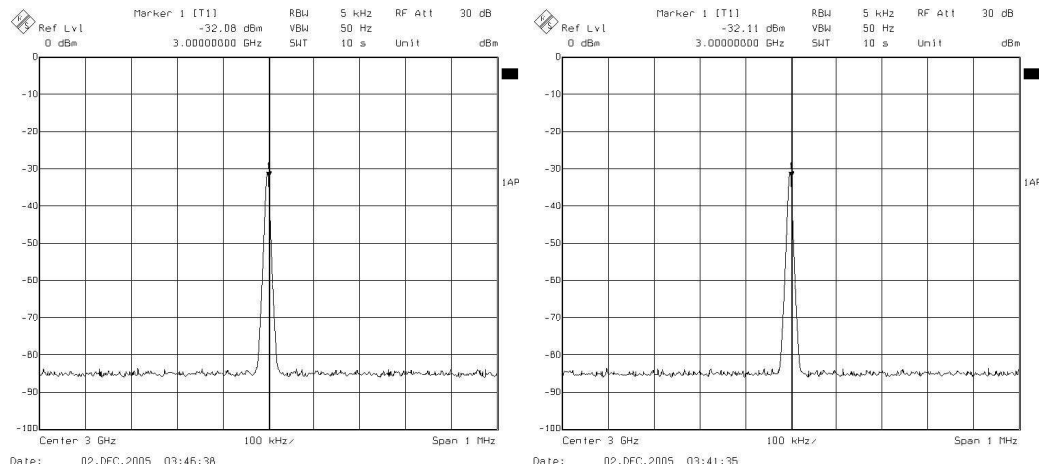**Figure E.1:** A single channel of the final PCM radar receiver.

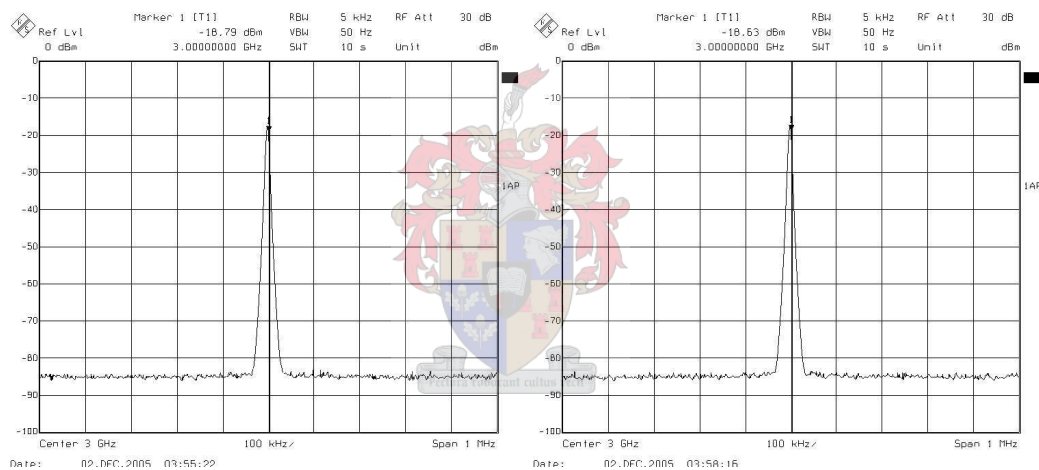**Figure E.2:** Measured frequency response at the output of RFFLTs : Σ-channel (left) and Δ-channel (right).



**Figure E.3:** Measured frequency response at the output of RFAMPs : Σ-channel (left) and Δ-channel (right).
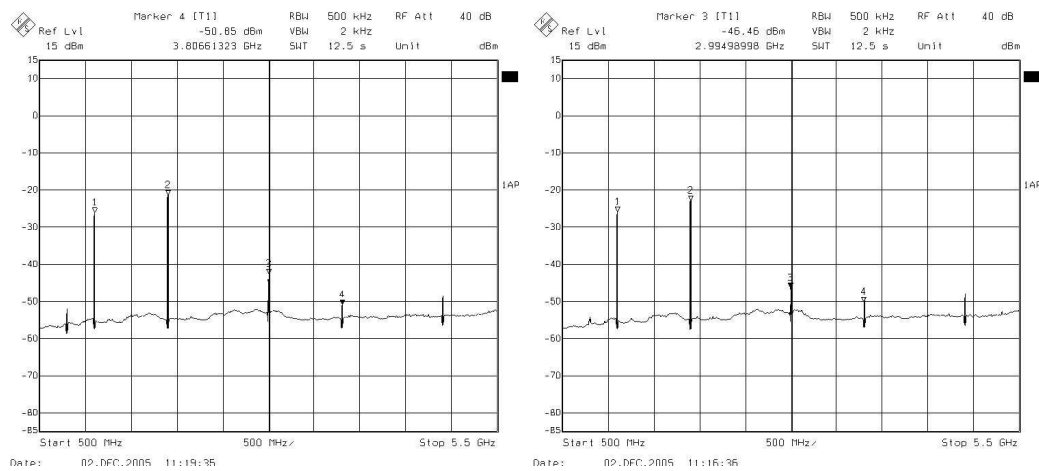


**Figure E.4:** Measured frequency response at the output of MIX1s : Σ-channel (left) and Δ-channel (right).
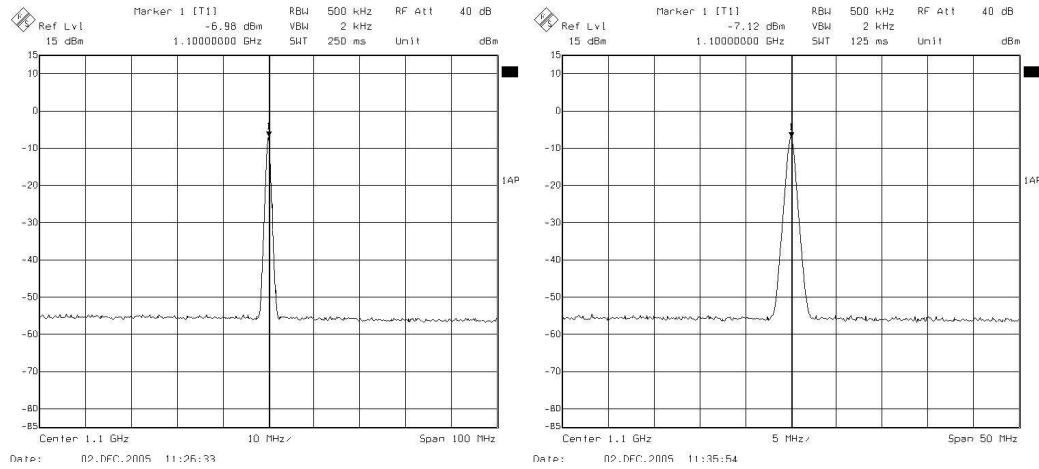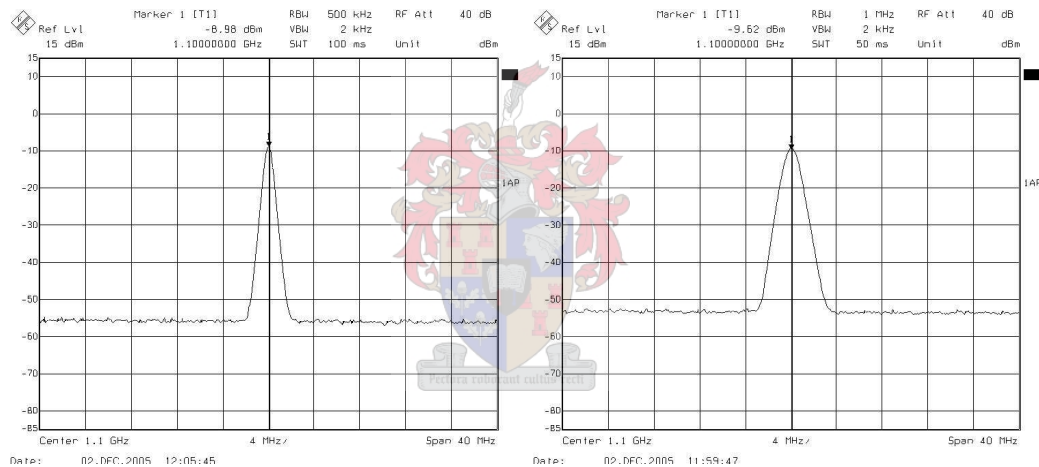
**Figure E.5:** Measured frequency response at the output of IF1AMP1s : $\Sigma$-channel (left) and $\Delta$-channel (right).



**Figure E.6:** Measured frequency response at the output of IF1FLTs : $\Sigma$-channel (left) and $\Delta$-channel (right).
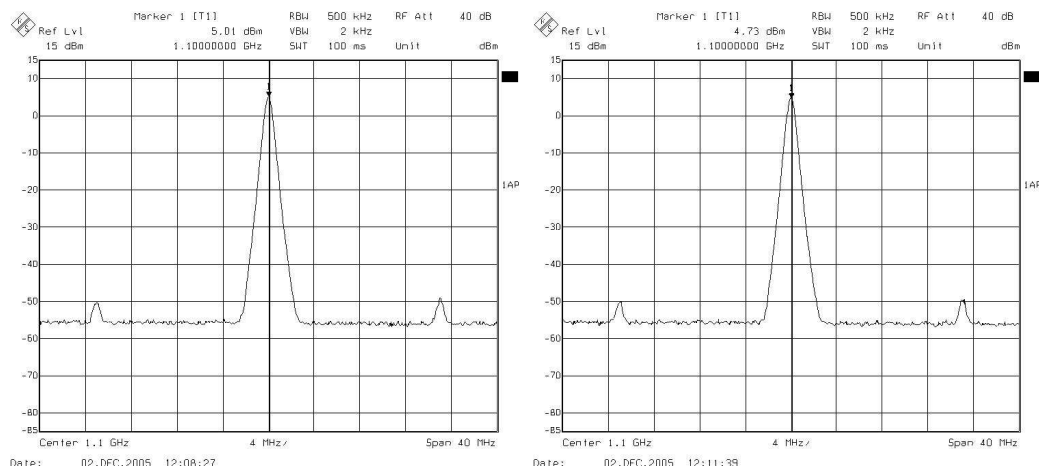


**Figure E.7:** Measured frequency response at the output of IF1AMP2s : $\Sigma$-channel (left) and $\Delta$-channel (right).
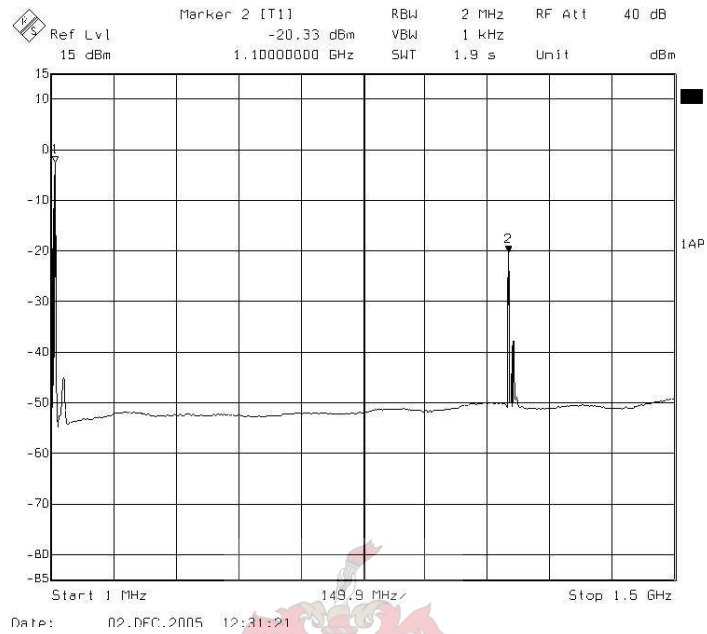
**Figure E.8:** Measured frequency response at the output of MIX2 of the Σ-channel.
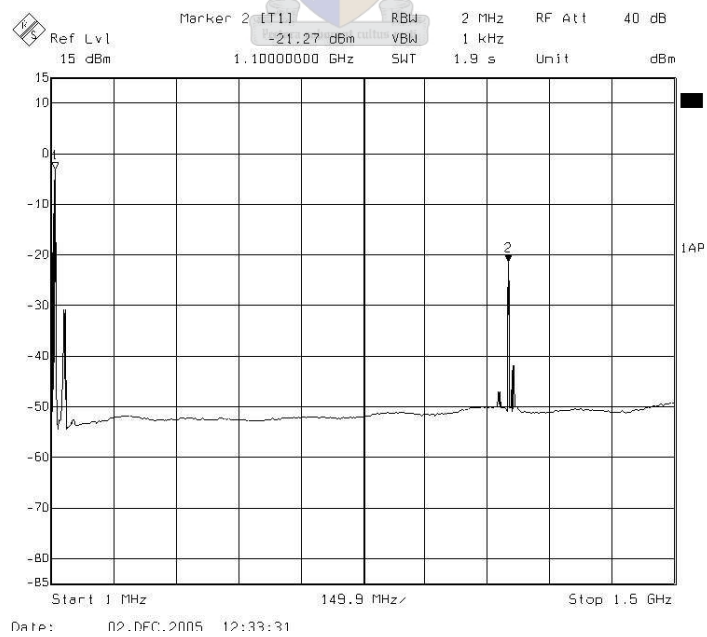


**Figure E.9:** Measured frequency response at the output of MIX2 of the Δ-channel.

# Appendix F

# PCM Radar Measurements

Discussed in this appendix is the measurements conducted to evaluate the performance of the PCM radar. Figure F.1 shows the layout of the measurement setup, where the target (a simple monopole antenna) is allowed to move horizontally while noting the outputs of the Σ and Δ-channels of the PCM radar receiver on an oscilloscope. The measured results are shown in Figures F.2 to F.7.
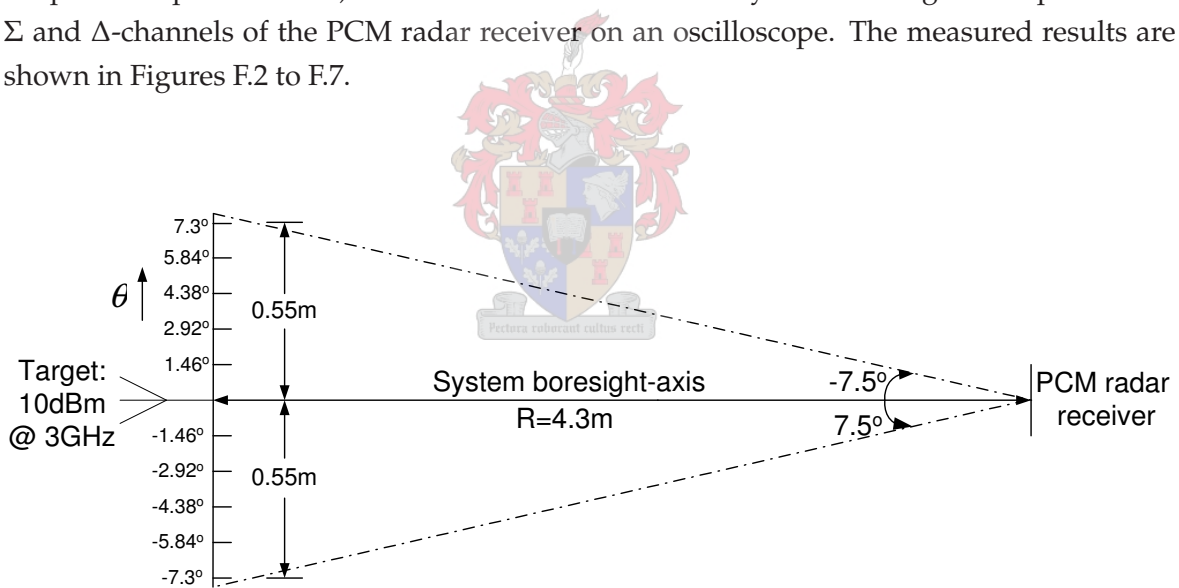


**Figure F.1:** PCM radar measurement layout.
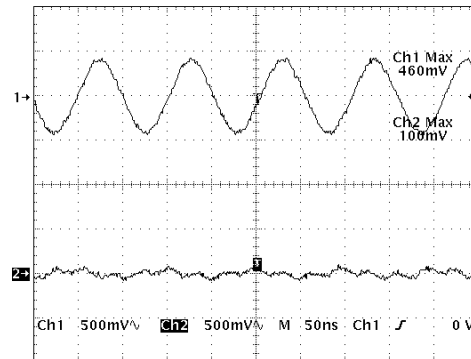
**Figure F.2:** Measured output of the Σ-channel (1) and Δ-channel (2) for the target on system boresight-axis $\theta=0^o$.



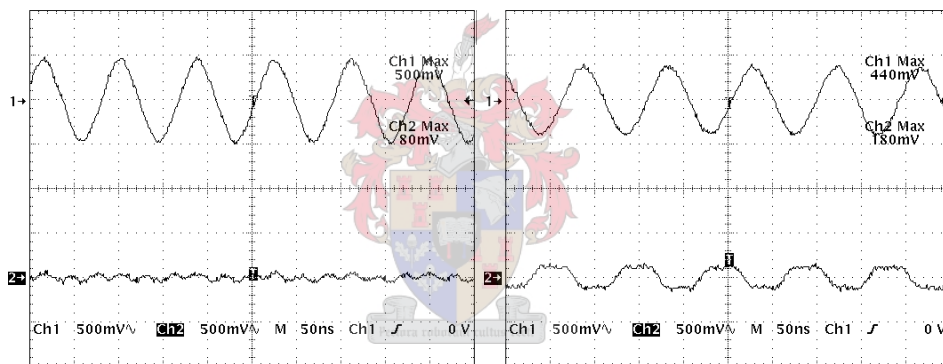**Figure F.3:** Measured output of the Σ-channel (1) and Δ-channel (2) for the target $\theta=$-1.46$^o$ (left) and $\theta=$1.46$^o$ (right) relative to the system boresight-axis.
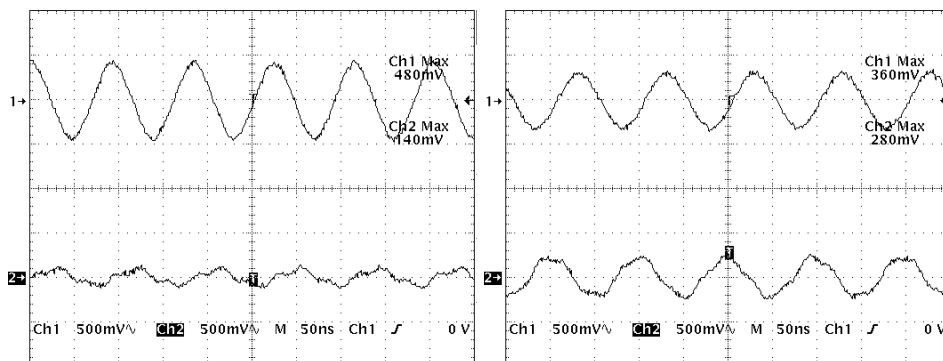


**Figure F.4:** Measured output of the Σ-channel (1) and Δ-channel (2) for the target $\theta=$-2.92$^o$ (left) and $\theta=$2.92$^o$ (right) relative to the system boresight-axis.
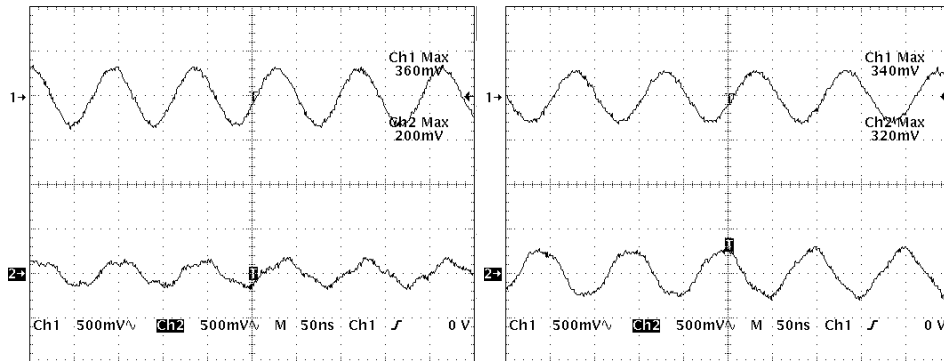
**Figure F.5:** Measured output of the $\Sigma$-channel (1) and $\Delta$-channel (2) for the target $\theta$=-4.38$^o$ (left) and $\theta$=4.38$^o$ (right) relative to the system boresight-axis.



**Figure F.6:** Measured output of the $\Sigma$-channel (1) and $\Delta$-channel (2) for the target $\theta$=-5.84$^o$ (left) and $\theta$=5.84$^o$ (right) relative to the system boresight-axis.



**Figure F.7:** Measured output of the $\Sigma$-channel (1) and $\Delta$-channel (2) for the target $\theta$=-7.3$^o$ (left) and $\theta$=7.3$^o$ (right) relative to the system boresight-axis.
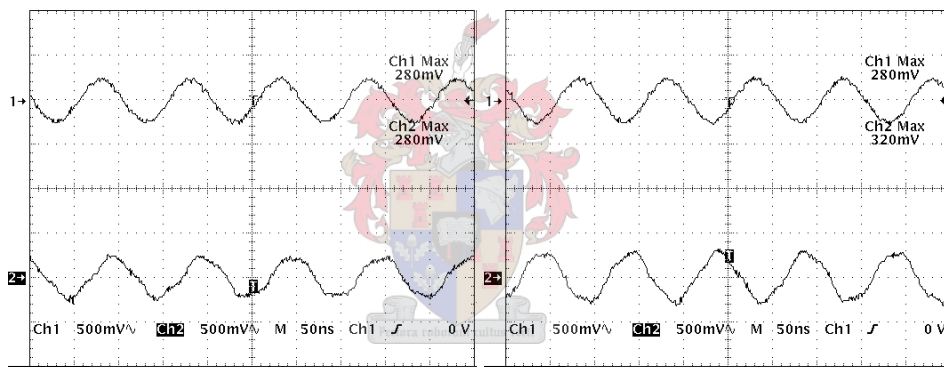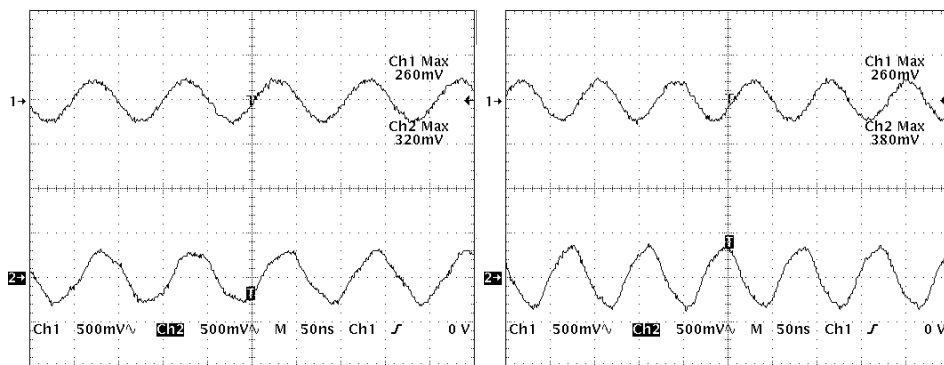
# List of References

[1]  D.K Barton, *Monopulse Radar*, vol. 1, Artech House, 1977.

[2]  M.I. Skolnik, *Introduction to Radar Systems*, McGraw-Hill, 1962.

[3]  W. Cohn and C.M. Steinmetz, "Amplitude-and phase-sensing monopulse system parameters," *Microwave Journal*, pp. 27–33, October 1959.

[4]  H.T. Friss, "Noise figure of radio receivers," *IRE Proc.*, pp. 419–422, July 1944.

[5]  D.M. Pozar, *Microwave Engineering*, John Wiley & Sons, Inc., 2nd edition, 1998.

[6]  W.F. Egan, *Practical RF System Design*, John Wiley and Sons, New York, 2003.

[7]  W.F. Egan, *Frequency Synthesis by Phase Lock*, John Wiley and Sons, New York, second edition, 2000.

[8]  Les Besser and Rowan Gilmore, *Practical RF Circuit Design for Modern Wireless Systems*, vol. I, Artech House, 2003.

[9]  S.A. Mass, *Nonlinear Microwave and RF Circuits*, Artech House, Boston, second edition, 2003.

[10] C.A. Balanis, *Antenna Theory Analysis and Design*, John Wiley & Sons Inc., second edition, 1982.

[11] Data Sheet AD8302, *RF/IF Gain and Phase Detector*, Analog Devices.

[12] J. Reed and G.J. Wheeler, "A method of analysis of symmetrical four-port networks," *IRE Trans. MTT*, pp. 246–252, October 1956.

[13] Peter Silvester and Peter Benedek, "Microstrip discontinuity capacitance for right-angle bends, t-junctions, and crossings," *IRE Trans. MTT*, pp. 341–346, May 1973.

[14] William H. Leighton and Arthur G. Milnes, "Junction reactance and dimensional tolerance effects on x-band 3-db directional coupleres," *IEEE Trans. MTT*, vol. MTT-19, no. 10, pp. 818–824, October 1971.

[15] J.R. Wolfgang Hoefer, "Equivalent series inductivity of a narrow transverse slit in microstrip," *IEEE Trans. MTT*, vol. MTT-25, no. 10, pp. 822–824, October 1977.

[16] MWO, *Applied Wave Research*, 2002.

[17] Rakesh Chadha and K.C Gupta, "Compensation of discontinuities in planar transmission lines," *IEEE Trans. MTT*, vol. MTT-30, no. 12, pp. 2151–2156, December 1982.

[18] R.J. Wenzel, "Exact design of tem microwave networks using quarter-wave lines," *IEEE Trans. MTT*, pp. 94–111, January 1964.

[19] G.L. Matthaei, "Comb-line bandpass filters of narrow or moderate bandwidth," *Microwave Journal*, pp. 82–91, August 1949.

[20] E.M.T. Jones and J.T. Bolljahan, "Coupled-strip-transmission-line filters and directional couplers," *IRE Trans. MTT*, vol. 19, pp. 75–81, April 1956.

[21] P.I. Richards, "Resistor transmission-line circuits," *IRE Proc.*, vol. 36, pp. 217–220, February 1948.

[22] Mohammed S. Ghausi Rolf Schaumann and Kenneth R. Laker, *Design of Analog Filters*, Prentice Hall, 1990.

[23] ZSYN, *Filter synthesis software developed at the University of Stellenbosch.*

[24] Ian Hunter, *Theory and Design of Microwave Filters*, London, Institution of Electrical Engineers, 2001.

[25] LINCALC, *Advanced Systmes Design*, 2004.

[26] G. L. Matthaei, "Intedigital bandpass filters," *IEEE Trans. MTT*, vol. 10, pp. 479–491, November 1962.

[27] J.A.G. Malherbe, *Microwave Transmission Line Filter*, Artech House, 1979.

[28] J.O. Scanaln, "Theory of microwave coupled-line networks," *Proc. IEEE*, vol. 68, no. 2, pp. 209–231, February 1980.

[29] R. J. Wenzel, "Theoretical and practical applications of capacitance matrix transformations to tem network design," *IEEE Trans. MTT*, vol. MTT-14, no. 12, pp. 635–647, December 1966.

[30] E. G. Cristal, "Coupled circularcylindrical rods between parallel ground planes," *IEEE Trans. MTT*, pp. 428–439, July 1964.

[31] CST Version 3, *Computer Simulation Technology*, 1998-2001.

[32] John R. Whinnery Simon Ramo and Theodore Van Duzer, *Fields and Waves in Communication Electronics*, John Wiley & Sons, Inc., third edition, 1994.

[33] E.J. Wilkinson, "An n-way power divider," *IRE Trans. MTT*, vol. MTT-8, pp. 116–118, January 1960.

[34] S.B. Cohn, "A class of broadband three-port tem-mode hybrids," *IEEE Trans. MTT*, vol. MTT-16, no. 2, pp. 110–116, February 1968.

[35] L.I. Parad and R.L. Moynihan, "Split-tee power divider," *IEEE Trans. MTT*, pp. 91–95, January 1965.

[36] Kun-Hui Yi and Bongokoo Kang, "Modified wilkinson power divider for nth harmonic suppression," *IEEE Microwave and Wireless Components Letters*, vol. 13, no. 5, pp. 178–180, May 2003.

[37] U. L. Rohde, *Digital PLL Frequency Synthesizers Theory and Design*, Prentice-Hall, Inc., New Jercy, 1983.

[38] Mike Curtin and Paul O' Brien, "Phase locked loops for high-frequency receivers and transmitters," Tech. Rep., Analog Devices.

[39] U.L. Rohde, "The design of oscillators and synthesizers," Tech. Rep., October 2000.

[40] ADF4153, *Fractional-N Frequency Synthesizer*, Analog Devices.

[41] Adrian Fox, "Ask the applications engineer-30 pll synthesizers," Tech. Rep.

[42] Data Sheet, *RF/IF Designer's Guide*, MiniCircuits.

[43] ADI SimPLL version 2.02, Analog Devices.

[44] Data Sheet, *Designer's Guide*, Hittite, 2004.

[45] Franklin F. Kuo, *Network Analysis and Synthesis*, John Wiley & Sons, Inc., Nework, second edition, 1966.

[46] CapCad version 3.0.2, *Dielectric Laboratories, Inc.*, 1999-2000.